HYPERSPECTRAL OBSERVATIONS FOR ATMOSPHERIC REMOTE SENSING: INSTRUMENTATION, ATMOSPHERIC CORRECTION, AND SPECTRAL UNMIXING

by

LOGAN ANSEL WRIGHT

B.S., University of Colorado Boulder, 2012

M.S., University of Colorado Boulder, 2014

A thesis submitted to the

Faculty of the Graduate School of the

University of Colorado in partial fulfillment

of the requirement for the degree of

Doctor of Philosophy

Department of Atmospheric and Oceanic Sciences

2018

This thesis entitled:

Hyperspectral Observations for Atmospheric Remote Sensing: Instrumentation, Atmospheric Correction, and Spectral Unmixing

written by Logan Ansel Wright

has been approved for the Department of Atmospheric and Oceanic Sciences

_____

Prof. Peter Pilewskie

_____

Prof. K. Sebastian Schmidt

Date_____

The final copy of this thesis has been examined by the signatories, and we find that both the content and the form meet acceptable presentation standards of scholarly work in the above-mentioned discipline.

Wright, Logan Ansel (Ph.D., Atmospheric and Oceanic Sciences)

Hyperspectral Observations for Atmospheric Remote Sensing: Instrumentation, Atmospheric Correction and Spectral Unmixing

Thesis directed by Professor Peter A. Pilewskie

Abstract

Hyperspectral instruments expand the spectral dimension of remote sensing measurements by collecting data in hundreds of contiguous wavelength channels. Spectrally resolved measurements can be used to derive science products for a diverse range of fields such as atmospheric science, geology, oceanography, ecology, climate monitoring, and agricultural science, to name a few. The spectral information collected by hyperspectral instruments enables more accurate retrievals of physical properties and detection of temporal changes. These advantages have led to an increasing number of active and planned hyperspectral instruments. This thesis describes methods for attributing hyperspectral radiation observations to physical sources.

We developed, validated and characterized improvements to a hyperspectral instrument, the Solar Spectral Irradiance Monitor (SSIM), built at the University of Colorado Boulder's Laboratory for Atmospheric and Space Physics. Contributions include the characterization of the optics' angular response, testing of an optics stabilizing platform and the development and testing of a spectrometer thermal control system. This instrument was then deployed on an aircraft for a field study with the National Ecological Observatory Network (NEON). SSIM measurements of upwelling and downwelling irradiance were used in conjunction with NEON's Imaging Spectrometer to enable atmospheric correction of imagery collected below cloud layers.

We developed a numerical spectral unmixing algorithm, Informed Non-Negative Matrix Factorization (INMF), to separate contributions to hyperspectral imagery from distinct physical

sources such as surface reflectance, atmospheric absorption, molecular scattering, and aerosol scattering. INMF was tailored for hyperspectral applications by introducing algorithmic constraints based on the physics of radiative transfer. INMF was tested using imagery collected by the Hyperspectral Imager for the Coastal Ocean (HICO). To validate the method INMF results were compared to model-based atmospheric correction results. We demonstrate possible applications of INMF by presenting the retrieval of two physical properties, aerosol attributed radiance and seafloor depth. The retrievals were evaluated by comparing INMF output to independent retrievals of aerosol properties from the Moderate Resolution Imaging Spectroradiometer (MODIS) and in-situ seafloor depth measurements from the U.S. Coastal Relief Model. In these comparisons INMF shows promise for retrieving both physical properties, and may be improved with physics-based constraints on the seafloor and aerosol source spectra.

Dedication

For my wife Abby, who has been a wonderful partner and friend and without whom this document would not exist.

Acknowledgements

I need to recognize some of the many individuals who have provided me with advice, support, and who have shared their expertise with me over the past five years. I first need to acknowledge Abby to whom this thesis is dedicated. Her support is so important to me that it needs to be mentioned again.

I would like to thank my adviser Peter Pilewskie for his guidance, support and advice and for encouraging me to define my own path through graduate school. Odele Coddington, who has provided endless support for my spectral unmixing work including refocusing me I wandered far afield. Sebastian Schmidt, Bruce Kindel, and Scott Kittelman from whom I learned instrument development, and memorized too many mil-spec components. Finally, all of the other students in the atmospheric radiation group, at LASP and in the Department of Atmospheric and Oceanic Sciences.

I have been supported for the last two and a half years by funding provided by NASA Headquarters under the NASA Earth and Space Science Fellowship Program – Grant "NNX15AJ58G".

Table of Contents

List of Tables

List of Figures

Chapter 1

Introduction

1.1. Remote Sensing Background

Remote sensing measurements are integral to many geoscience disciplines and can provide a comprehensive picture of the globe. Remote sensing is the observation and derivation of the properties of an object (whether cloud, atmosphere or land surface) from measurements of radiation made by instruments on aircraft or spacecraft. In practice, remote sensing encompasses a wide range of measurements and instruments. The measurements are typically classified as active or passive. Active instruments emit radiation and then detect the reflected signal. Examples of active instruments are lidars and radars. In contrast, passive instruments observe radiation emitted by the object being observed or reflected by the object from another source, like the sun. The work in this thesis uses passive remote sensing observations made in the 300 to 2500 nm range.

This wavelength range is often referred to as solar because it covers the range in which the sun radiates the majority of its energy. Moreover, in Earth's atmosphere and at the surface, electromagnetic radiation in this range is most likely to have been emitted by the sun. Passive, solar wavelength remote sensing has evolved from black-and-white images such as the first weather satellite image collected by TIROS-1 (Television and Infra-Red Observation Satellite) in 1960 (Anderson, 2010), to spectrally resolved multi-band measurements collected by satellites

such as the Landsat series that began with the Earth Resources Technology Satellite (ERTS-1) 1973 (NASA Goddard Space Flight Center, 1971), and instruments such as the Moderate Resolution Imaging Spectroradiometer (MODIS) (Ardanuy et al., 1991) (Figure 1.1).

More recently, improvements in spectrometer and detector technologies have led to the development of *hyperspectral imaging spectrometers*. These instruments, sometimes referred to simply as imaging spectrometers, are called *hyperspectral* to differentiate them from multispectral instruments, which collect data in discrete wavelength bands. Hyperspectral instruments collect data in hundreds of contiguous wavelength bands over the instrument's spectral range (Goetz et al., 1985). The development of hyperspectral imaging spectrometers was an important advance as these instruments produce spatially resolved images where a contiguous radiance spectrum is observed for each spatial pixel (Goetz, 2009).

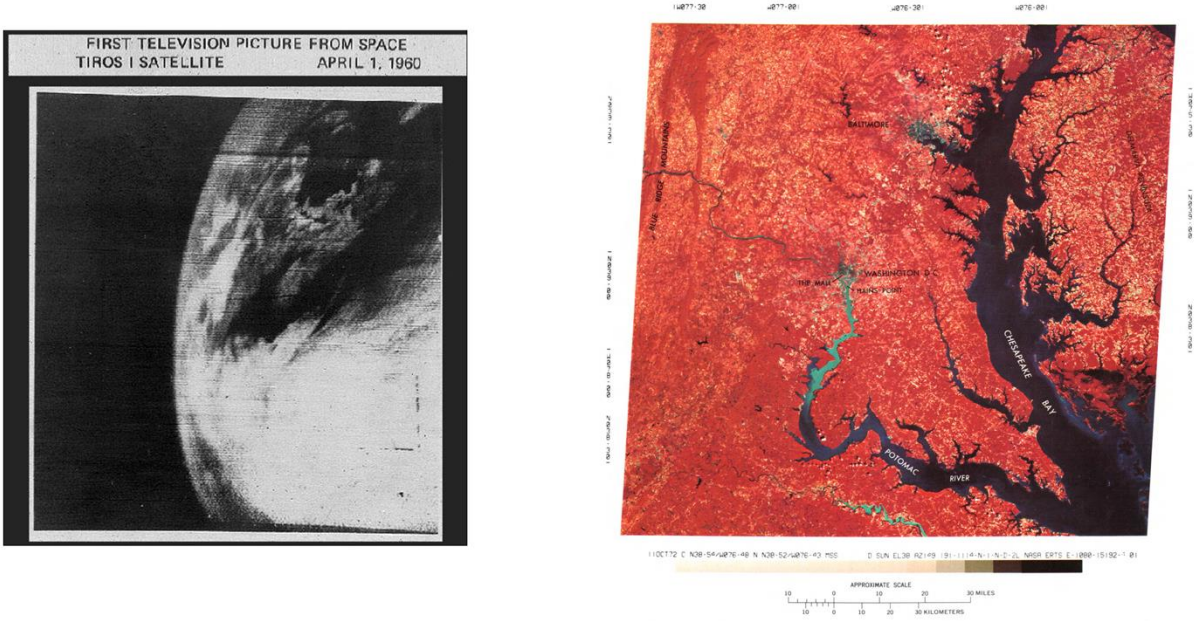

Figure 1.1: A progression of satellite remote sensing imagery.
Left: the first image returned by a weather satellite (TIROS-1) (Anderson, 2010). Right: a false color image collected by the Multispectral Scanner (MSS) instrument on ERTS-1 (later renamed Landsat 1). The MSS had four wavelength bands, green (500-600 nm), red (600-700 nm), and two near-infrared bands (700-800 nm and 800-1100 nm) (Williams Jr. & Carter, 1976).

The ability to measure a contiguous spectrum for each pixel in a scene is a powerful observational technique. Figure 1.2 shows a representation of a hyperspectral image, a hyperspectral data-cube or hypercube. This representation has the true-color image in front, with depth representing the spectral information with the edge pixels. This spectral information can be used to derive a diverse and useful array of data products including leaf area index (LAI) (Verrelst et al., 2015), leaf chlorophyll content (LCC) (Verrelst et al., 2015); surface mineral maps (Crowley et al., 1989), real-time atmospheric methane retrievals (Thompson, Leifer, et al., 2015), among many others. In early hyperspectral measurements the ability to take advantage of the collected spectral information was limited by low signal-to-noise ratios (SNR) (Vane et al., 1984), the large volumes of data produced by hyperspectral instruments, and computational requirements to process such large datasets (Goetz, 2009). In the decades since the first imaging spectrometers were flown in the 1980s many of these limitations have been overcome. Modern imaging spectrometers such as the National Ecological Observatory Network's (NEON) imaging spectrometer have SNR of greater than 1000 (Johnson et al., 2010), and the costs of storing and processing large volumes of data are now manageable. Because of these technical

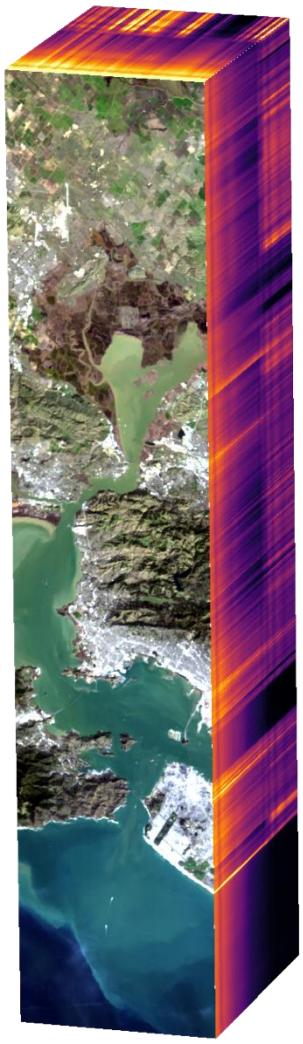

Figure 1.2: A hyperspectral data-cube, or hypercube, collected by the Hyperspectral Imager for the Coastal Ocean (HICO). HICO collects data in 128 wavelength bands. The hypercube shows wavelength in the depth axis, with wavelength increasing from shallow to deep. Yellow colors are the highest signals, purples and blacks are the lowest.

improvements and the success of earlier instruments, many hyperspectral instruments are currently in operation and many more are planned for the future.

1.2. Motivations for Hyperspectral Sensing

Hyperspectral measurements command strong research interest because they offer a more complete measurement of atmospheric and surface properties than multispectral observations. Collecting contiguous spectra is important because the signatures of atmospheric species and processes are spectrally overlapping across the solar wavelength range (Figure 1.3, top panel). Similarly, surface reflectance varies substantially in spectral shape and magnitude between surface types (Figure 1.3, bottom panel). In remote sensing applications the challenge of connecting observations to physical processes is magnified because atmospheric signals are commonly mixed with signal reflected from the surface. Multispectral instruments approach the problem of mixed signals by selecting wavelength ranges that minimize the mixing between target signals (Goetz, 2009). This approach makes comparatively straightforward retrievals of the selected properties but because of the

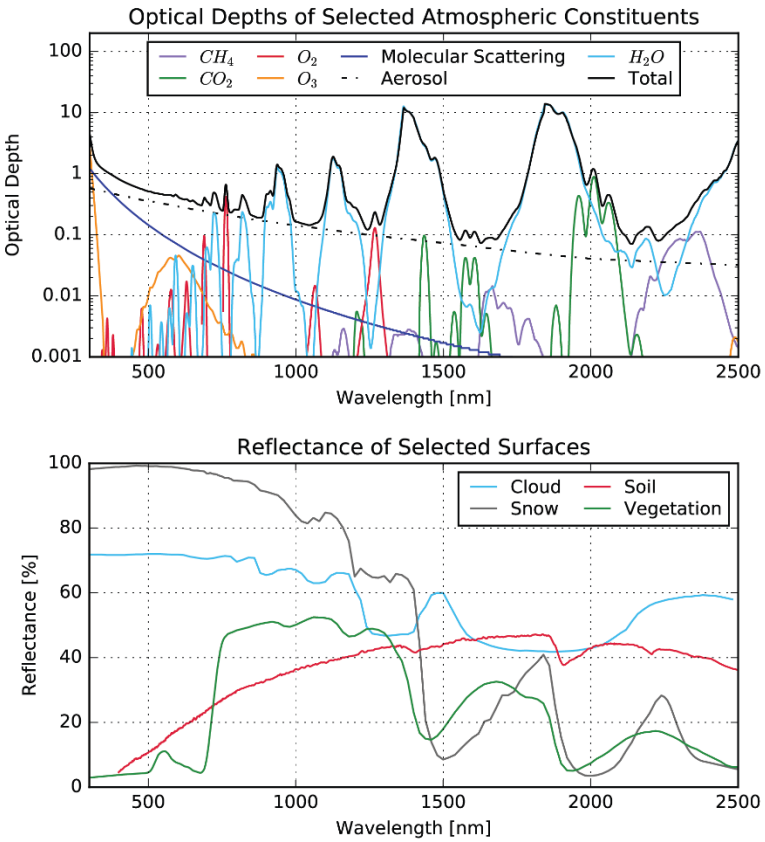

Figure 1.3: Optical depths (top) and surface reflectance (bottom) of selected atmospheric constituents and selected surfaces

limited number of wavelength bands observed, there is little opportunity to reduce noise in the retrieval by exploiting the correlation in signal across broad spectral regions (Goetz, 2009).

To highlight the difference in approaches between multi- and hyperspectral approaches consider the channels of the MODIS instruments compared to the channels of a hyperspectral instrument such as the Hyperspectral Imager for the Coastal Ocean (HICO) (Figure 1.4). MODIS includes 36 spectral channels that were each chosen to support a particular science products (Barnes et al., 1998; Justice et al., 1998). For example, MODIS channels 17, 18, and 19 were primarily used to retrieve atmospheric water vapor, while channels 1 through 7 were intended to retrieved land and cloud properties (Barnes et al., 1998). These channels cover only a fraction of the entire spectrum (Figure 1.4, top panel), compared to a hyperspectral instrument with contiguous and overlapping measurements over the entire spectral range (Figure 1.4, bottom panel). In the wavelength range between 350 nm and 1100 nm MODIS has 16 channels while HICO has 128 (Barnes et al., 1998; Lucke et al., 2011).

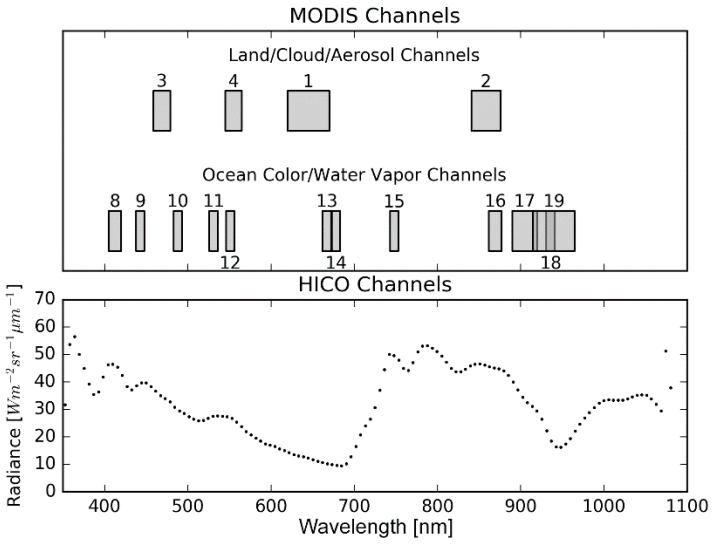

Figure 1.4: Spectral channels of the MODIS instruments (top) and the HICO instrument (bottom).
The spectral extent and primary use of the MODIS channels is shown. The HICO image shows an example radiance spectrum and only the channel centers are shown due to their number. Both panels are plotted on the same wavelength axis. [Source data from: Barnes et al., 1998 (MODIS); Lucke et al., 2011 (HICO)]

In contrast to the multispectral instrument approach described above, hyperspectral instruments observe many wavelengths in a contiguous spectrum. This approach does not require instrument channels to be chosen for a specific function since the

complete spectrum is observed. Instead the challenge for hyperspectral instruments is making full use of the data collected. Traditional multispectral methods can be applied to hyperspectral data by extracting specific wavelength bands to mimic a multispectral instrument. However, this approach does not make full use of the spectral data provided by hyperspectral measurement.

Hyperspectral observations are made on the premise that the addition of spectral channels to an observation provides more information that can be used to improve the accuracy of property retrievals (Rodgers, 1998; Vukicevic et al., 2010). This is an intuitive result that adding spectral channels generally adds more information (Coddington et al., 2012; Rodgers, 1998). However, channels may include redundant information, or perhaps no information on a particular property, so that information content does not increase linearly with the number of spectral channels (Rodgers, 1998). Information theory can be applied to quantitatively measure the impact of collecting more spectral channels. Shannon information content (Shannon & Weaver, 1949) is one commonly employed metric. Previous work has explored the application of information content metrics to the selection of wavelength channels and their impacts on property retrievals (Coddington et al., 2012; Cooper et al., 2006; L'Ecuyer et al., 2006; Rodgers, 1998, 2000; Tamminen & Kyrölä, 2001; Taylor et al., 2008; Vukicevic et al., 2010). For hyperspectral remote sensing the continuing challenge is how to best use the increased information content of hyperspectral measurements to extract the desired science properties given that the observations are composed of signals from many physically distinct sources.

Another important application of hyperspectral observations is climate change detection and monitoring through missions such as the NASA Climate Absolute Radiance and Refractivity Observatory (CLARREO) mission (Wielicki et al., 2013). High accuracy observations are needed to detect climate change within a reasonable observational period (Wielicki et al., 2013). Spectrally

resolved measurements provide more information than their broadband counterparts, reducing the time required to detect climate change trends (Wielicki et al., 2013) and attribute them to their physical sources (Feldman et al., 2011; Roberts et al., 2011).

Beyond trend detection, the high accuracy requirements of a planned future climate observing system necessitates improved hyperspectral processing methods. Existing methods have accuracies of 10-20% for surface reflectance (Richter & Schläpfer, 2002) and 15-20% for aerosol optical depth (Levy et al., 2013). Conversely, CLARREO's solar wavelength instrument has a requirement for systematic error less than 0.3% (Wielicki et al., 2013). It should be noted that CLARREO's intended climate change trend detection does not rely on retrieving physical properties and these values compare geophysical property retrieval accuracies (of 10-20%) against a systematic measurement error (of 0.3%). However, the comparison of the two values highlights that retrieval errors are almost two orders-of-magnitude larger than measurement errors demonstrating a need for research to improve retrieval methods.

Hyperspectral instruments have also recently been incorporated into projects such as the Airborne Snow Observatory (ASO) (Painter et al., 2016), which measures snowpack to advise municipal water systems in California, and NEON's Airborne Observation Program (AOP) (Schimel et al., 2011), which will make yearly observations across the United States. The ASO employs a hyperspectral imager and a lidar to measure the snow water equivalent, and snow albedo of snowpack in mountain basins (Painter et al., 2016). NEON's AOP operates a similar payload consisting of a hyperspectral imager, lidar, and high-resolution camera, but the goal is to monitor terrestrial ecosystems (Kampe, Johnson, Kuester, & Keller, 2010). Chapter 3 of this thesis describes research performed with NEON's AOP to improve surface property retrievals. The

launch of these two observation programs demonstrates the maturity of hyperspectral instrumentation and the versatility of their measurements.

Figure 1.5 shows a timeline of major hyperspectral instruments, both space-based and airborne. In addition to a number of continuing major airborne campaigns there are four major space-based hyperspectral missions planning to launch within the next five years. The increasing number of operational and planned hyperspectral missions makes it clear that the benefits of these observations have been recognized. Given this trend, this thesis presents a timely investigation of hyperspectral applications and processing methods.

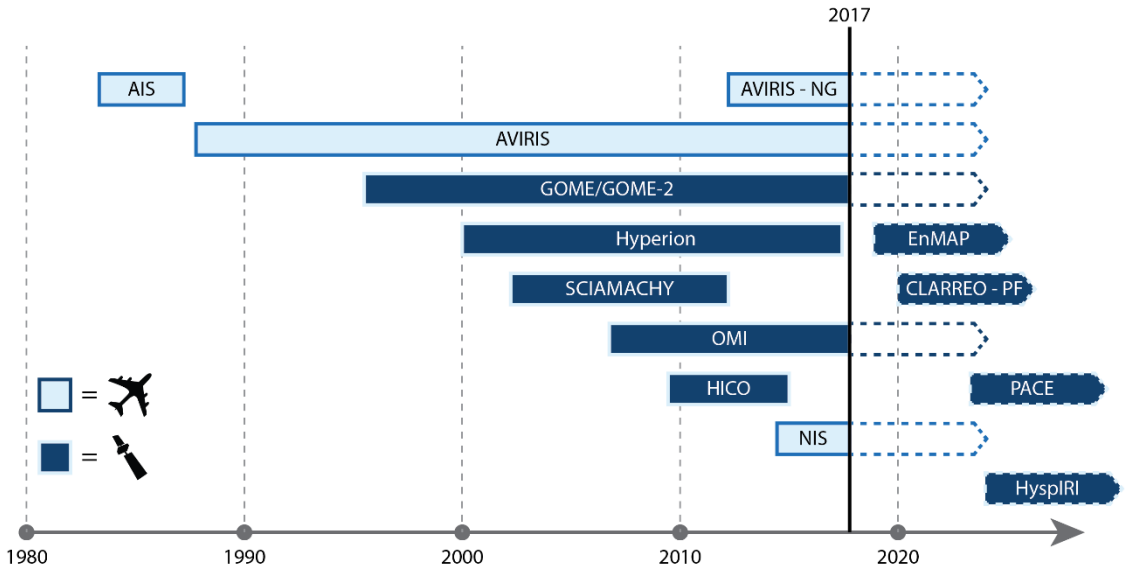

Figure 1.5: A timeline showing major hyperspectral imaging spectrometer instruments. Light blue boxes are airborne instruments, while dark blue are satellite instruments. Dashed boxes indicate future deployments.

Table 1.1: Major hyperspectral instrument missions, historical, ongoing, and planned.

Instrument:	**Reference:**
Airborne Imaging Spectrometer (AIS)	(Vane et al., 1984)
Airborne Visible/Infrared Imaging Spectrometer (AVIRIS)	(Green et al., 1998)
Global Ozone Monitoring Experiment (GOME)	(Burrows et al., 1999)
Global Ozone Monitoring Experiment 2 (GOME-2)	(Callies et al., 2000)
Hyperion	(Pearlman et al., 2003)
Scanning Imaging Absorption Spectrometer for Atmospheric Chartography (SCIAMACHY)	(Bovensmann et al., 1999)
Ozone Monitoring Instrument (OMI)	(Levelt et al., 2006)
Hyperspectral Imager for the Coastal Ocean (HICO)	(Lucke et al., 2011)
AVIRIS – Next Generation (AVIRIS-NG)	(Hamlin et al., 2011)
National Ecological Observatory Network's Imaging Spectrometer (NIS)	(Kampe, Johnson, Kuester, & McCorkel, 2010).
Planned hyperspectral instruments include:	
Environmental Mapping and Analysis Program (EnMAP)	(Guanter et al., 2015)
Climate Absolute Radiance and Refractivity Observatory – Pathfinder (CLARREO-PF)	(Wielicki et al., 2013)
Plankton, Aerosol, Cloud, Ocean Ecosystem (PACE)	(NASA Goddard Space Flight Center, 2017)
Hyperspectral Infrared Imager (HyspIRI)	(C. M. Lee et al., 2015)

1.3. Remote Sensing Measurements

Remote sensing instruments do not directly provide information on surface or atmospheric properties. Instead they measure the radiation scattered by the atmosphere and surface that is related to their intrinsic properties and therefore, can be used to derive those properties. For example, imaging spectrometers measure a radiation quantity called *spectral radiance*. Spectral

radiance is the radiative flux density per unit wavelength, per unit solid angle that is incident on a surface, normal to the direction of incidence (Bohren & Clothiaux, 2006). Spectral radiance has units of watts per square meter per steradian per nanometer ($W \cdot m^{-2} \cdot sr^{-1} \cdot nm^{-1}$). Another important radiation measurement is *irradiance*, which is the radiance received by a surface of unit area, scaled by the cosine of the radiance direction to the surface normal, and integrated over a finite range of solid angle, most commonly the hemisphere (Bohren & Clothiaux, 2006). In atmospheric science defining irradiance over a hemisphere relative to the Earth's horizon allows independent measurements of the radiation propagating upwards (upwelling irradiance) and radiation propagating towards the surface (downwelling irradiance). *Spectral irradiance* is the irradiance per unit of wavelength, with units of watts per square meter per nanometer ($W \cdot m^{-2} \cdot nm^{-1}$).

Table 1.2: Radiometric Quantities (Wyatt et al., 1998)

Quantity	***Symbol***	***Unit***
Radiative Flux	Φ_e	W
Radiance	L	$W \cdot m^{-2} \cdot sr^{-1}$
Spectral Radiance	L_λ	$W \cdot m^{-2} \cdot sr^{-1} \cdot nm^{-1}$
Irradiance	F	$W \cdot m^{-2}$
Spectral Irradiance	F_λ	$W \cdot m^{-2} \cdot nm^{-1}$

The measured quantity depends on the instrument design. Imaging spectrometers record spectral radiance, because they must observe in narrow ranges of direction to resolve spatial features. Spectral irradiance can be measured with other instruments such as the Solar Spectral Irradiance Monitor (SSIM), described in Chapter 2, that integrates over the hemisphere.

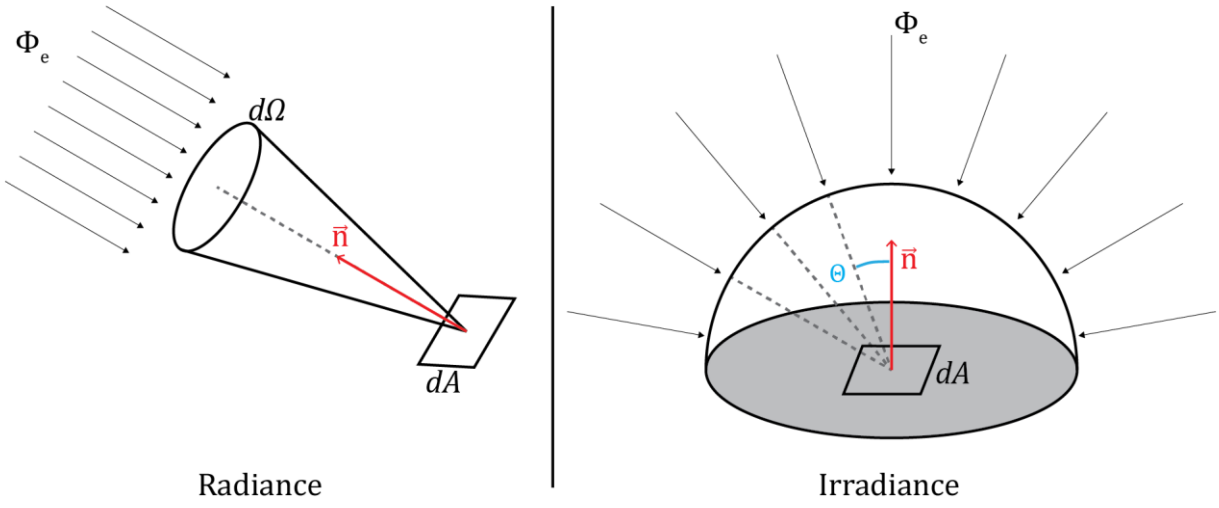

Figure 1.6: Diagrams showing the definition of radiance (left) and irradiance (right). Radiance is defined by the incoming radiation field (Φ_e) that passes through a unit solid angle ($d\Omega$) and passes through a unit of surface area (dA) that is normal to the radiation field. Irradiance is the integral of incident radiance over some amount of solid angle (shown here as a hemisphere) and is scaled by projected area, which is dependent on the angle (Θ) between the incident radiation and the normal vector of the surface ($\vec{n}$).

The measured radiance or irradiance is dependent on the observed target and the instrument's location on the ground, on an aircraft, or in space. This *at-sensor measurement* includes contributions from the target and from the atmosphere. Deriving a physical property from an at-sensor measurement requires a *retrieval process* to connect the observed radiation to desired quantity through the underlying radiative processes of atmospheric absorption, scattering or surface reflectance (Rodgers, 2000). Often a preparatory step known as *Atmospheric correction* is required to separate atmospheric effects from surface reflectance to derive surface information (B.-C. Gao et al., 1993, 2006). Atmospheric correction is crucial for surface remote sensing because it removes the effects of the atmosphere from a measured signal. Typically atmospheric correction involves the use of a radiative transfer model to determine the combined radiative sources from atmospheric and surface. However, model-based routines can be inaccurate for a variety of reasons including assumptions about atmospheric composition, aerosol type and size distributions, and

uncertainties in the incident solar spectrum. Improving atmospheric correction could significantly affect the accuracy of many science products.

1.4. Summary of Thesis Chapters

1.4.1. Chapter 2: Solar Spectral Irradiance Monitor Development

This chapter describes development and characterization of the Solar Spectral Irradiance Monitor (SSIM), a hyperspectral instrument built by the Laboratory for Atmospheric and Space Physics (LASP) at the University of Colorado Boulder (CU). This instrument is used to observe spectrally resolved irradiance over the most of the solar spectrum, from 350 nm to 2150 nm. This chapter discusses improvements to the instrument that were undertaken and validated as part of an observational campaign with the National Ecological Observatory Network (NEON) in summer 2015. These improvements include the testing of a redesigned actively-stabilized optics assembly, the validation of the angular response of a new optical design, and the design and validation of a spectrometer temperature control system. This chapter also describes the laboratory spectral and radiometric calibration of the SSIM and the field calibration of the instrument while it is installed on an aircraft.

1.4.2. Chapter 3: Below-Cloud Atmospheric Correction of Airborne Hyperspectral Imagery Using Simultaneous Solar Spectral Irradiance Observations

This chapter details a study in which the SSIM was flown on a Twin Otter aircraft together with the NEON imaging spectrometer (NIS). This study examines how simultaneous hyperspectral imagery, from the NIS, and irradiance measurements provided by the SSIM, can be used to improve the atmospheric correction of the hyperspectral imagery. For this work we deployed calibrated reflectance targets and collected ground truth reference spectra, using a portable field spectrometer, at a field site north of Boulder, Colorado. Data collection flights were made over the ground site on several days in cloud-free, overcast, and scattered clouds conditions. This work

demonstrates that SSIM measurements can be used for more accurate atmospheric correction when the aircraft flew below a cloud layer where traditional atmospheric correction methods fail. This work also examines the use of upwelling irradiance observations to estimate and correct *adjacency effects* (to be defined in §3.2).

1.4.3. Chapter 4: An Informed Non-Negative Matrix Factorization Method for Unmixing Atmospheric and Surface Signals in Hyperspectral Imagery

This chapter describes the development of a numerical algorithm, Informed Non-Negative Matrix Factorization (INMF), to identify and separate contributions from surface reflectance and the atmosphere in hyperspectral imagery. This method was developed to address some of the limitations of other commonly used numerical processing techniques. We designed INMF for separating signals in at-sensor radiance observations, while most other *spectral unmixing* (to be defined in §4.2) approaches have focused on surface reflectance. To improve the separation of physically distinct sources we modified INMF to incorporate knowledge of the physics of remote sensing instrumentation and radiative transfer. This was included in the algorithm by constraining spectral and spatial smoothness, which are determined by the observing instrument, and the spectral shape of molecular scattering, determined by Rayleigh's Law.. To further guide the solution towards physically realistic results, library reflectance spectra are used to generate an initial guess of source spectra. We evaluated the performance of INMF using hyperspectral imagery collected by the Hyperspectral Imager for the Coastal Ocean (HICO). Using two HICO images, we tested INMF's sensitivity to the choice of scene and the sensitivity of INMF to the magnitude of the initial guess spectra. The INMF solutions were compared, in both magnitude and spectral shape, with traditional model-based atmospheric correction radiance products.

1.4.4. Chapter 5: Evaluation of First Retrievals of Atmospheric and Surface Properties from Hyperspectral Imagery using Informed Non-Negative Matrix Factorization

The goal of numerical *unmixing* techniques is to produce a result that connects observed radiance to radiative properties such as surface reflectance and aerosol or cloud scattering. This chapter presents the derivation of two system properties, aerosol optical depth and seafloor depth, from INMF results. An initial guess of the aerosol scattering spectrum was derived from radiative transfer modeling of standard aerosol profiles from MODTRAN. An initial guess of the spectrum of a seafloor below shallow water was extracted from the imagery itself. A significant challenge in this work is validating the results: ground-truth measurements for many applications are sparse or nonexistent. This work compared the INMF derived properties against independent satellite or in-situ measurements. Derived aerosol properties were compared, spectrally and spatially, to Moderate Resolution Imaging Spectroradiometer (MODIS) retrievals of aerosol properties. Seafloor depth data were compared to bathymetric maps derived from sonar measurements.

1.4.5. Chapter 6: Summary and Directions for Future Work

This final chapter summarizes the results from the previous chapters and highlights possible areas of future work stemming from the results of each chapter.

Chapter 2

Solar Spectral Irradiance Monitor Development

2.1. Overview

The Solar Spectral Irradiance Monitor (SSIM) is the product of iterative improvement upon the NASA Ames Research Center Solar Spectral Flux Radiometer (SSFR) instrument (Pilewskie et al., 2003). The original development of the SSIM leveling and spectrometer systems was sponsored by NASA. A sibling instrument to National Ecological Observatory Network's (NEON) SSIM was flown during NASA's Arctic Radiation IceBridge Sea and Ice Experiment (ARISE) in 2014 (Smith et al., 2017). This chapter details the major improvements over previous generations of this instrument. The description of the instrument testing and validation highlights the contributions I have made to the SSIM development.

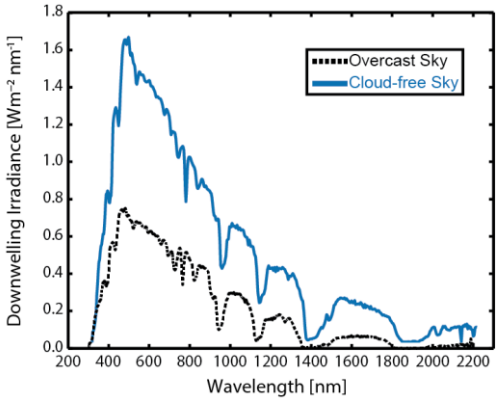

Figure 2.1: Downwelling irradiance measured by the SSIM in cloud-free and overcast sky conditions.

This SSIM system was built for NEON and consists of three components: a spectrometer enclosure, foreoptics, and a leveling platform on the exterior of the aircraft. Figure 2.1 shows an

example of downwelling irradiance spectra measured by the SSIM under both cloud-free and overcast conditions. The instrument was delivered to NEON in May 2015. A set of engineering test flights were conducted in the first half of June 2015, and the collected data were used for a study of retrieving surface reflectance value when the aircraft was flown below clouds. Chapter 3 reports the results of that work.

The spectrometer enclosure houses two Zeiss spectrometers that cover a wavelength range from 350 nm to 2150 nm. One spectrometer uses a silicon (Si) linear array detector to measure the wavelength range from 350 nm to 1000 nm; the other uses an Indium-Gallium-Arsenide (InGaAs) detector array for sampling from 900 nm to 2150 nm. The Si spectrometer has spectral sampling of 3.3 nm and a Full-Width-Half-Maximum (FWHM) spectral resolution of 9 nm while the InGaAs-detector spectrometer has spectral sampling and resolution of 5 nm and 16 nm FWHM, respectively. The full-system contains two sets of these spectrometers, one connected to the zenith pointing foreoptics for measuring downwelling irradiance, the other to nadir pointing foreoptics for measuring upwelling irradiance. In the NEON SSIM the nadir-pointing InGaAs spectrometer (900-2150 nm) was not deployed. The spectrometers are housed in a standard 19-inch aircraft rack mounted enclosure that includes data acquisition, signal amplification, digitization, spectrometer control, and temperature control electronics. Fiber optic cables from the foreoptics connect through shutters to the spectrometers. When closed, the shutters enable the in-flight measurement of dark current levels that are applied as part of the radiometric calibration of the spectrometer data.

The foreoptics are hemispheric-viewing light collectors mounted on the exterior of the aircraft. Figure 2.2 shows a diagram of the light collector design and Figure 2.3 shows the zenith and nadir pointing foreoptics mounted on the NEON Twin Otter aircraft. A light collector consists of a fused quartz dome that covers a one-inch diameter integrating sphere. The entrance aperture

to the integrating sphere ensures that the signal from incident light is weighted by the cosine of the zenith angle and is, therefore, proportional to irradiance. The integrating sphere serves to collect and diffuse the directly transmitted radiation. It is made of Fluorilon, which has a reflectance of 99% or greater in the visible wavelengths. Using this highly reflective material increases the system's signal to noise ratio by increasing the amount of radiation reaching the detector. A fiber optic bundle is mounted at the base of the integrating sphere to transmit light to the spectrometers. A baffle inside the integrating sphere prevents direct and first-reflected light from entering the fibers.

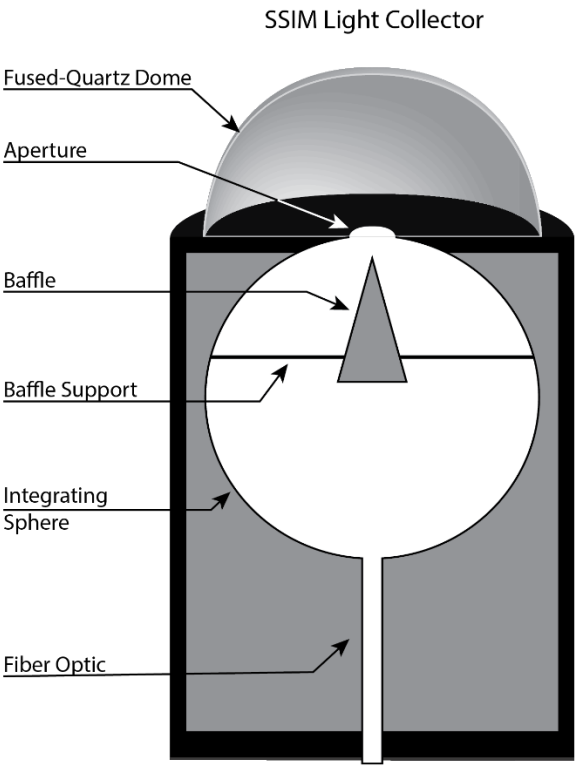

Figure 2.2: Cross-section of the SSIM light collector

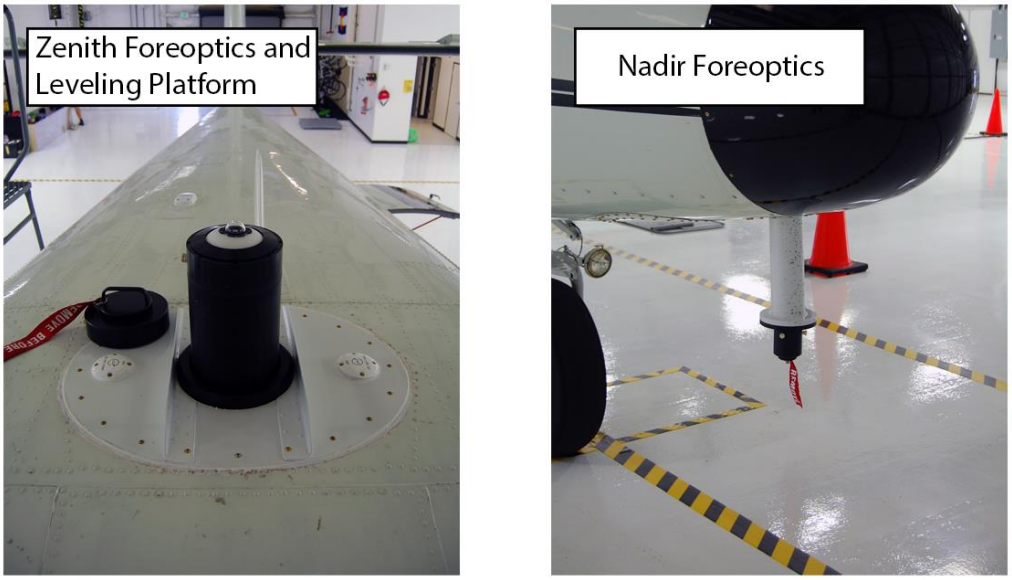

Figure 2.3: Photographs showing the SSIM foreoptics installed on the NEON Twin Otter. The zenith pointing light collector includes the leveling platform and is located mid-fuselage. The nadir light collector is fixed and mounted below the aircraft's nose.

2.2. Leveling Platform

The leveling platform maintains the light collector parallel to the Earth horizon independent of aircraft attitude changes. This improves data quality by reducing frequency of the non-horizontal light collector orientations due to aircraft motion and eliminates the need for corrections in post-processing (Bucholtz et al., 2008; Wendisch et al., 2001). Implementations of solar flux radiometers on many prior flight missions routinely discarded data when aircraft attitude exceeded a threshold deviation from horizontal (Bucholtz et al., 2008; Wendisch et al., 2001). Even the data that passed the threshold required post-processing corrections for sensor misalignment geometry (Wendisch et al., 2001). Thresholding techniques resulted in the loss of large amounts of data (Bucholtz et al., 2008; Wendisch et al., 2001) and correcting even small pitch and roll offsets still produced data with large uncertainties. Moreover, software corrections are of limited value when clouds are present because of the unknown angular dependent scattering from the cloud field (Wendisch et al., 2001).

The SSIM leveling system uses the aircraft inertial navigation system and GPS to control a motor driven stage that adjusts to counter the aircraft pitch and roll. Leveling maintains the light collector's horizontal orientation during pitch and roll maneuvers of up to ±7°. Active leveling results in usable data not only during steady flight at a fixed pitch, but also throughout any aircraft maneuvers or turbulence-induced motions within this angular range. Figure 2.4 shows an example of the aircraft attitude during the collection of a NEON Imaging Spectrometer flight line. The resulting time series of irradiance at 582.8 nm shows very small deviations from the mean (Figure 2.4, bottom panel). During this collection pitch and roll varied by ±5° while the irradiance remained stable and independent of aircraft attitude. The irradiance time series has a standard deviation less than 0.5% and a maximum deviation of 1.6%. An un-stabilized instrument would

observe a 4.5% change in irradiance for a 5° roll given the solar zenith angle when these data were collected. Aircraft maneuvers outside of a 7° range may occur during ascents, descents, changes in heading, and very turbulent conditions, but are uncommon during the normal acquisition of imaging spectrometer data.

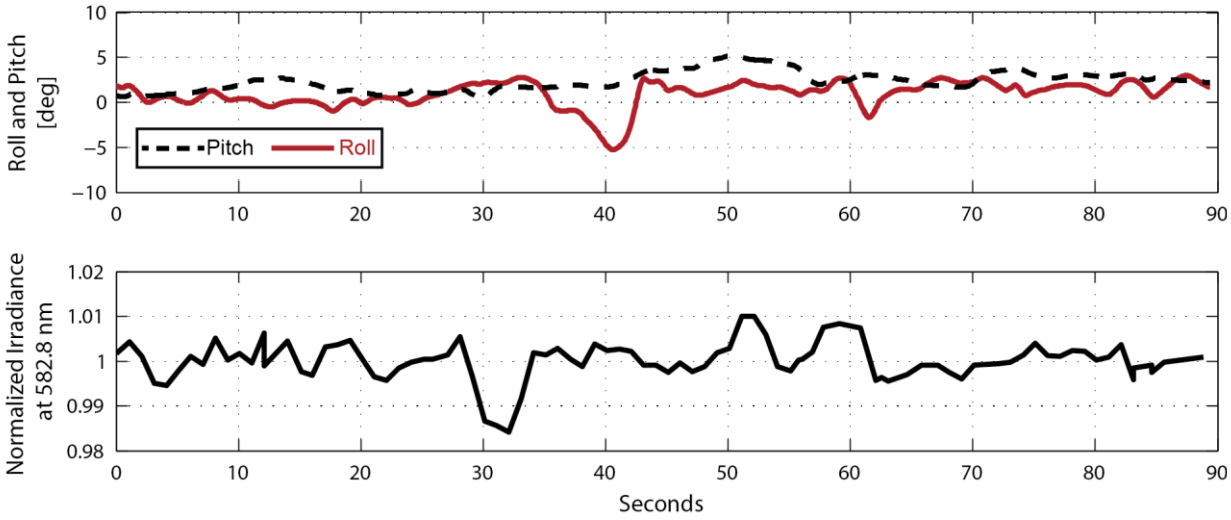

Figure 2.4: Aircraft roll and pitch for a single flight line are plotted in the top panel. Aircraft attitude varied by ± 5° during this 90-second-long collection. The bottom panel shows a single irradiance channel over the same time period. Each division is 1%.

2.3. Azimuthal Response

Previous generations of light-collectors developed at LASP had four narrow metal legs supported the baffle and connected it to the sides of the light collector (Figure 2.5, top). These legs produced azimuthal artifacts in the observations with throughput dropping by up to 10% when a leg was aligned with the direction of incident light (Figure 2.6, bottom). Even when the light collector's angular response is known, azimuthal effects are difficult to correct because the angular distribution of incident radiation field is unknown. Measurement uncertainty due to azimuthal biases would be especially large when observing irradiance in a cloudy or aerosol-laden

atmosphere with that further complicates the radiation field by increasing the amount of diffuse radiation relative to direct solar radiation.

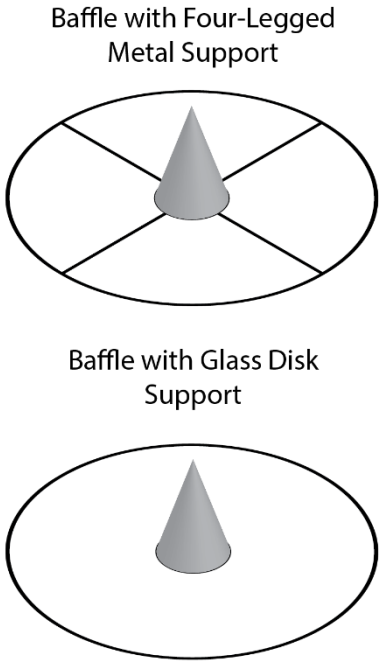

Figure 2.5: Light collector baffle support designs.

To remove the azimuthal dependence, the four-legged metal baffle support was replaced with a glass disk (Figure 2.5, bottom). This redesign eliminated the azimuthal dependency of the light collectors with negligible loss of signal. Figure 2.6 shows the normalized signal at a single wavelength collected through the SSIM foreoptic. The data were collected at 5° increments in azimuth and for several zenith angles. The four-lobed azimuthal features of the metal baffle support are seen for solar zenith angles between 20° and 50°. At solar zenith angles smaller than 20° the metal baffle support does not produce noticeable azimuthal effects. The light-collectors with a glass disk baffle support have a consistent azimuthal response across this range of zenith angles. Data collected at 10°, 20°, and40° zenith angles are shown in Figure 2.6. The left panel shows a four-lobed pattern in the normalized signal observed by the original foreoptic. The dips in signal correspond with the legs of the baffle support. The light collector with the glass baffle support had smaller variations with azimuthal orientation with deviations from the mean of less than 0.5% over all azimuthal angles.

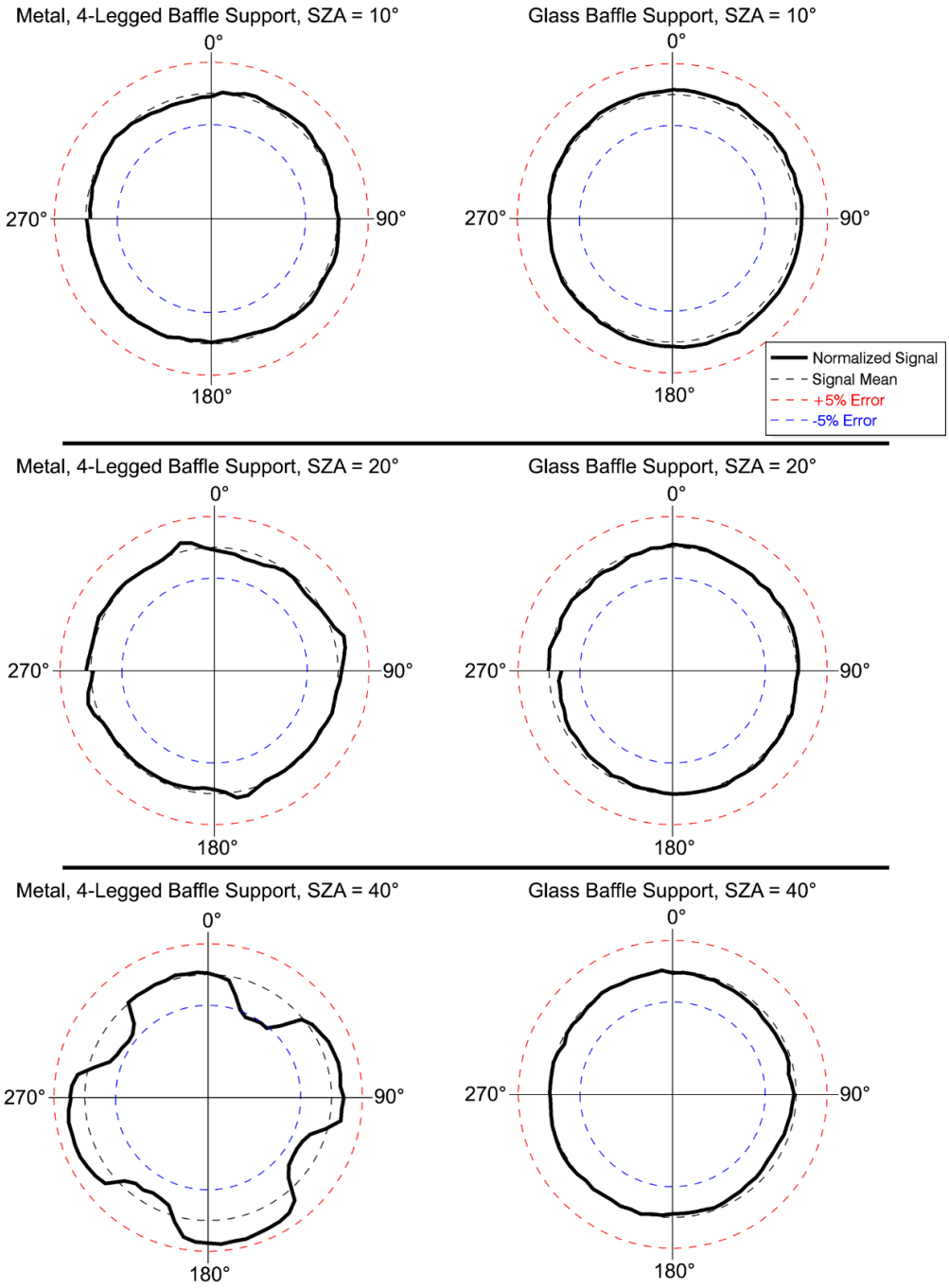

Figure 2.6: Observed signal, normalized to the mean, as the light collector was rotated azimuthally from 0 to 360°.
The black dashed line is the azimuthally averaged signal while the red and blue dashed lines are plus and minus 5% of the mean, respectively. The data were collected with a light source at several zenith angles, plots are shown for solar zenith angles (SZA) of 10° (top row), 20° (middle row), and 40° (bottom row). The panels show the normalized azimuthal response of a light collector including a metal baffle support (left) and a light collector with a glass baffle support (right).

2.4. Temperature Control

The detectors used by the SSIM spectrometers are temperature sensitive. Higher temperatures can increase the baseline *dark signal* that is detected in the absence of any incident light and the *noise* that is present in both the dark signal and light measurements. In normal data collection, the SSIM periodically closes a shutter to make dark measurements throughout the course of a flight. The measured dark signal is subtracted from the open shutter observations to correct the signal. Temperature changes that occur between dark measurements are more difficult to correct. Therefore, it is important to maintain the spectrometer detectors at a stable temperature. Temperature effects are present in both the Si spectrometer and the InGaAs spectrometers, but are stronger in the near-infrared InGaAs detector. Because of their sensitivity to thermal effects, the manufacturer packages InGaAs spectrometers with a two-stage thermoelectric cooler to maintain the detector at -10 °C. These tests validated this built-in system. The InGaAs detector array remained at -10.30 ± 0.03 °C at environmental temperatures from 10 to 35 °C. However, this built-in temperature control only cools the detector array. Temperature changes in the body of the InGaAs spectrometer are not controlled and can be observed in the dark signal. This is not detector noise but the response of the detectors elements to emission at the longest wavelength limit of detector response (greater than 2 μm) from the instrument enclosure.

The SSIM has an additional level of control to stabilize the thermal environment for the spectrometers. An insulated enclosure houses the spectrometers. Within the housing the spectrometers are attached to a common aluminum mounting plate. The plate's temperature is controlled by two thermoelectric coolers that expel waste heat with a fan-cooled heat sink to the exterior of the spectrometer enclosure. The system was tested in the Laboratory for Atmospheric and Space Physics' (LASP) thermal test facility. Environmental temperature was varied between

10 ºC and 35 ºC. The spectrometer thermal control system was set to maintain the central plate temperature at 20 ºC. The spectrometer was operated in the chamber for 50 minutes at each temperature. Figure 2.7 shows the set-temperature of the thermal chamber, the temperature of the InGaAs spectrometer, and an external temperature that was measured inside the SSIM but outside of the cooled spectrometer enclosure.

The performance of the cooling system was evaluated during the final 20 minutes of data collection at each temperature, when the system had equilibrated. The cooling system reduced the change in the InGaAs spectrometer's body to 1.6 ºC per 10 ºC of environmental temperature change, a reduction of 84% from the uncontrolled change. The system also provided stable temperature control throughout testing. The coefficient of variation (the ratio of standard deviation to the mean) of the spectrometer temperature was less than 0.45% at any temperature.

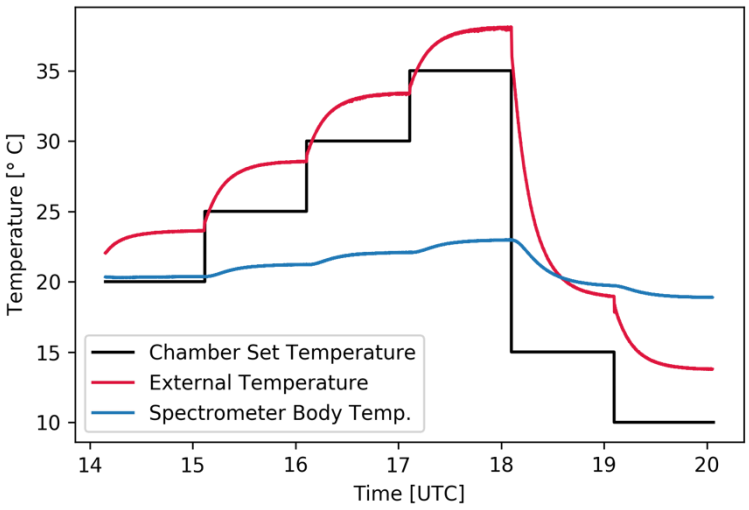

Figure 2.7: SSIM temperatures during thermal testing. The black line is the set-temperature of the thermal chamber. The temperature of the exterior of the InGaAs spectrometer is shown in blue. The red line is the temperature of the analog-to-digital converter module which was not temperature controlled.

2.5. SSIM Calibration

Spectral and radiometric calibrations were performed on the SSIM before the instrument was installed on the aircraft. Spectral calibration was performed using a mercury lamp line source. The emission spectrum of mercury gas was then compared with the spectra recorded with the SSIM to produce a spectral calibration (Pilewskie et al., 2003). Radiometric calibrations were

made prior to the instrument's integration onto the aircraft at the Atmospheric Radiation Laboratory at LASP (Pilewskie et al., 2003). This calibration employed a 1000 W FEL lamp traceable to National Institute of Standards and Technology (NIST) standards (Yoon et al., 2002). The measurement was repeated for a post-deployment calibration after the instrument was de-integrated.

While the laboratory measurements provide a primary calibration, it is necessary to monitor the radiometric calibration of the SSIM throughout the observation campaign. Changes to the instrument response are possible due to events such as modifications to the routing of the fiber optic cable connecting the spectrometer to light collector, or the unlikely breakage of one or more of the fibers within the fiber optic bundle. The CU LASP group has developed a universal field calibrator (Figure 2.8) to track any changes in radiometric calibration over the course of a field campaign. The field calibrator employs two 150 W halogen tungsten lamps used in rotation to account for changes in lamp output in addition to changes in SSIM response. Before and after field deployment the primary 1000 W FEL lamp calibration is transferred to the field

Figure 2.8: Universal field calibrator installed on the SSIM nadir light collector.
Calibrations were made in the hangar while the SSIM was installed on the NEON Twin Otter. An opaque two-layered black shroud (not pictured) covers the light collector and calibrator when in use.

lamps. Previous field experience with these instruments have demonstrated that the SSIM system is generally stable to within ~1% over a month (Pilewskie et al., 2003).

The field calibrator is necessary to detect and correct for any changes. Figure 2.9 shows the instrument response function, relative to the mean primary calibration, for the zenith-viewing silicon spectrometer. The coefficients were derived from seven calibrations of the SSIM, including pre- and post-flight primary calibrations in LASP's Atmospheric Radiation Laboratory, and five mid-campaign field calibrations. Figure 2.9 demonstrates the importance of field calibration, given the discrepancies between the laboratory and field coefficients. It also demonstrates that changes to the instrument's calibration generally occur in large discrete jumps that are usually associated with instrument installation or hardware modifications, such as modifying the route of the fiber optic cable or the breaking of a fiber within the fiber optic bundle. In this figure, two jumps are obvious. One occurred during installation. This is seen in the change between the black pre-campaign primary calibration and the June 2 field calibration. Another jump, most likely due to changing the fiber optic routing, occurred between the June 2 and June 9 field calibrations. After this change, the

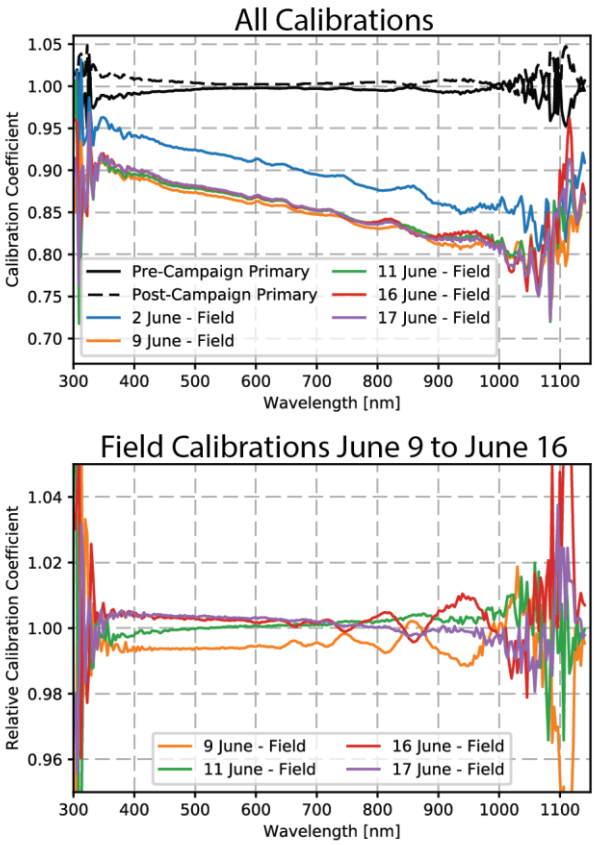

Figure 2.9: SSIM Calibration Coefficients. (Top) Calibration coefficients relative to the mean of the primary calibrations. Primary calibrations are in black and field calibration coefficients are shown with colored lines. (Bottom) Calibration coefficients for field calibrations made between June 9 and June 16 relative to the mean of the four calibrations.

field calibration coefficients from June 9 until the end of the field campaign remained within 1.05% of the mean of the four calibrations for the wavelengths from 350 nm to 980 nm (Figure 2.9, bottom panel). Data at wavelengths shorter than 350 nm are usually excluded due to low signal to noise ratio (SNR) of the detector at the limit of its spectral response. The spectra from the Si and InGaAs spectrometers are typically merged at 980 nm, the intersection of decreasing SNR for the two detectors response limits.

2.6. Acknowledgements

The development of the SSIM was supported by the National Science Foundation under Grants DBI-0752017 and sub-award NEON 1010-214-AOP.

The predecessor of the NEON SSIM leveling platform sub-system was originally developed for the NASA aircraft ER-2 under grant NNX10AV05G from NASA's Earth Science Technology Office, and later adapted for the NASA C-130 aircraft under NNX12AC11G (NASA's Radiation Science Program), which also funded the development of the spectrometer sub-system. A sibling of the SSIM including the spectrometer and leveling platform components was flown during the NASA ARISE experiment (Smith et al., 2017).

Chapter 3

Below-Cloud Atmospheric Correction of Airborne Hyperspectral Imagery Using Simultaneous Solar Spectral Irradiance Observations

3.1. Abstract

Retrieving surface properties from airborne hyperspectral imagery requires the use of an atmospheric correction model to compensate for atmospheric scattering and absorption. In this study a Solar Spectral Irradiance Monitor (SSIM) from the University of Colorado Boulder was flown on a Twin Otter aircraft with the National Ecological Observatory Network's (NEON) imaging spectrometer. Up- and down-welling irradiance observations from the SSIM were used as boundary conditions for the radiative transfer model used to atmospherically correct NEON imaging spectrometer data. Using simultaneous irradiance observations as boundary conditions removed the need to model the entire atmospheric column so that atmospheric correction required modeling only the atmosphere below the aircraft. For overcast conditions, incorporating SSIM observations into the atmospheric correction process reduced error in retrieved surface reflectance by up to 57%. In addition, upwelling irradiance measurements were used to produce an observation-based estimate of the adjacency effect, improving surface reflectance retrievals, under cloud-free conditions, by up to 27%.

3.2. Introduction

Hyperspectral imagers, also known as imaging spectrometers, acquire radiance spectra in contiguous and overlapping wavelength channels for each spatial pixel in a scene (Goetz et al., 1985). The large numbers of spectral channels provide the opportunity to develop hyperspectral processing methods and science products that exploit more spectral information than the relatively few channels of multispectral instruments. However, more sophisticated analytic techniques are required to effectively exploit the additional spectral information. Signal unmixing, biophysical vegetation property retrieval, and some atmospheric correction methods, all may benefit from the increased information provided by hyperspectral data (Goetz, 2009). Taking advantage of these benefits, imaging spectrometers are used to produce many diverse surface data products making them a valuable tool for a wide variety of research topics including geological, ecological and agricultural studies. Imaging spectrometers are also now beginning to support operational programs (Kampe, Asner, et al., 2010).

Deriving surface products from imaging spectrometer data requires *atmospheric correction* to remove the influence of the atmosphere from the observations (B.-C. Gao et al., 2009). This step generally uses radiative transfer models to derive atmospheric extinction in order to calculate the surface reflectance from aircraft or spacecraft measured spectral radiance. Conventional atmospheric correction techniques assume a cloud-free atmosphere, severely limiting the flight conditions to which they can be applied. This places a constraint on observation campaigns that may lead to: long delays in flights, smaller datasets than would arise from collecting in cloudy and cloud-free conditions, reduced frequency of resampling flights, or reduced data quality from collecting in sub-optimal conditions.

We present a method for retrieving surface reflectance below clouds, or in otherwise marginal atmospheric conditions, using coincident airborne observations of up- and down-welling irradiance. This method extends the concept of using irradiance measurements for atmospheric correction from earlier work that used ground based irradiance observations to improve atmospheric correction (Goetz et al., 1998). By using only imagery and irradiance observations from the aircraft we collect all the data required for continuous atmospheric correction throughout the flight without the need for ground sites. We also demonstrate the use of upwelling irradiance observations to estimate the *adjacency effect*, which is defined as the signal reflected from surface regions other than the desired target that is then scattered into the sensor. Quantifying the adjacency effect is not possible with exclusively ground-based observations. The data presented in this study were collected during a June 2015 flight campaign of the National Ecological Observatory Network's (NEON) Twin Otter aircraft equipped with the NEON Imaging Spectrometer (NIS) and the University of Colorado Boulder Solar Spectral Irradiance Monitor (SSIM).

3.3. Background

3.3.1. Atmospheric Correction

The goal of the NEON Airborne Observation Program (AOP) is to produce remotely sensed terrestrial ecological data products (Kampe, Johnson, Kuester, & Keller, 2010). The AOP is one component of NEON's strategy to produce a long-term record of ecological change in the United States using fixed and relocatable ground sites, and airborne data. Airborne observations complement ground-based data by extending NEON's long-term data record to larger regions surrounding the ground sites. Producing these ecological data products requires observations of surface reflectance, whereas the NIS acquires reflected radiance at aircraft flight altitude, known as *at-sensor radiance*. The measured at-sensor radiance includes: the signal from the target

(surface); contributions from molecular scattering; aerosol scattering, including cloud particles; the adjacency effect; and the signal of atmospheric absorption (Figure 3.1). This combination of signals makes it difficult to isolate surface reflectance from atmospheric effects.

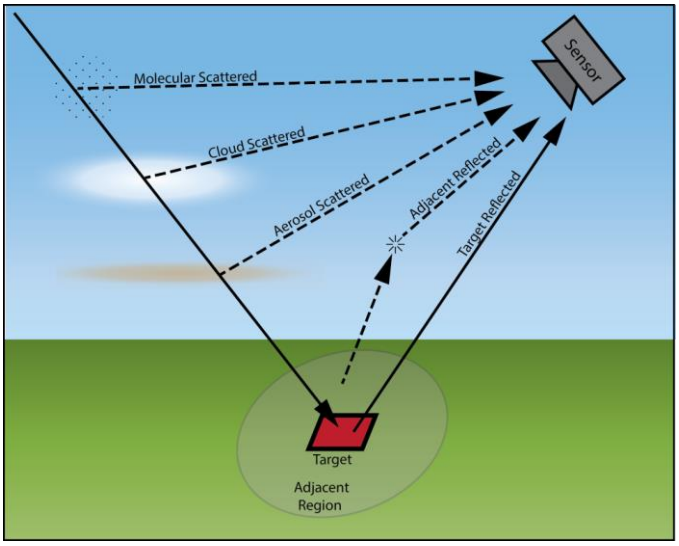

Figure 3.1: Contributions to at-sensor radiance: scattered radiance from the atmosphere, including cloud, aerosol, and molecular scattering; radiance reflected by the surface adjacent to the target; and the radiance reflected by the target (red square).

Atmospheric correction separates these signals by determining the irradiance at the surface and the transmittance between the surface and the flight altitude. The most commonly used methods employ an atmospheric radiative transfer model. Many model-based atmospheric correction routines have been developed to retrieve surface reflectance. Examples include Atmospheric REMoval Program, (ATREM) (B.-C. Gao et al., 1993; Thompson, Gao, et al., 2015), Atmosphere CORrection Now (ACORN) (Kruse, 2004), High-accuracy Atmospheric Correction for Hyperspectral data (HATCH) (Qu et al., 2003), Fast Line-of-sight Atmospheric Analysis of Spectral Hypercubes (FLAASH) (Matthew et al., 2002), and Atmospheric and Topographic Correction (ATCOR) (Richter & Schläpfer, 2002).

Conventional model-based atmospheric correction routines start with two measured or assumed quantities, the top-of-atmosphere (TOA) solar irradiance and radiance observed by the imaging spectrometer. A radiative transfer model uses these quantities to calculate atmospheric radiative properties based on inputs of known (e.g., solar geometry and ground elevation) and estimated (e.g., visibility) atmospheric conditions. The surface reflectance can be calculated by

combining the modeled atmosphere with the TOA solar irradiance and solving for the surface reflectance value that matches the modeled radiance to the measured radiance (B.-C. Gao et al., 2009). More advanced methods of atmospheric correction include the retrieval of atmospheric properties such as column water vapor and aerosol optical thickness and methods for topographic and adjacency effect correction (Richter & Schläpfer, 2015). The specific atmospheric correction process employed by this study is discussed in the Methods section.

3.3.2. Motivation

As we will show, atmospheric correction is a large source of error in hyperspectral remote sensing of surface properties even under ideal conditions. Using existing techniques, cloud-free flight opportunities are required for accurate property retrievals. Sensitivity to atmospheric conditions can be problematic because thin clouds such as cirrus, while difficult to detect, can impact data quality. Figure 3.2 illustrates that clouds above the aircraft can introduce errors in retrieved surface reflectance when atmospheric correction does not account for the cloud-induced reduction in atmospheric transmission. The observed reduction of reflectance by factors of two to five is unlikely to be due to spatial variability across the scene given the homogeneity seen in the true color image. Instead, the changes are almost certainly due to increasing cloud cover that decreases the downwelling irradiance at the surface. The greatest impact due to a cloud-free atmosphere requirement is a reduction in the number of possible flights in a given time. By improving atmospheric correction below clouds, this work aims to increase the number of viable flight opportunities for data collection.

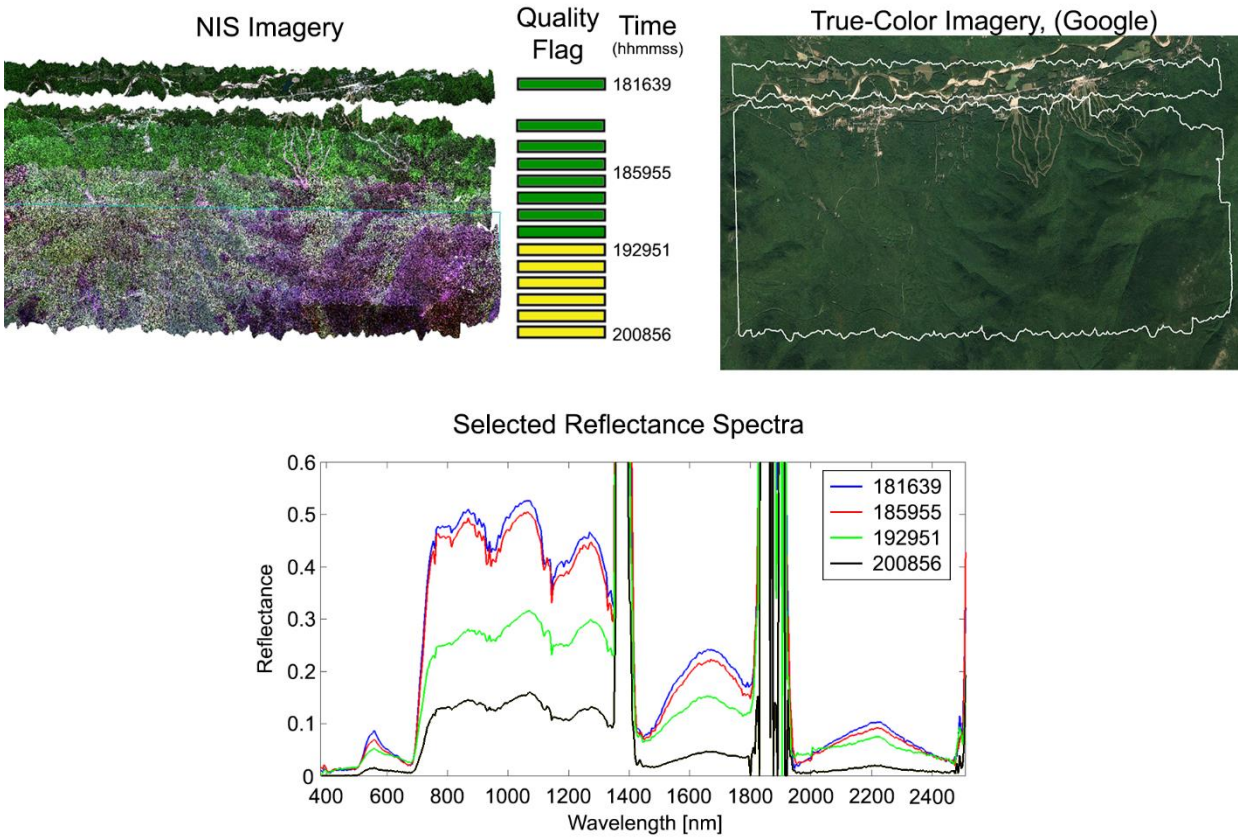

Figure 3.2: Flight lines of Bartlett Forest on June 2, 2014 (top left panel).
Flight lines were acquired sequentially from top to bottom. Increasing cirrus cloud cover was recorded as the airborne survey progressed; resulting in a reduction in flight line quality from green to yellow (top panel, right). The collection times for select flight lines are shown as GPS time stamps (hhmmss) recording the time the flight lines were acquired. The true color image, imagery from Google, shows the uniformity of vegetation over this scene. The bottom panel shows retrieved spectral reflectances for single pixels containing similar vegetation for the flight lines shown in the top panel. As time progresses, the increasing cirrus cloud cover reduced the magnitude of retrieved spectral reflectance, which should have remained constant. The large spikes in reflectance centered on 1380 and 1900 nm are due to the strong water vapor absorption bands in those wavelengths. (Figure courtesy of Tristan Goulden, Battelle Ecology Inc./NEON Project)

Ground-based observations of downwelling irradiance or surface reflectance may also improve atmospheric correction. Ground site measurements of spectral reflectance or irradiance may help to remove systematic errors in the retrieved surface reflectance due to the atmospheric correction method or instrument error (Baugh & Groeneveld, 2008; Goetz et al., 1998). These techniques have drawbacks. Ground sites require the deployment of additional personnel and

equipment on the ground; a costly and logistically challenging option for an operational system. Moreover, surface measurements are limited spatially compared to the much larger region of varying atmospheric conditions sampled by aircraft.

Simultaneous airborne observations of irradiance address these current limitations by reducing the number of model atmospheric assumptions, providing continuous information on the atmospheric conditions above the aircraft, and providing an airborne reference measurement which can complement ground sites for detecting systematic errors. Commercial airborne instruments are available for measuring downwelling irradiance, for example, Specim Ltd.'s Fiber Optic Downwelling Irradiance Sensor (FODIS). The intended use of this instrument is to derive apparent reflectance at the sensor level (Homolova et al., 2009). Unfortunately this instrument lacks a stabilizing system, the angular calibration/characterization, and radiative transfer modeling required for robust atmospheric correction (Homolova et al., 2009).

Atmospheric correction accuracy is highly dependent on the accuracy of the radiative transfer model. Model errors reduce the accuracy of retrieved surface reflectance in otherwise ideal conditions. For example, a commonly employed commercially available routine, ATCOR, can have model uncertainties of 0.02 to 0.04 reflectance units (Richter & Schläpfer, 2015). However, these uncertainty levels are realized only with perfect knowledge of aerosol and cloud conditions. Using downwelling irradiance observations as a model boundary condition rather than TOA solar irradiance removes the need to assume atmospheric properties above flight level; only the dotted region in Figure 3.3 remains to be modeled.

In a hyperspectral image, changes in surface reflectance and changing illumination can appear as equivalent changes in the observed radiance. Airborne irradiance measurements can be used to resolve this ambiguity and separate the two signals. This problem is minor for instruments

such as the Airborne Visible/Infrared Imaging Spectrometer (AVIRIS) (Green et al., 1998) when flown aboard the high altitude NASA ER-2 (nominal 20 km flight altitude) and is non-existent for satellite instruments because there is very little or no atmosphere above these instruments. However, for a low-flying instrument, such as the NIS flying at one kilometer above ground level, employing a radiative transfer model with assumed above-aircraft atmospheric transmittance could produce a significant difference between observed and modeled flight-altitude irradiances.

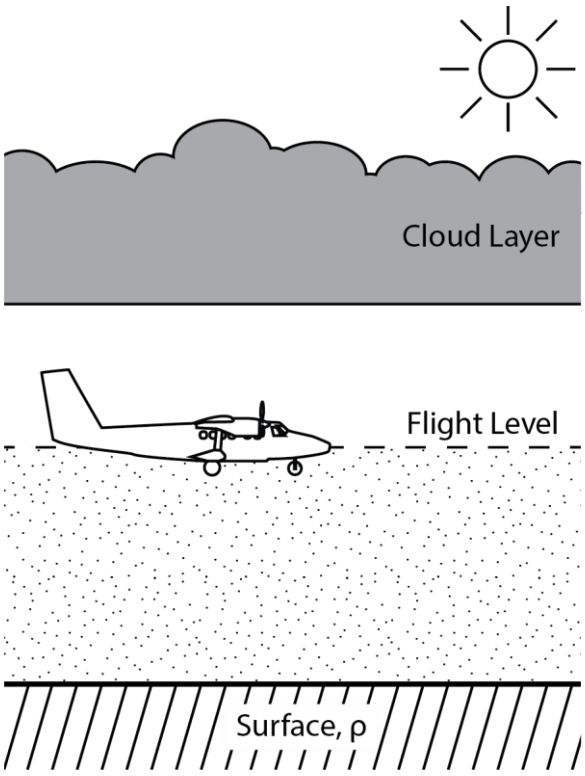

Figure 3.3: The below cloud observations scenario.
Radiance and irradiance observations are made at the aircraft. Using irradiance measurements only the dotted region must be modeled for atmospheric correction.

To demonstrate the magnitude of the error introduced into surface reflectance retrievals by assuming a cloud-free atmosphere in the presence of clouds we have modeled this scenario for an aircraft at one kilometer above the ground with several thicknesses of cirrus clouds (Figure 3.4). The downwelling irradiance and atmospheric transmittance were modeled with the MODTRAN 5.3 radiative transfer model using its standard cirrus cloud model (Berk et al., 2006, 2013). Even a thin cirrus cloud can introduce significant errors in retrieved surface reflectance. The resulting errors at 550 nm are 5%, when the cirrus optical depth is 1.0. Additionally, inhomogeneous cloud fields can have rapidly varying illumination conditions, further reducing the usefulness of fixed atmospheric transmittance assumptions. With an overlying cloud layer, the uncertainty in the

retrieval model exceeds the measurement error. Simultaneous observations of the downwelling irradiance provide the information on atmospheric conditions above the aircraft that is necessary for reducing this error.

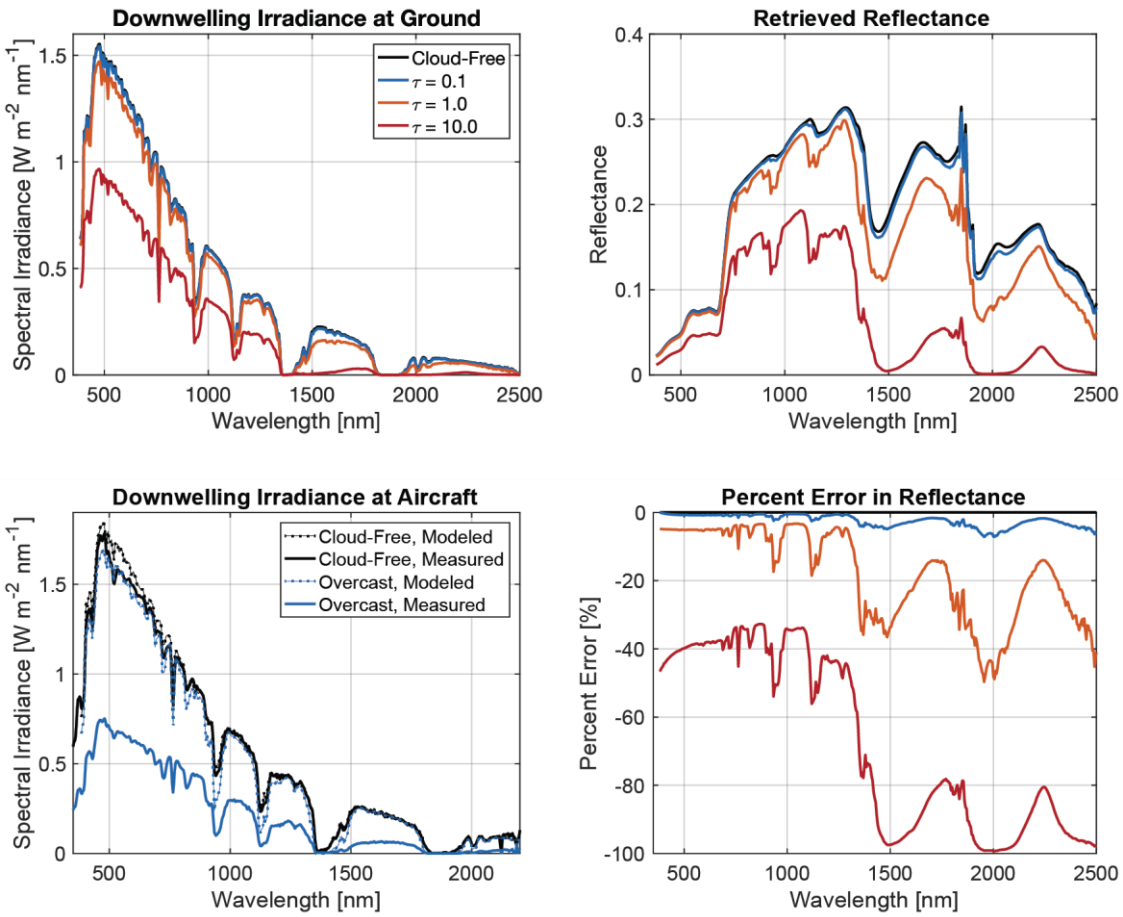

Figure 3.4: Modeled irradiance at the surface (top left), corresponding surface reflectance retrievals (top right), and the error in the retrieved reflectance (bottom right) for four atmospheric cases: a cloud-free atmosphere and cirrus clouds of 0.1, 1.0 and 10 optical thicknesses. In all four cases the surface reflectances were retrieved assuming a cloud-free atmosphere. This assumption results in the shown retrieval error. Optical depth values refer to the optical depth at 550 nm. The final panel (bottom left) shows the difference between modeled (dotted lines) and measured (solid lines) downwelling irradiance spectra collected in cloud free (June 8) and overcast conditions (June 16).

3.4. Instrumentation

The data used for this study were collected during a flight campaign of the NEON Twin Otter in June 2015 based at the Boulder Municipal Airport in Boulder, Colorado. The instrument

payload included the NEON Imaging Spectrometer and the University of Colorado Boulder Solar Spectral Irradiance Monitor. Flights were conducted in a variety of atmospheric conditions over four days with cloud-free, partly cloudy, and full overcast flight opportunities (Figure 3.5). Calibrated reference targets were deployed at the National Oceanic and Atmospheric Administration Table Mountain Facility outside of Boulder, Colorado (https://www.esrl.noaa.gov/gmd/grad/calfacil/tmtf.html) located at 40.125° latitude, 105.237° longitude, and at an altitude of 1689 meters (Figure 3.6).

Figure 3.5: Sky conditions for the three flight days examined in this study.
From left-to-right, cloud-free on June 8, 2015, overcast on June 16, 2015, and partial cloud cover on June 17, 2015. In two of the photographs the reflectance reference targets, white and black, are visible. In the center photo the Twin Otter aircraft is visible overflying the ground site below a cloud layer on June 16.

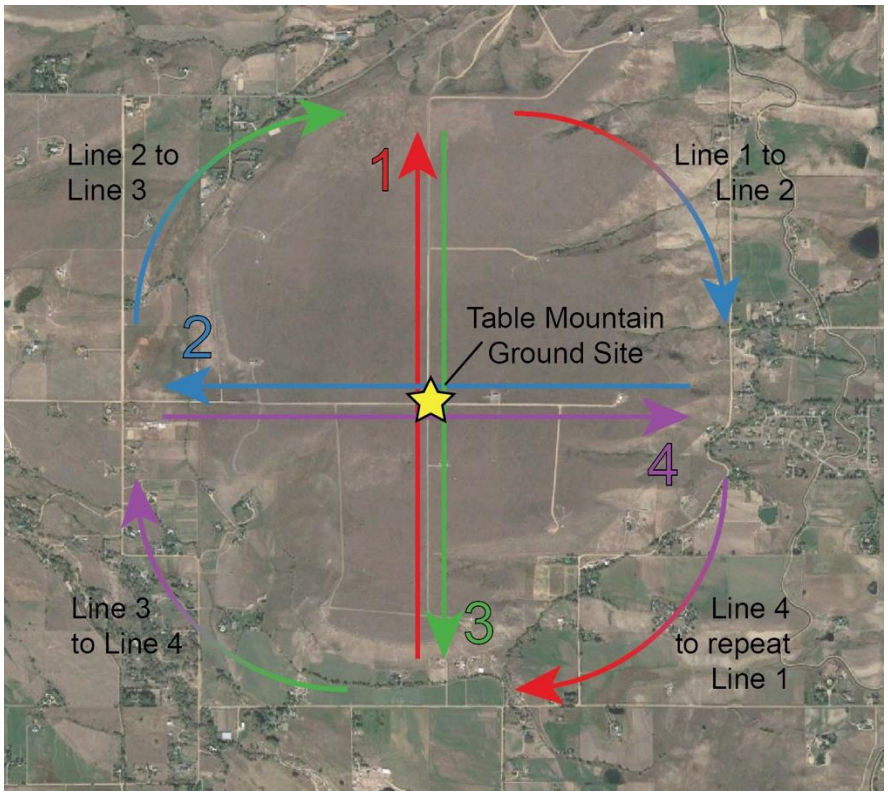

Figure 3.6. NEON planned flight lines over the NOAA Table Mountain Test site.
This pattern was collected at least once on each of the flight days. Airborne observations were supported by ground based validation data collected at the marked Table Mountain ground site. (Imagery and Map Data: Google).

3.4.1. NEON Imaging Spectrometer (NIS)

Figure 3.7: NIS image flight tracks at 1 m resolution overlaying AVIRIS 18 m imagery (Kampe et al., 2013)

The NIS is a hyperspectral imaging spectrometer developed for NEON by the Jet Propulsion Laboratory, and has been previously described in Johnson et al., 2010 and Kampe, Asner, Green, Eastwood, et al., 2010. The NIS has 426 wavelength bands in the region from 380 nm to 2510 nm with a spectral sampling of 5 nm and a full-width half-maximum (FWHM) spectral resolution of 1 to 1.5 times the spectral sampling interval. A single

spectrometer with a two-dimensional detector array is operated in a pushbroom mode that produces greater signal to noise ratio (SNR) than would be achieved with a whiskbroom scanner (Johnson et al., 2010). The entire imaging spectrometer is housed in a vacuum chamber cooled to below 150 K to minimize detector dark current and background emission from the instrument optics. The NIS is flown at altitudes between 1 and 3 km. An instantaneous field-of-view of 1 milliradian results in a ground resolution of 1 to 3 m and a ground swath 600 to 1800 m wide depending on the flight altitude. The NIS has a stated 1-σ radiometric accuracy of greater than 95% (Johnson et al., 2010).

3.4.2. Solar Spectral Irradiance Monitor (SSIM)

The SSIM is an airborne spectral irradiance radiometer built by the University of Colorado Laboratory for Atmospheric and Space Physics. The system measures both up- and downwelling spectral irradiance for the wavelength range from 350-2150 nm. The instrument consists of a spectrometer module mounted in the aircraft which is coupled by fiber optic cables to foreoptics mounted on the exterior of the aircraft. A leveling platform maintains the foreoptics oriented parallel to the Earth horizon for aircraft movements and turbulence of less than ±7º. Chapter 2 describes the SSIM instrument in detail.

3.5. Methods

Atmospheric correction requires relating the NIS radiance to known quantities using a radiative transfer model. In this study the MODTRAN version 5.3 (Berk et al., 2006, 2013) radiative transfer model is employed for this purpose. MODTRAN is often used as the radiative transfer core of atmospheric correction routines as in ACORN (Kruse, 2004) and ATCOR (Richter & Schläpfer, 2015). Beginning with version 5.1 MODTRAN introduced the option to output an atmospheric correction data (acd) file (Berk & Anderson, 2008). The acd output file simplifies the

correction process by producing the transmittance and spherical albedo values necessary to perform an atmospheric correction in a single model run.

In this section, we describe the standard retrieval process for surface reflectance when only imaging spectrometer radiance measurements are available. The retrieval is then extended to include the irradiance measurements.

3.5.1. Standard Atmospheric Correction

A standard atmospheric correction relates the observed at-sensor radiance to the known TOA solar irradiance using the radiative transfer model. MODTRAN model runs are required to describe the radiative properties over the path from the top of the atmosphere to the surface and back to the aircraft altitude. The surface is assumed to be flat and a perfect diffuse reflector. Therefore, the method retrieves a surface reflectance scaled to that from an idealized, Lambertian, surface (B.-C. Gao et al., 1993; Richter & Schläpfer, 2002; Schaepman-Strub et al., 2006; Thompson, Gao, et al., 2015). For simplicity, scaled surface reflectance will be referred to as surface reflectance.

The at-sensor radiance, $\langle L \rangle_\lambda$, is comprised of three terms: path radiance, $\langle L_0 \rangle_\lambda$, direct radiance, $\langle L_T \rangle_\lambda$, and the adjacency radiance, $\langle L_t \rangle_\lambda$ (Eq. **(3.1)**). These equations are for monochromatic light and each quantity is normalized to an instrument's spectral response function. These normalized quantities are defined in Eq. **(3.2)** and denoted by brackets ($\langle \quad \rangle_\lambda$) (Berk et al., 2013).

$$\langle L \rangle_\lambda \approx \langle L_0 \rangle_\lambda + \langle L_T \rangle_\lambda + \langle L_t \rangle_\lambda \tag{3.1}$$

$$\langle x \rangle_\lambda \equiv \int_\lambda x(\lambda) f(\lambda) d\lambda \tag{3.2}$$

These radiance terms are either direct MODTRAN outputs, $\langle L_0 \rangle_\lambda$, or are calculated, $\langle L_T \rangle_\lambda$ and $\langle L_t \rangle_\lambda$, from the following six output quantities:

- **Path Radiance (L_0):** The contribution of atmospheric scattering alone, this term is the radiance that would be present if there were no surface or a completely absorbing surface below the atmosphere.
- **Sun-to-ground diffuse transmittance (t_s):** The fraction of incident radiation that passes through the atmosphere with at least one scattering event.
- **Sun-to-ground-to-observer direct transmittance (T_{so}):** The fraction of incident radiation directly transmitted through the atmosphere, reflected by the surface, and directly transmitted to the observer.
- **Sensor-to-ground embedded diffuse transmittance (t):** The fraction of radiation scattered into the direction of the sensor by the atmosphere when the sensor is located within the atmosphere.
- **Sensor-to-ground direct transmittance (T):** The fraction of radiation leaving the surface and passing to the sensor without being scattered.
- **Spherical albedo (σ):** The fraction of radiation leaving the surface that is scattered back to the surface by the atmosphere.

The first of the terms, path radiance, $\langle L_0 \rangle_\lambda$, is output directly from MODTRAN. Direct radiance, $\langle L_T \rangle_\lambda$, is the portion of the incident radiation that scatters off of the observed target and is transmitted directly to the sensor. The term is calculated from the transmittances, spherical albedo and TOA solar irradiance (F_0) by Eq. **(3.3)**. The final term, adjacency radiance, $\langle L_t \rangle_\lambda$, is the contribution from radiation reflected from the surface in the neighborhood of the target and then scattered to the sensor; it is calculated by Eq. **(3.4)**. The adjacency term is defined by a

neighborhood surface reflectance, $\bar{\rho}_\lambda$, which is an average of the surface reflectance within the observed pixel's neighborhood. The size of the relevant neighborhood, also known as *adjacency range*, varies with atmospheric conditions and on instrument altitude (Richter et al., 2006). Substituting Eqs. **(3.3)** and **(3.4)** into Eq. **(3.1)** produces the desired relationship between radiance observations and model outputs (Eq. **(3.5)**). Eqs. **(3.3)**, **(3.4)**, and **(3.5)**, relating observed radiance and TOA irradiance through the MODTRAN atmospheric correction outputs are adapted from the MODTRAN documentation (Berk et al., 2013).

$$\langle L_T \rangle_\lambda = \frac{\mu F_0 \langle (T_s + t_s) T \rangle_\lambda}{\pi} \frac{\rho_\lambda}{1 - \langle \sigma \rangle_\lambda \bar{\rho}_\lambda} \quad \textbf{(3.3)}$$

$$\langle L_t \rangle_\lambda = \frac{\mu F_0 \langle (T_s + t_s) t \rangle_\lambda}{\pi} \frac{\bar{\rho}_\lambda}{1 - \langle \sigma \rangle_\lambda \bar{\rho}_\lambda} \quad \textbf{(3.4)}$$

$$\langle L \rangle_\lambda \approx \langle L_0 \rangle_\lambda + \frac{\mu F_0 \langle (T_s + t_s) T \rangle_\lambda}{\pi} \frac{\rho_\lambda}{1 - \langle \sigma \rangle_\lambda \bar{\rho}_\lambda} + \frac{\mu F_0 \langle (T_s + t_s) t \rangle_\lambda}{\pi} \frac{\bar{\rho}_\lambda}{1 - \langle \sigma \rangle_\lambda \bar{\rho}_\lambda} \quad \textbf{(3.5)}$$

In Eqs. **(3.3)**, **(3.4)** and **(3.5)**, $\langle \sigma \rangle_\lambda$, is the spherical albedo convolved with the channel spectral response function and μ is the cosine of solar zenith angle, θ. The final term, T_s, is the direct sun-to-ground transmittance calculated from the model outputs where $T_s = T_{so}/T$. In this simple standard atmospheric correction we ignore the adjacency effect, assuming that $\rho_\lambda \approx \bar{\rho}_\lambda$. With this assumption, we solve Eq. **(3.1)** for surface reflectance:

$$\rho_\lambda = \frac{\pi(\langle L \rangle_\lambda - \langle L_0 \rangle_\lambda)}{\langle \sigma \rangle_\lambda \pi(\langle L \rangle_\lambda - \langle L_0 \rangle_\lambda) + \mu F_0 \langle (T_s + t_s)(T + t) \rangle_\lambda} \quad \textbf{(3.6)}$$

3.5.2. Enhanced Atmospheric Correction

Irradiance observations can be incorporated into the atmospheric correction process with a few modifications to the standard method described in the previous section. Incorporating the irradiance measurements avoids assumptions of atmospheric conditions above the aircraft.

Modeling the atmosphere below the aircraft is still required. Two assumptions are still necessary. The irradiance is assumed to be constant in the across-track direction because aircraft irradiance measurements are only made at the center of the flight track. This assumption could be validated by using the stability of the observed downwelling irradiance as a proxy for the across-track variation. The irradiance recorded when the surface was imaged was used for each retrieval and the two observations were synchronized using the GPS system time. Matching imagery with spectral irradiance acquired when the aircraft was directly above the surface image implies an assumption of horizontal uniformity over a distance between zenith and the actual slant path. For the scenes examined in this study this horizontal offset distance varied from 200 to 515 m. Figure 3.8 illustrates the observing geometry of the aircraft and highlights this horizontal offset. Determining the importance of this offset would require knowledge of the atmospheric conditions above the aircraft. In a cloud-free atmosphere, irradiance may not vary significantly over that distance while scattered clouds could produce substantial changes in downwelling irradiance over those distances.

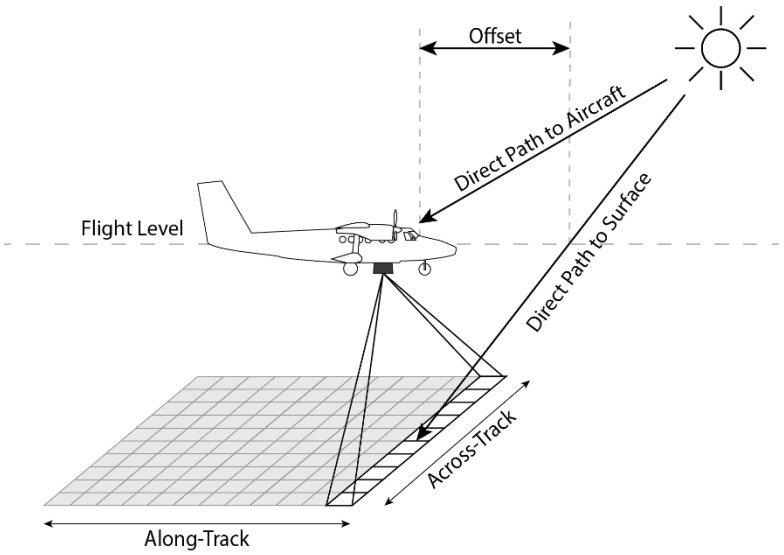

Figure 3.8: A diagram of the observing geometry of the NEON AOP Twin Otter System. The diagram illustrates the horizontal offset the direct solar radiation path that is incident on the surface and the direct solar radiation that is observed at the aircraft.

Eqs. **(3.5)** and **(3.6)** relate the NIS radiance to the TOA irradiance but this relation is less useful for atmospheric correction below clouds if the properties of the atmosphere above the aircraft are not known. Rather than assuming atmospheric extinction above the aircraft, the downwelling irradiance measured with the SSIM can be used in place of the TOA irradiance, requiring a modification of Eq. **(3.6)**. Sun to ground transmittances, T_s and t_s, are replaced with the aircraft to ground transmittances T and t. The spherical albedo value, $\langle\sigma\rangle_\lambda$, is replaced with the spherical albedo of the layer between the ground and flight levels, $\langle\sigma_L\rangle_\lambda$. Additionally, the MODTRAN output path radiance no longer sufficiently represents the observed path radiance because it is dependent on downwelling irradiance. Instead the path radiance is calculated via the atmospheric reflectance (ρ_{a_λ}) which is derived from the cloud-free MODTRAN outputs of path radiance and flight-level downwelling irradiance ($F_{F\downarrow}$) such that $\rho_{a_\lambda} = L_0/F_{F\downarrow}$. The below cloud path radiance is calculated by multiplying ρ_{a_λ} by the SSIM downwelling irradiance. Substituting the observed flight-level downwelling irradiance for TOA irradiance produces Eq. **(3.7)**.

$$\langle L\rangle_\lambda \approx \langle L_0\rangle_\lambda + \frac{F_{F\downarrow}\langle(T+t)T\rangle_\lambda}{\pi}\frac{\rho_\lambda}{1-\langle\sigma_L\rangle_\lambda\bar{\rho}_\lambda} + \frac{F_{F\downarrow}\langle(T+t)t\rangle_\lambda}{\pi}\frac{\bar{\rho}_\lambda}{1-\langle\sigma_L\rangle_\lambda\bar{\rho}_\lambda} \qquad \textbf{(3.7)}$$

At this point we can solve Eq. **(3.7)** for ρ_λ, employing the same assumption, $\rho_\lambda \approx \bar{\rho}_\lambda$, that was employed for the standard retrieval. The resulting surface reflectance is the enhanced atmospheric correction retrieval, without adjacency correction.

In the standard and enhanced retrievals above we ignored the adjacency effect, assuming $\rho_\lambda = \bar{\rho}_\lambda$. However, the SSIM measurement of upwelling irradiance provides a measure of the adjacency effect. The upwelling irradiance expected at the SSIM, ($F_{F\uparrow}$), can be calculated from the observed downwelling irradiance and model outputs, using Eq. **(3.8)**.

$$F_{F\uparrow} = F_{F0} + \frac{F_{F\downarrow}\langle (T+t)^2 \rangle_\lambda \rho_{h_\lambda}}{1 - \langle \sigma_L \rangle_\lambda \rho_{h_\lambda}} \quad \textbf{(3.8)}$$

This relationship is derived from Eq. **(3.5)** by multiplying the diffuse and direct radiance terms by π to transform from radiance to irradiance values, assuming that the surface is a Lambertian reflector. In addition we introduce two new variables: F_{F0}, the irradiance equivalent of path radiance; and ρ_{h_λ}, the hemispherical surface reflectance. Combining the direct and diffuse transmittance terms reduces reflectance to a single term, ρ_{h_λ}. This hemispherical surface reflectance term is the average surface reflectance of the hemispherical field-of-view of the SSIM; it is weighted by both the cosine of the nadir angle and the atmospheric transmittance. This inherent weighting defines the relevant "adjacency neighborhood". The hemispherical surface reflectance can be derived from the upwelling irradiance observations by solving Eq. **(3.8)** for ρ_h.

We can use ρ_{h_λ} as an approximation for the true adjacency surface reflectance, eliminating the assumption that $\bar{\rho}_\lambda = \rho_\lambda$. Then the surface reflectance, ρ_λ, is calculated with the assumption that $\bar{\rho}_\lambda = \rho_{h_\lambda}$, the flight-level downwelling irradiance, $F_{F\downarrow}$, and the model output terms: T, t, $\langle L_0 \rangle_\lambda$, and $\langle \sigma_L \rangle_\lambda$ (Eq. **(3.9)**).

$$\rho_\lambda = \left[\langle L \rangle_\lambda - \langle L_0 \rangle_\lambda - \frac{F_{F\downarrow}\langle (T+t)t \rangle_\lambda}{\pi} \frac{\bar{\rho}_\lambda}{1 - \langle \sigma_L \rangle_\lambda \bar{\rho}_\lambda} \right] \frac{\pi (1 - \langle \sigma_L \rangle_\lambda \bar{\rho}_\lambda)}{F_{F\downarrow}\langle (T+t)T \rangle_\lambda} \quad \textbf{(3.9)}$$

In the results presented below we will refer to this retrieval as the enhanced retrieval with adjacency correction.

3.6. Results

The NEON Twin Otter test flights in June 2015 provided opportunities to test the enhanced atmospheric correction. During this flight campaign SSIM and NIS data were collected from the aircraft. Ground truth reflectance measurements of calibrated reference targets were made at the National Oceanic and Atmospheric Administration Table Mountain Facility outside of Boulder, Colorado. The reference targets were 10 m x 10 m tarps (approximately 100 NIS pixels) with relatively flat spectral reflectances of 0.03 and 0.48 (Figure 3.9). Ground truth spectra were acquired for the tarp targets as well as the vegetation and road surfaces at the ground site. These measurements were made using an PANalytical/ASD FieldSpec 3 field spectrometer (Goetz et al., 1975). We compared these ground site measurements to the surface reflectances retrieved from the NIS observations using the standard and enhanced atmospheric correction methods.

Figure 3.9: True color NIS imagery of the field ground site.
The 0.03 and 0.48 reflectance targets are the black and white squares, respectively. The brown and green rectangles show where the dirt road and vegetation reference spectra were collected. The tarps, road and vegetation regions amount to approximately 400 pixels.

Ground-based surface reflectance measurements were made by observing a NIST traceable calibrated Spectralon reference panel, followed by measurements of the target surface, finishing with another measurement of the reference panel. By comparing the observations of the unknown surface to the known reflectance panel, the unknown reflectance can be derived. However, the incident downwelling irradiance between these two reference panel measurements may be changing, due to varying atmospheric conditions or solar geometry, introducing uncertainty into

the retrieved surface reflectance. An additional source of error in the ground measurements is imperfect spatial sampling, so that slightly different sections of the reference tarps and vegetated surfaces were measured on repeat measurements. These and other possible error sources can result in multiple measurements of the same surface with different reflectance values (Figure 3.10). In cloud-free conditions on June 8, repeated surface reflectance observations produced standard deviations up to 0.025, for the dirt road, and the 0.48 tarp has a standard deviation greater than 0.02 at all wavelengths longer than 500 nm. Figure 3.10 shows the reflectance spectra and standard deviations for the four reference surfaces; the 0.48 tarp, vegetation, and dirt road spectra are plotted with the same axes to allow a comparison. Mean derived surface reflectances for June 16 and June 17 are also shown to illustrate the variation of the observed surface reflectance in different illumination conditions. For the reference tarps the mean reflectance values for June 16 and 17 are within the standard deviation of cloud-free observations from June 8. The natural surfaces, the dirt road and vegetation show more variation between days. The dirt road surface has significantly lower reflectance on the overcast day, June 16. It is unclear whether this decrease is due to the different illumination or whether the road surface had been changed, possibly becoming damp. The NIS retrieved surface reflectance spectra are compared to the mean of several ground surface reflectance measurements made on the same day as the airborne observations to account for differences in illumination over the three days of observations.

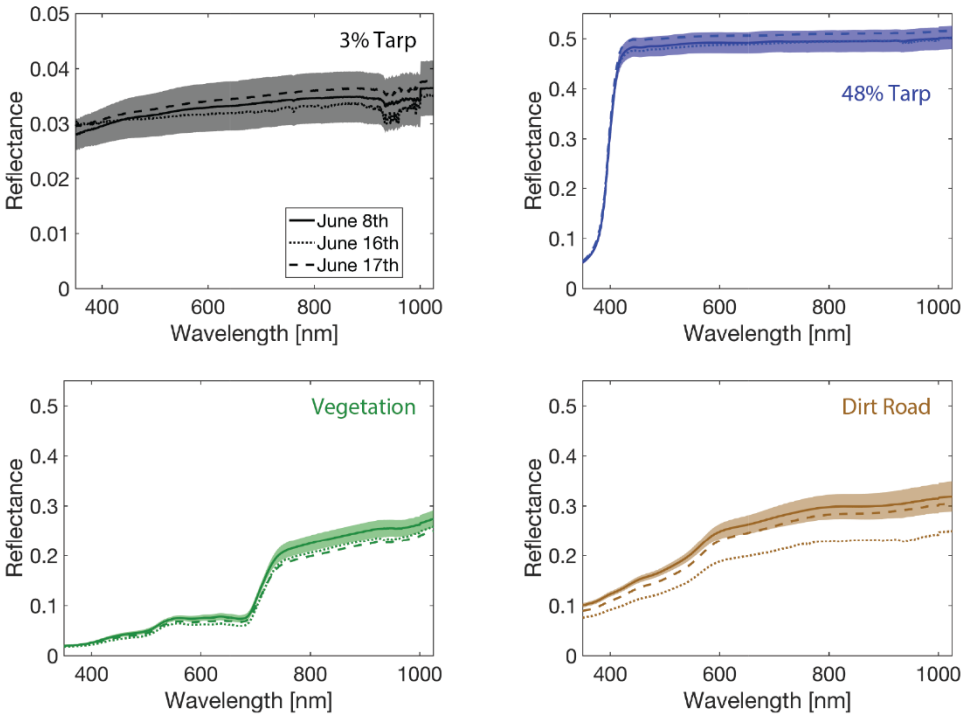

Figure 3.10: ASD derived surface reflectances for the 0.03 and 0.48 reflectance reference tarps, a vegetated surface and the dirt road.
The lines show the mean reflectance spectra measured for each of the three collection days. The shaded region shows the standard deviation, ±1σ, of the measurements made on June 8 with cloud-free conditions.

Airborne flight data were collected over several days with varied atmospheric conditions. Figure 3.5 shows a photograph taken during data collection on each day. On the morning of June 8 observations were made under nearly cloud-free conditions with the aircraft flying at 1000 m above ground level (AGL). Clouds were present near the horizon over the mountains far to the west of the ground site (Figure 3.5 left panel). On the morning of June 16 conditions were overcast, with scattered low cumulus clouds below a stratus cloud layer. On this day the aircraft operated at an altitude of 260 m AGL to remain below the cloud base. The flight on the afternoon of June 17 captured more complex sky conditions with a mixed of scattered cumulus and high altitude cirrus. The aircraft flew at 1000 m AGL. The inhomogeneous and optically thick cloud conditions on

June 16 present an extreme challenge to atmospheric correction. Our ideal target cloud conditions of optically thin, relatively homogeneous cirrus did not occur during the test flight period. Four or five flights lines were collected during the flight opportunity on each day. These flight lines were collected along latitudinal and meridional tracks centered on the crossroads shown in Figure 3.9. The flight directions were rotated with each line collected so that the meridional lines were collected in both north to south, and south to north directions while the latitudinal lines were collected both east to west, and west to east. Results from a single flight line on each day are presented in Figure 3.11.

For the three flight days we performed a standard atmospheric correction, shown in blue, and an enhanced correction, without the adjacency correction, shown in orange, and an enhanced correction using the adjacency correction shown in red. These colors have been kept consistent across the all the tables and figures. Both the standard and the two enhanced corrections were performed using the MODTRAN standard mid-latitude summer atmospheric profile as the input to the radiative transfer model. Only the aircraft altitude, solar zenith angle, day of the year, and a single scene value of column water vapor were modified in the radiative transfer model. Column water vapor was scaled to minimize the residual absorption. No attempt was made to retrieve aerosol extinction. The absence of a nadir InGaAs spectrometer limited the enhanced retrievals to wavelengths shorter than 1000 nm.

To quantify the comparison of the standard and enhanced atmospheric correction methods we calculated the root-mean-square (RMS) error of result of both retrieval methods compared to the ASD measurements, shown in Table 3.1. The error values have not been normalized so the values are the absolute error, in reflectance units.

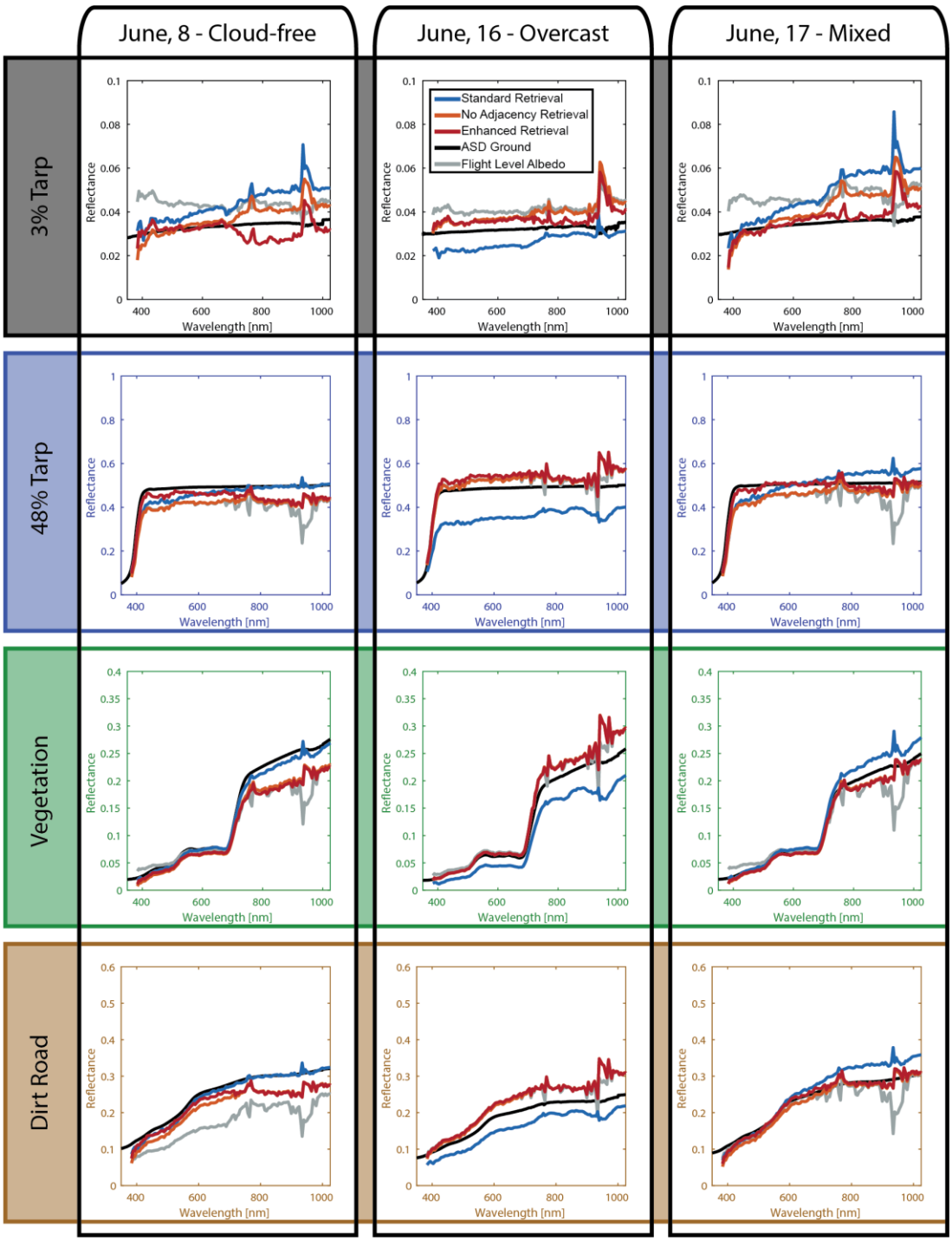

Figure 3.11: Atmospheric correction results; from top to bottom, for the 0.03 reflectance tarp, 0.48 reflectance tarp, vegetation, and dirt road.
Each column lists results from a single flight day; from left to right, June 8, June 16, and June 17. Black lines are ASD-derived surface reflectance. Red spectra are the enhanced retrievals with adjacency correction, orange are the enhanced retrievals without adjacency correction, and blue spectra are the standard retrievals. The light gray spectra are the flight-level albedos, $\boldsymbol{\pi L / F_{F\downarrow}}$. While this is not the same quantity as surface reflectance it is shown for reference. Spectra are the mean value averages over all pixels of that surface type.

Table 3.1: RMS errors between the NIS retrieved surface reflectances and the ASD derived reflectance values.
Errors are presented for both the standard and enhanced correction methods. Values are absolute error values in reflectance units.

	June 8, 2015 – Cloud-Free			June 16, 2015 - Overcast			June 17, 2015 - Mixed		
	Standard	Enhanced, No Adjacency	Enhanced, with Adjacency	Standard	Enhanced, No Adjacency	Enhanced, with Adjacency	Standard	Enhanced, No Adjacency	Enhanced, with Adjacency
0.03 Tarp	0.0133	0.0072	0.0058	0.0062	0.0106	0.0066	0.0193	0.0121	0.0067
0.48 Tarp	0.0321	0.0751	0.0548	0.130	0.0556	0.0623	0.0492	0.0496	0.0269
Vegetation	0.0088	0.0359	0.0404	0.0410	0.0297	0.0278	0.0201	0.0121	0.0164
Dirt Road	0.0095	0.0598	0.0390	0.0370	0.0483	0.0477	0.0364	0.0155	0.0147

3.7. Discussion

3.7.1. Spectral Sampling Challenges with Multiple Instruments

Below cloud the enhanced atmospheric correction's surface reflectance values are generally closer in magnitude to the field spectra but contain more channel-to-channel variation, than the standard correction values. This variation can be attributed to the difference between the NIS and SSIM spectral sampling and resolution. Combining measurements made by instruments with unique slit functions required spectral resampling. In this work the SSIM measurements were resampled to the NIS resolution and response function. A result of the mismatch in spectral resolution and sampling between the two instruments is evident in the resulting surface reflectance spectra at the 762 nm oxygen A-band where there is a very sharp absorption feature in the original radiance and irradiance spectra (Figure 3.12, left panel). Combining measurements from the two instruments produces a residual overcorrection feature, shaped like an M, in retrieved surface reflectance spectra at the location of the oxygen absorption band (Figure 3.12, center and right panels). Figure 3.12 demonstrates this problem by comparing modeled downwelling irradiance spectra that have been resampled to the NIS and SSIM slit functions. The 9 nm spectral resolution of the SSIM versus 5 nm for the NIS results in a broadening of the absorption band. The broadened absorption feature then produces an overcorrection at the edges of the band with less of an

overcorrection at the band center resulting in the M shape. This type of artifact is common when comparing spectrometers having different spectral and sampling resolutions.

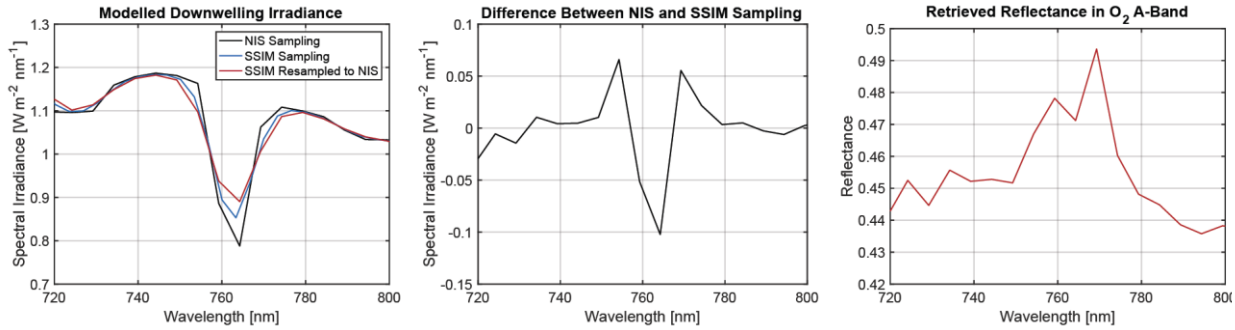

Figure 3.12: SSIM and NIS Sampling of the oxygen A-band.
Left panel shows modeled downwelling irradiance using the NIS spectral response function, in black, the SSIM spectral response function, in blue, and the result of resampling the SSIM irradiance with the NIS response function. Center panel is the difference between the NIS-sampled irradiance and the SSIM irradiance that has been resampled to the NIS response function. The characteristic M shape is visible. The right panel shows the enhanced, with adjacency correction retrieval of surface reflectance for this same wavelength region for comparison.

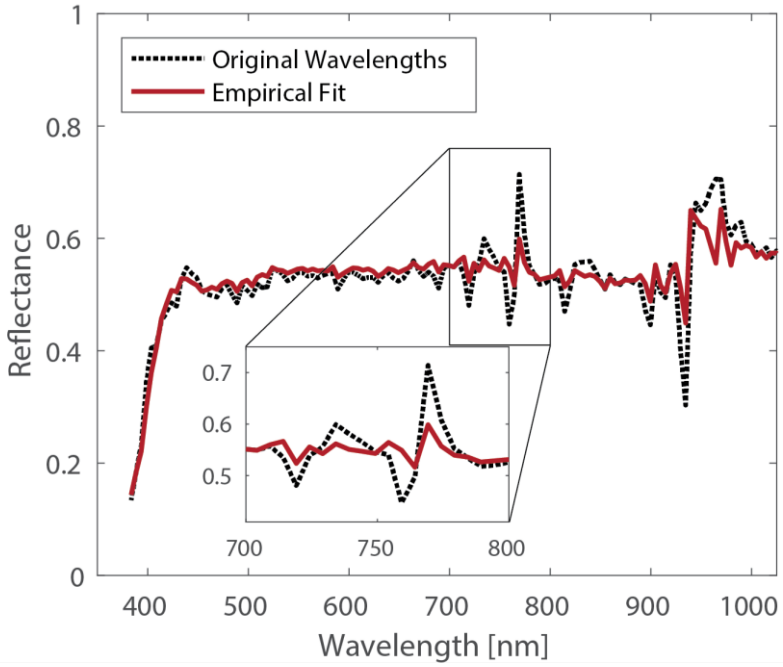

Figure 3.13: Two surface reflectance spectra retrieved using the enhanced atmospheric correction method.
The dashed black line is the result of using the original wavelength calibrations for the two instruments. The solid red line is the result of empirically shifting the center wavelengths to minimize the magnitude of the feature at 762 nm. The inset expands the oxygen A-band region; demonstrating the reduction in spectral mischaracterization error achieved using the empirically derived wavelength offsets.

The standard retrieval shows a smaller error at the oxygen A-band and the 940 nm water vapor band from imperfect characterization of the single spectrometer; adding an additional instrument response function magnifies this error. Without perfect knowledge of wavelength calibration and slit function FWHM, convolving measurements from the two instruments will produce errors that are especially evident around sharp, strong absorption features. Since this error is known to arise from wavelength shifts in the sensor spectral characterization we use an empirical fit to minimize the error by shifting the instrument center wavelengths by 0.01 nm increments over a range of ±3 nm (Qu et al., 2003). An offset is selected by choosing the value that produces the smallest magnitude feature in surface reflectance result at the oxygen A-band (Figure 3.13, solid red line). For these flights, the empirical best-fit spectral offsets were 1.28 nm for the NIS and -2.50 nm for the SSIM. These offsets were used to retrieve the surface reflectances shown in Figure 3.11. The ideal solution to this spectral mismatch problem is to employ the same spectrometer to make both imagery and irradiance measurements. This approach is taken by the Specim FODIS instrument (Homolova et al., 2009).

Water vapor absorption centered on 940 nm is responsible for the other large error spike in both the enhanced and standard retrieval spectra. Some of this error can be traced to the spectral resampling issues discussed above. However, the errors in the water vapor absorption bands are also attributed in part to the method used to determine column water vapor. A single column water vapor value was empirically determined for each of the three flight days. It has been previously shown that column water vapor can vary significantly over a scene (B.-C. Gao et al., 1993; Qu et al., 2003). This source of error in the water vapor bands could be minimized by implementing a pixel-by-pixel retrieval. Many existing atmospheric correction algorithms already incorporate such a correction (Richter & Schläpfer, 2015).

3.7.2. Solar Geometry Correction for Enhanced Retrievals

Examining the cloud-free results, in the leftmost column of Figure 3.11, we see that there are significant differences between the enhanced and standard retrievals. A large improvement was not expected in cloud-free conditions; the model atmosphere closely approximates the cloud-free conditions for that day. However, both of the enhanced retrievals less accurately match the ground surface reflectance measurements, with three of the four surface types show larger RMS errors. The enhanced methods produced larger error for the 0.48 reflectance tarp, vegetation, and road surfaces while producing smaller errors for the 0.03 reference tarps (Table 3.1). A portion of the error is attributable to differences between the observed and modeled downwelling irradiances (Figure 3.4, bottom left panel) possibly suggesting that atmospheric conditions did not match the modeled cloud-free atmosphere. However, the majority of the error can be attributed to the solar geometry of the scene, and the assumptions made for the enhanced retrieval methods. The direct solar portion of irradiance has a slant path that is longer than the vertical ground to aircraft path (Figure 3.8). This path can be corrected by introducing the cosine of the solar zenith angle, or μ (highlighted in red), into the directly transmitted term of Eq. **(3.9)**, producing:

$$\rho_\lambda = \left[\langle L\rangle_\lambda - \langle L_0\rangle_\lambda - \frac{F_{F\downarrow}\langle (T+t)t\rangle_\lambda}{\pi}\frac{\bar{\rho}_\lambda}{1-\langle\sigma_L\rangle_\lambda\bar{\rho}_\lambda}\right]\frac{\pi(1-\langle\sigma_L\rangle_\lambda\bar{\rho}_\lambda)}{\mu F_{F\downarrow}\langle (T+t)T\rangle_\lambda} \qquad \textbf{(3.10)}$$

Adding this term accounts for the decreased transmittance due to the slant path when the sun is off-zenith. However, this correction is only possible if the direct and diffuse components the downwelling irradiance are known. Figure 3.14 shows the surface reflectance retrievals including the solar zenith angle correction, assuming the MODTRAN modeled direct and diffuse irradiance proportions. The result is that the retrieved surface reflectance spectra are very similar to the standard retrievals. The RMS errors of the vegetated surface retrievals are decreased to 0.0189 and 0.0129, respectively, for the enhanced methods with and without adjacency correction. These

values are still larger than the standard retrieval value of 0.0088 but less than half of the uncorrected RMS error values.

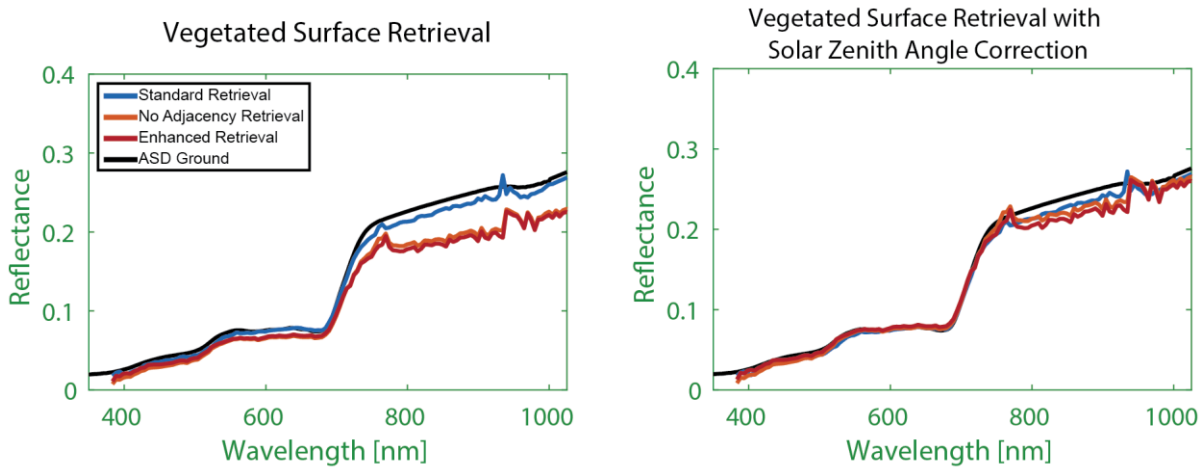

Figure 3.14: June 8 vegetated surface retrievals in cloud-free conditions.
The left panel reproduces the plot from Figure 3.11. In the right panel the two enhanced retrievals, shown in red and orange, have been modified to account for the slant path of the direct solar irradiance.

Assuming the modeled direct and diffuse irradiance partitioning improves results for a cloud-free scenario. However, this assumption would be poorer in the presence of clouds because a cloud layer would increase the amount of diffuse downwelling irradiance relative to the direct amount. Since we primarily wanted to demonstrate the below-cloud retrievals all of the result shown in Figure 3.11 were retrieved without the solar zenith angle correction in the enhanced retrievals. An ideal solution to this problem would be an irradiance instrument that is capable of measuring both total and diffuse irradiance allowing for the correction factor to be calculated. This measurement is technically difficult to make on an airborne platform and no such instrument has yet been deployed.

3.7.3. Impacts of Upwelling Irradiance based Adjacency Correction

In all but three cases the enhanced retrieval including the adjacency correction more accurately retrieved the surface reflectance spectra, as quantified by RMS error, than the enhanced

retrieval without the adjacency correction. This can be seen most clearly in the retrievals for June 8 and 17 in Figure 3.11. On these days the adjacency effects, while small in a cloud-free atmosphere, are responsible for the significant deviation of the standard retrieval from the ground truth observations. The effect is most noticeable for the two reference tarps and less pronounced for the vegetation or road surface because the tarp surfaces have reflectance spectra that contrast significantly with the adjacency reflectance of the scene. The reflectance spectra retrieved with the standard method, and enhanced method without the adjacency correction, are too high for the 0.03 tarp, especially at wavelengths longer than 700 nm, and too low for the 0.48 tarp, especially at wavelengths shorter than 700 nm. The direction of these errors is consistent with the adjacency effect because the scene's adjacency reflectance is dominated by the vegetation reflectance spectrum, which is brighter than the 0.03 tarp but darker than the 0.48 tarp. The sharp change in vegetation reflectance due to the near-infrared edge at 700 nm is consistent with the magnitude of the difference between the two enhanced retrieval results which changes at this same wavelength. The road and vegetation spectra more closely match the scene adjacency reflectance spectrum, $\bar{\rho}$, so the difference between deriving adjacency reflectance from the upwelling irradiance observation and assuming that $\bar{\rho} = \rho$ is minimal.

3.7.4. Below-Cloud Retrieval Performance

Results from the overcast day, June 16, demonstrate the improvements using the enhanced correction method (Figure 3.11, center column). For all the surfaces the standard atmospheric correction reflectances are significantly lower than the ASD ground measurements, by as much as 0.2 at some wavelengths. The low bias results from the standard retrieval not accounting for the decrease in atmospheric transmittance due to the overlying cloud. Therefore, the surface reflectance must be lower for the modeled radiance to match the NIS observations. For the reference tarps, and vegetation surfaces the enhanced method with adjacency correction produces

surface reflectance values much closer to the ASD measurements than the standard results. While both enhanced retrievals produce a larger error for the dirt road target than the standard method, though the enhanced retrievals of reflectance are too high and the standard result is too low. The other three surface types show improvement, with RMS errors reduced by up to 57% from the standard method. The result is retrieved surface reflectance values with errors that approach the radiometric accuracy of the NIS. This regime, when the aircraft is below clouds, is where the enhanced retrievals produce the greatest improvements over the standard method.

Observations from June 17 tell a story that is not entirely captured by the results shown in the right column of Figure 3.11. These results show a significant improvement in the surface reflectance retrieval with the enhanced methods. However, the sky conditions overlaying these observations were mixed scattered cumulus below cirrus clouds. Throughout the collected flight lines various clouds, both cirrus and cumulus, drifted in front of the sun with occasional cloud-free periods. While the mean spectra and RMS error values shown compare favorably with the other results from the other days they do not capture the quickly changing cloud conditions. Over the period of 100 seconds, roughly the length of a flight line collection, the downwelling irradiance varied by more than ±20%, occasionally changing rapidly, by up to 80% over 10 seconds. In such rapidly change conditions the sampling rate of the SSIM, 1 Hz, may be insufficient. Additionally differences between scene illumination and the observed downwelling irradiance due to horizontal offset problem, discussed in section 3.5.2, from solar zenith angle could introduced very substantial errors in the retrieved surface reflectances.

3.8. Summary

Accurately retrieving surface properties from airborne hyperspectral imagery below clouds is a challenging task for atmospheric correction. The improvements achieved in this work

demonstrate that there is great potential for making accurate below cloud retrievals by assimilating simultaneous observations of spectral up- and down-welling irradiance. Retrieval accuracy was generally improved, with the RMS error in the retrieved surface reflectance reduced by up to 57% for the overcast flight. This improvement was made despite the difficult cloud conditions encountered on the overcast flight day, June 16. The cloud field on this day presented a very complex scene with an optically thick inhomogeneous cloud field including multiple cloud types, and quickly changing conditions. There are, however, limitations associated with making observations below clouds. The signal-to-noise ratio is necessarily reduced due to the lower transmission of the cloud compared to cloud-free atmosphere. There is also an increase in channel-to-channel variation in the retrieved reflectance due to imperfect spectral resampling arising from the differing resolution and sampling of the SSIM and NIS. Simpler cloud conditions, such as thin cirrus or more homogeneous scenes should be more straightforward to correct and produce more accurate surface reflectance retrievals. However, the ability to retrieve surface properties below clouds presents the opportunity to collect additional data, or make more frequent repeat observations at times when data collection was previously avoided.

Incorporating SSIM irradiance measurements into the atmospheric correction routine reduced RMS error by up to a factor of two, for below cloud observations. Below clouds, the enhanced correction produces more accurate surface reflectances than the standard method. In addition, during cloud-free conditions the accuracy of the enhanced method approaches that of the standard method. The additional channel-to-channel variation present in the surface reflectances spectra retrieved with the enhanced correction is a result of imperfect spectral calibration of the two instruments. Ideally the irradiance and imaging spectrometer measurements should be made with the same detector to minimize this spectral effect. These improvements are largest and most

consistent below cloud fields with little horizontal variation, while the variation in irradiance below broken cloud fields may exceed the temporal resolution of the current SSIM instrument. The SSIM observations result in a second benefit, upwelling irradiance measurements can be used to provide an estimate of the adjacency effect of the scene.

A major limitation of the enhanced retrievals in this study is the spectral sampling between instruments. This problem has been previously solved by using the same spectrometer and detector to observe irradiance and imagery; an approach used to some extent with other instruments such as Specim's FODIS (Homolova et al., 2009).

For the cloud-free scenes the enhanced retrieval methods produced less accurate retrievals than the standard method due primarily to the solar geometry. Properly correcting this effect, without assumptions of the above aircraft transmittances, would require aircraft measurements of the direct and diffuse downwelling irradiances. An airborne instrument capable of these measurements is technically challenging to build and no such instrument has been previously described. Ground-based measurements are often made by periodically moving sun-shades into the direct solar radiation path to enable to measurement of diffuse in addition to total irradiance (Harrison et al., 1994; Reynold et al., 2001). Implementing a moving sunshade on the exterior of an aircraft is a difficult engineering problem which complicates an airborne instrument implementation.

The enhanced retrievals that use the upwelling irradiance measurement to estimate the adjacency effect achieve smaller errors than ignoring the adjacency effect. More accurate surface reflectance retrievals were achieved using the adjacency correction in both cloud-free and overcast scenes. However, we did not examine the performance of this adjacency correction against many of the other techniques that are in use such as approximating the adjacency effect from the imagery

itself (Richter, 1998; Richter & Schläpfer, 2015). This work shows that an irradiance-based adjacency correction is better than no correction. Based on this result, further investigation is need to determine how this upwelling irradiance-based method compares to existing adjacency correction techniques.

Beyond the methods presented, there are many opportunities for improving below-cloud atmospheric correction method. This work demonstrated that airborne irradiance observations can contribute to more accurate atmospheric correction below cloud layers using a simple retrieval technique. However, further improvements could be made by incorporating more advanced techniques already employed in other atmospheric correction routines, alongside spectral irradiance observations. This includes techniques for retrieving atmospheric conditions, such as visibility and pixel-by-pixel column water vapor, from the imaging spectrometer data instead of using a default atmospheric profile.

3.9. Acknowledgements

We would like to recognize the contributions of the NEON aircraft operations group including the NEON airborne instrument operators and the pilots of Twin Otter International. This study would not have been possible without the data collected through their efforts.

The National Ecological Observatory Network is a project sponsored by the National Science Foundation and managed under cooperative agreement by Battelle. This material is based in part upon work supported by the National Science Foundation. Any opinions, findings, and conclusions or recommendations expressed in this material are those of the authors and do not necessarily reflect the views of the National Science Foundation. This material was supported by the National Science Foundation under Grants DBI-0752017 and sub-award NEON 1010-214-AOP.

The predecessor of the NEON leveling platform sub-system was originally developed for the NASA aircraft ER-2 under grant NNX10AV05G from NASA's Earth Science Technology Office, and later adapted for the NASA C-130 aircraft under NNX12AC11G (NASA's Radiation Science Program), which also funded the development of the spectrometer sub-system. The NASA ARISE experiment (Smith et al., 2017) included a sibling instrument to the NEON SSIM with both spectrometer and leveling platform systems.

Chapter 4

An Informed Non-Negative Matrix Factorization Method for Unmixing Atmospheric and Surface Signals in Hyperspectral Imagery

4.1. Abstract

Radiance observations made by hyperspectral imaging spectrometers in the solar portion of the electromagnetic spectrum are a mixture of signals from surface reflectance, atmospheric absorption, molecular scattering, and aerosol scattering. To retrieve physical properties from these observations the signals must be unmixed and attributed to their sources. Typically, model-based methods, such as atmospheric correction, are used in this step. In this paper, we develop a numerical unmixing algorithm, Informed Non-Negative Matrix Factorization (INMF), to attribute signals in place of model-based approaches. INMF is a cost function minimization routine that has been developed to incorporate knowledge of the physics of radiative transfer as constraints to the cost function. Implemented constraints include fixing the well-known spectral shape of molecular scattering and generating initial guesses of source spectra, also known as endmembers, from library reflectance spectra. The improved initial guesses and cost function constraints cause INMF to favor physically plausible solutions. INMF was applied to simple dark ocean images collected by the Hyperspectral Imager for the Coastal Ocean (HICO). To evaluate the results of the method, quantitative metrics of algorithm performance were defined and assessed, and the INMF solutions

were compared, in magnitude and spectral shape, with traditional model-based atmospheric correction radiance products. Using two of these simple images, we show that the method is sensitive to the choice of subset from within the HICO images. We tested the algorithm's sensitivity to initial conditions by perturbing the initial guess endmember spectra with ±30% systematic (wavelength-independent) offsets. The resulting solution endmembers converged towards the non-perturbed solution. The best case INMF solution of atmospheric scattering and water-leaving radiance differed from a standard model-based atmospheric correction (L2GEN or the Level-2 data product generator), by 3.4% and 24.9%, respectively. The INMF solutions were sensitive to scene type and number of endmembers.

4.2. Introduction

Hyperspectral imagers are a growing class of sensors that produce data widely applicable to many geophysical disciplines. Hyperspectral instruments are defined by their spectral resolution, requiring the "acquisition of images in many narrow contiguous spectral bands" (Goetz et al., 1985). Collecting a large number of contiguous spectral channels has many benefits over multispectral instruments that collect data in a limited number of discrete bands. For example, hyperspectral data can be used to derive a wider variety of science data products, including surface, vegetation and atmospheric properties (Goetz, 2009; Shaw & Burke, 2003). A core challenge of remote sensing is identifying the radiative processes such as atmospheric scattering, absorption, or surface reflectance, that contribute to the observed signal. *Spectral unmixing*, the process of separating hyperspectral imagery into component spectra (Keshava & Mustard, 2002), is one technique that was developed to address this attribution challenge by exploiting the additional spectral information provided by hyperspectral instruments. Attribution is especially important for climate monitoring (Wielicki et al., 2013).

Spectral unmixing can also extract sub-pixel information by deriving the fraction of various signal sources in a single pixel (Keshava, 2003). The subpixel information is the fraction of signal that is attributed to each source present in a pixel as opposed to classifying a pixel as a single type of source. Pixels are currently ascribed to a single source in products such as the National Land Cover Database (derived from Landsat Thematic Mapper imagery) (Homer et al., 2015), but more information can be extracted from subpixel analysis.

Many unmixing techniques have focused on surface signals, so they have been applied to surface reflectances (Bioucas-Dias et al., 2012; Keshava & Mustard, 2002), which are retrieved from the observed at-flight level radiances through *atmospheric correction* (B.-C. Gao et al., 2009). Atmospheric correction uses modeled atmospheric absorption and transmittance to calculate the surface reflectance (Goetz et al., 1997). This process depends on input conditions such as trace gas concentration and aerosol optical thickness. Uncertainty in these inputs limits the accuracy of the derived surface reflectance (B.-C. Gao et al., 2009). One commonly used commercial algorithm, Atmospheric/Topographic Correction for Airborne Imagery (ATCOR) (Richter & Schläpfer, 2015), retrieves surface reflectance with an accuracy of 10-20% depending on the target's surface reflectance, with darker surfaces having larger uncertainty (Richter & Schläpfer, 2002). A 10-20% accuracy is larger than the radiometric accuracy of modern instruments. For example, the Hyperspectral Imager for the Coastal Ocean (HICO) has a radiometric accuracy of 5% (Michael R. Corson et al., 2008). Moreover, these uncertainties are much larger than what the next generation of hyperspectral imagers are expected to achieve. Instruments on the NASA Climate Absolute Radiance and Refractivity Observatory (CLARREO) mission aims to have accuracies on the order of 0.3% (Wielicki et al., 2013). The accuracies of retrieved products like surface reflectance and instrument measurement accuracies are not the

same quantity, but the difference illustrates the need for more accurate retrieval methods to exploit improvements in instrumentation.

Our approach is to avoid model-based atmospheric correction by directly applying a numeric unmixing method to the radiance measurement. The observed *at-sensor radiance* is a combination of atmospheric signals, such as molecular, aerosol, and cloud scattering, and surface signals. From at-sensor radiance, the unmixing method attributes both surface and atmospheric signals while surface reflectance can only be used to attribute surface signals. This is expected to improve the accuracy of signal attribution.

A wide variety of numeric spectral unmixing techniques have been developed and applied to hyperspectral imagery including Independent Component Analysis (ICA) (Chiang et al., 2000; Comon, 1994), Principal Component Analysis (PCA) (Jolliffe, 2002; Roberts et al., 2014), N-FINDR (Winter, 1999), Pixel Purity Index (PPI) (Boardman et al., 1995), Non-negative Matrix Factorization (NMF) (D. D. Lee & Seung, 1999, 2001; Pauca et al., 2006), Vertex Component Analysis (VCA) (Nascimento & Dias, 2005), and many others (Keshava & Mustard, 2002). These unmixing techniques have several common limitations. Methods such as ICA and PCA use statistical requirements for separating components, such as minimizing mutual information, for ICA (Comon, 1994), and orthogonality, for PCA (Jolliffe, 2002). However, important physically distinct sources are not necessarily spatially, spectrally, or temporally independent or uncorrelated (Rabbette & Pilewskie, 2001; Roberts et al., 2011, 2014). Other approaches, like N-FINDR, PPI, and VCA, rely on the presence of a pure pixel of each source type within the image (Boardman et al., 1995; Nascimento & Dias, 2005; Winter, 1999), which is not possible when separating surface and atmosphere signals. Further, many unmixing methods, such as NMF, have algorithmic issues

including sensitivity to initial conditions and uncertainty in the number of endmembers (Berry et al., 2007) and others, such as PCA, can produce negative radiance values.

In this work, we develop a spectral unmixing method, *informed* non-negative matrix factorization (INMF) based on the NMF algorithm (D. D. Lee & Seung, 2001). NMF was chosen as the base method for the work because NMF produces a non-negative separation, and is algorithmically flexible (Jia & Qian, 2009; Pauca et al., 2006). We exploited this flexibility to add constraints to the algorithm that are based on the physics of radiative transfer. This paper details a first attempt at using NMF to separate atmospheric and surface contributions. We assess the ability of NMF to separate source signals with linear assumptions and physics based constraints and whether it is sufficient for this application. Specifically, we evaluate the performance and success of the algorithm by examining two HICO images for:

- sensitivity to initial conditions, including the magnitude of initial endmember spectra,
- sensitivity to spatial variation within a scene, and
- comparison to results from a model-based atmospheric correction including quantitative measures of absolute error and measures of spectral shape similarity.

We describe a conventional NMF approach in section 4.3, the INMF spectral unmixing method in section 4.4, the HICO atmospheric correction data in section 4.5, the INMF results in section 4.6, a discussion of algorithmic sensitivity and performance in section 4.7, and conclusions in section 4.8.

4.3. Non-Negative Matrix Factorization (NMF)

NMF is a multivariate decomposition technique that has been employed for data analysis applications such as text-mining and spectral analysis (Berry et al., 2007). NMF assumes a *linear mixture model*. In this model an observed spectrum, $\boldsymbol{Y}$, can be represented as a set of endmembers,

$\boldsymbol{X}$, that are scaled by weighting factors, $\boldsymbol{S}$, such that $\boldsymbol{Y} = \boldsymbol{SX} + \boldsymbol{N}$, where $\boldsymbol{N}$ is an additional measurement error vector. Linear mixing models have been used extensively in surface remote sensing based on the assumption that there is negligible scattering between different surface materials (Keshava & Mustard, 2002). We recognize that a linear mixing model is not ideal for atmospheric signals because the radiative processes within the atmosphere and at surface are affected by non-negligible multiple scattering events between the surface and overlying atmosphere and between different physical atmospheric features such as gas molecules and cloud droplets (Bioucas-Dias et al., 2012; Keshava & Mustard, 2002).

When applied to hyperspectral imagery, NMF factors the input data into *spectral endmembers*, which represent the spectral shape of each separated source, and *spatial abundances*, which describe the amount of each endmember in each image pixel. While hyperspectral imagery is three-dimensional, with one spectral and two spatial dimensions, it is simplest to perform the spectral unmixing on two-dimensional arrays. Therefore, the hyperspectral image is flattened into a two-dimensional array, $\boldsymbol{A}$, of *m* spectral bands and *n* number of pixels. Given a flattened hyperspectral image as input, an NMF routine produces an array of spectral endmembers, $\boldsymbol{W}$, having dimensions of *m-by-k* and an array of spatial abundance factors, $\boldsymbol{H}$, with dimensions *k-by-n*, (Figure 4.1). The number of endmembers, *k*, must be defined by the user; in general, *k* is chosen to be much less than both *m* and *n* so the dimensionality of the dataset is decreased. The reduced dimensionality results in a reconstruction such that the product of the endmembers and abundances, $\boldsymbol{WH}$, approximately represents the input data, $\boldsymbol{A}$: $\boldsymbol{A} \approx \boldsymbol{WH}$.

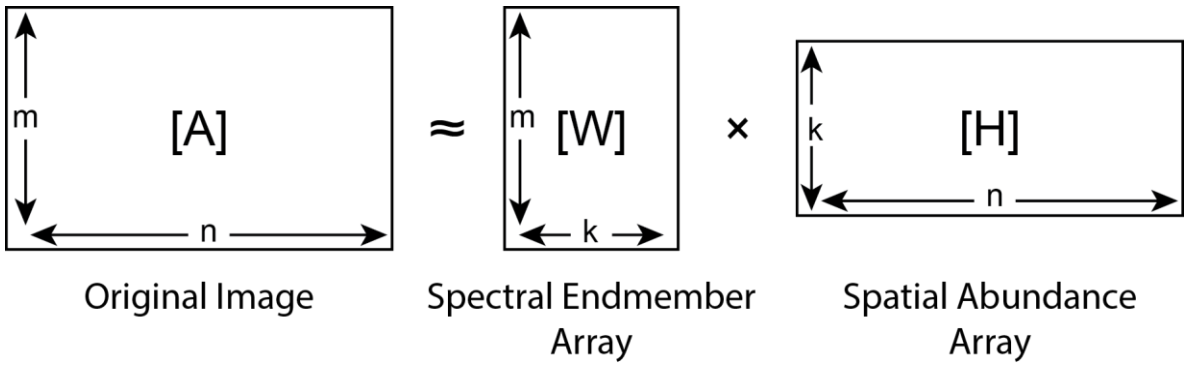

Figure 4.1: A graphical representation of the NMF decomposition.
The original image data, A, with m rows of wavelengths and n columns of pixels is factored into an array of k spectral endmembers, W, and k spatial abundances, H.

Given this framework an NMF algorithm solves for $\boldsymbol{W}$ and $\boldsymbol{H}$ by minimizing a cost function. The standard cost function, $D(\boldsymbol{W}, \boldsymbol{H})$, is the square of the Euclidean distance between the original image and the NMF approximation (D. D. Lee & Seung, 2001):

$$D(\boldsymbol{W}, \boldsymbol{H}) = \|\boldsymbol{A} - \boldsymbol{W}\boldsymbol{H}\|^2 \tag{4.1}$$

One drawback to this method is that the solution space defined by Eq. **(4.1)** may have many minima, with no guarantee that each represents a physically realistic solution. By simply minimizing the cost function the solution may converge to a minimum that is not a physically possible result. The presence of multiple minima within the solution space means that the INMF algorithm's result depends on the initial conditions, including initial endmember spectra, initial spatial abundances, and the number of endmembers (Pauca et al., 2006). While the algorithm is sensitive to the number of endmembers used for unmixing we do not examine approaches to automated selection of the number and type of endmembers. Instead we manually chose the number and type of endmembers based on the expected major contributing sources from a visual inspection of the image.

4.4. Informed NMF (INMF)

4.4.1. Constraints for the INMF Cost Function

The goal of introducing constraints is to address the inherently under constrained nature of the NMF problem and help the INMF solution to be physically realistic. To the basic cost function, Eq. **(4.1)**, we introduce constraints on spectral and spatial smoothness that produce a more physically realistic result. The spectral constraint assumes that real surface reflectances are spectrally smooth at the spectral resolution of hyperspectral instruments (Hunt, 1977). Spatial smoothness assumes that spatial patterns vary smoothly across a natural scene, such as a field or forest region. Piecewise smoothness is even more appropriate because it can accommodate abrupt boundaries, such as sharp land-water boundaries or man-made features that are likely to occur within real imagery (Jia & Qian, 2009).

Piecewise smoothness constraints were introduced by adding two terms to the cost function, one for spectral smoothness and another for spatial smoothness (Eq. **(4.2)**) (Jia & Qian, 2009). An adaptive potential function (Eq. **(4.3)**), $g(x_i, x_{\mathcal{N}_i})$, determines the smoothness of the endmember spectra and spatial abundances based on the difference between the value at a given pixel, x_i, or spectral channel, and the values in its spatial or spectral neighborhood ($\mathcal{N}$), $x_{\mathcal{N}_i}$. The size of the neighborhood can be set independently for each endmember and each spatial abundance. In this study, we set the *spectral* neighborhood for all of the endmembers, to five spectral channels on either side of the center wavelength. After substantial testing a smoothing window of five channels was chosen because five was the smallest window that removed sharp channel-to-channel variation from the INMF results.

$$D(\boldsymbol{W}, \boldsymbol{H}) = \|\boldsymbol{A} - \boldsymbol{W}\boldsymbol{H}\|^2 + \alpha\langle g(\boldsymbol{W} - \boldsymbol{W}_{\mathcal{N}})\rangle + \beta\langle g(\boldsymbol{H} - \boldsymbol{H}_{\mathcal{N}})\rangle \quad \textbf{(4.2)}$$

$$g\left(x_i, x_{\mathcal{N}_i}\right) = -e^{-\left(x_i - x_{\mathcal{N}_i}\right)^2/\gamma} + 1 \quad \textbf{(4.3)}$$

The *spatial* neighborhood was defined as the pixels within a taxicab distance (Krause, 1986) of two for surface endmembers, and five for the atmospheric endmember. Taxicab distance, d_t between two points A and B with coordinates (x_a, y_a) and (x_b, y_b), is defined as: $d_t = |x_a - x_b| + |y_a - y_b|$. This distance metric is used because it simplifies the implementation of a smoothing window on a gridded data set such as imagery. Setting these neighborhood values independently is intended to improve the unmixing of atmospheric and surface contributions which vary on different spatial scales. The spatial smoothing window values were set after qualitative evaluation of INMF results for simulated and HICO images. These values and the size of the spectral smoothing window are dependent on the spatial and spectral resolution of the instrument. The spatial windows are also likely to be scene dependent; for example, an urban scene would likely require a smaller smoothing window than the ocean scenes examined in this work.

Implementing the smoothness terms requires four scaling parameters. The constant, γ, determines how sharply the cost of the smoothness term decreases as the difference between the value, x_i, and the neighborhood values, $x_{\mathcal{N}_i}$, approaches zero. γ may have different values for the spectral, γ_W, and spatial, γ_H, domains. The other two parameters, α and β, scale the magnitude of the two smoothness parameters relative to the Euclidean norm term.

The brackets ($\langle\ \rangle$) in Eq. **(4.2)** represent a sum of matrix elements, and the smoothness functions employ their respective parameters, γ_W with $g(\boldsymbol{W} - \boldsymbol{W}_{\mathcal{N}})$ and γ_H with $g(\boldsymbol{H} - \boldsymbol{H}_{\mathcal{N}})$. The sensitivity of INMF results to the constraint parameters (α, β, γ_W, γ_H) is not examined in this paper; these parameters were selected as 0.5, 0.1, 0.01, and 0.5, respectively, following the values used in *Jia and Qian*, [2009].

Using Eq. **(4.2)** as the INMF cost function results in the following multiplicative update rules to minimize the algorithm. For more detailed discussion and proof of this method see *Jia and Qian*, [2009], §IIIB.

$$\boldsymbol{W} \leftarrow \boldsymbol{W} \odot \left(\boldsymbol{A}\boldsymbol{H}^T + \alpha(\boldsymbol{W} \odot h(\boldsymbol{W} - \boldsymbol{W}_{\mathcal{N}}) - g'(\boldsymbol{W} - \boldsymbol{W}_{\mathcal{N}})\right) \oslash (\boldsymbol{W}\boldsymbol{H}\boldsymbol{H}^T + \alpha \boldsymbol{W} \odot h(\boldsymbol{W} - \boldsymbol{W}_{\mathcal{N}})) \tag{4.4}$$

$$\boldsymbol{H} \leftarrow \boldsymbol{H} \odot \left(\boldsymbol{W}^T\boldsymbol{A} + \beta\left(\boldsymbol{H} \odot h(\boldsymbol{H} - \boldsymbol{H}_{\mathcal{N}}) - g'(\boldsymbol{H} - \boldsymbol{H}_{\mathcal{N}})\right)\right) \oslash (\boldsymbol{W}^T\boldsymbol{W}\boldsymbol{H} + \beta \boldsymbol{H} \odot h(\boldsymbol{H} - \boldsymbol{H}_{\mathcal{N}})) \tag{4.5}$$

In these update rules $\odot$ and $\oslash$ denote element-wise multiplication and division, respectively. The elements of $h(\boldsymbol{W} - \boldsymbol{W}_{\mathcal{N}})$, $g'(\boldsymbol{W} - \boldsymbol{W}_{\mathcal{N}})$, and the corresponding spatial functions $h(\boldsymbol{H} - \boldsymbol{H}_{\mathcal{N}})$, and $g'(\boldsymbol{H} - \boldsymbol{H}_{\mathcal{N}})$ are defined as:

$$h\left(w_i - w_{\mathcal{N}_i}\right) = \frac{2}{\gamma_W} \sum_{i' \in \mathcal{N}_i} e^{\frac{-\left(w_i - w_{i'}\right)^2}{\gamma_W}} \tag{4.6}$$

$$g'\left(w_i - w_{\mathcal{N}_i}\right) = \frac{2}{\gamma_W} \sum_{i' \in \mathcal{N}_i} (w_i - w_{i'}) e^{\frac{-\left(w_i - w_{i'}\right)^2}{\gamma_W}} \tag{4.7}$$

Another constraint, called Abundance-Sum-to-One (ASO), normalizes the abundance of each endmember into relative fractions of the total abundance in that pixel. (Heinz & Chang, 2001; Jia & Qian, 2009). This constraint does not require a modification of the cost function. Instead, the ASO normalization modifies $\boldsymbol{A}$ and $\boldsymbol{W}$ by inserting an additional row vector of ones scaled by a parameter, δ, that controls how close the sum of the spatial abundances must be to one:

$$\boldsymbol{A}_{\boldsymbol{A}} = \begin{bmatrix} \boldsymbol{A} \\ \delta \mathbf{1} \end{bmatrix} \qquad \boldsymbol{W}_{\boldsymbol{A}} = \begin{bmatrix} \boldsymbol{W} \\ \delta \mathbf{1} \end{bmatrix} \tag{4.8}$$

These new $\boldsymbol{A}_{\boldsymbol{A}}$ and $\boldsymbol{W}_{\boldsymbol{A}}$ arrays can simply be substituted for $\boldsymbol{A}$ and $\boldsymbol{W}$ in the update routine (Eqs. **(4.4)** and **(4.5)**). δ can be chosen to be any non-negative number. Increasing the value of δ produces a solution where the variability in the sum of abundances is smaller. Decreasing δ leads to larger variability. For all the results presented in this paper δ was set to 100. This value was chosen by testing the two images that were examined in this study. INMF was performed several times on the images with a range of δ. With a small value the sums of abundances in any pixel

could be larger or smaller than one. As δ increased the abundance value converge toward one. We set $\delta = 100$ because it was the smallest of the tested values that produced a scene averaged abundance sum within 1% of unity (between 0.99 and 1.01). As with many of the parameters used for INMF this value will be scene dependent; changes in the number of pixels and radiance level of the scene will affect the choice of δ.

The ASO method can have a drawback when INMF is applied to separating contributions from the atmosphere and surface. Consider a highly variable land surface below an unchanging atmosphere. In this scenario, while the absolute signal contribution from the atmosphere is constant over all the pixels, the relative strength of the surface and atmosphere contributions would vary significantly. Since the atmospheric spectral endmember is shared by all pixels, the NMF result with an ASO constraint would be unable to produce a correct representation of the atmosphere. This problem was resolved by simply modifying the ASO row vector to exclude the atmospheric endmembers from the sum constraint.

4.4.2. INMF Initial Separation Guess

The presence of an unknown number of minima in the solution space makes the NMF result highly dependent on the initial guess. Two random, initialization techniques are widely used with NMF. The first randomly generates initial endmember spectra (Berry et al., 2007; Qian et al., 2011). This approach has obvious limitations given NMF's strong dependence on initial conditions (Berry et al., 2007; Pauca et al., 2006). The second method selects spectra from randomly selected pixels to use as the initial guess (Jia & Qian, 2009; Wang et al., 2013). There is a clear drawback to this technique for separating atmospheric from surface contributions: these signals are mixed in every pixel so the spectrum from any pixel would be a mixed signal making it a poor selection for an endmember. Initializing INMF with a physically plausible separation will start the algorithm near the correct minimum, increasing the likelihood of convergence toward a physically plausible

result. We elected to manually choose the number and type of initialization spectra to ensure a physically realistic initial guess.

The spatial abundance array is initialized with equal abundance fractions. This scheme sets the spatial pixels associated with every endmember to the same abundance value. Derived at-sensor radiance spectra are used as the initial guess of the unmixed endmember spectra for the INMF algorithm. The at-sensor radiance spectra are derived using atmospheric and surface library spectra in the following approach. Surface reflectance spectra are from the Advanced Spaceborne Thermal Emission and Reflection Radiometer (ASTER) spectral library (Baldridge et al., 2009). Cloud reflectance spectra were sourced from NASA Reference Publication 1139 (Bowker et al., 1985). These cloud spectra are consistent with airborne measurements of cloud albedo from the Solar Spectral Flux Radiometer (Kindel et al., 2010). When multiple reflectance spectra were available for a single endmember, such as various types of vegetation and soil, the reflectance spectra were averaged to produce generic vegetation or soil spectra. The at-sensor radiances corresponding to each reflectance spectra (Figure 4.2) were calculated using transmittances derived with the MODTRAN radiative transfer model (Berk et al., 2006). MODTRAN calculated the transmittances using the solar and observing geometries of each HICO scene and the MODTRAN standard mid-latitude summer atmospheric profile.

4.4.3. Constraining the Spectral Shape of Molecular Scattering

In addition to the surface and cloud reflectance spectra, molecular scattering is a significant contributor to at-sensor radiance, especially at wavelengths shorter than 600 nm. Unlike many surface reflectance spectra, the spectral shape of molecular scattering is well known (Bodhaine et al., 1999). We constrain the spectral shape of the molecular scattering endmember at each iteration of the INMF algorithm so that only the magnitude of molecular scattering may vary. In each iteration of the algorithm the molecular scattering spectral shape is enforced after the endmember spectra are updated with Eq. **(4.4)**. The known spectral shape of molecular scattering is fit with a scaling factor to the updated endmember spectrum by minimizing the least-squares difference. This fitted spectrum is then inserted into the endmember array, ***W***, replacing the existing spectrum for the molecular scattering endmember.

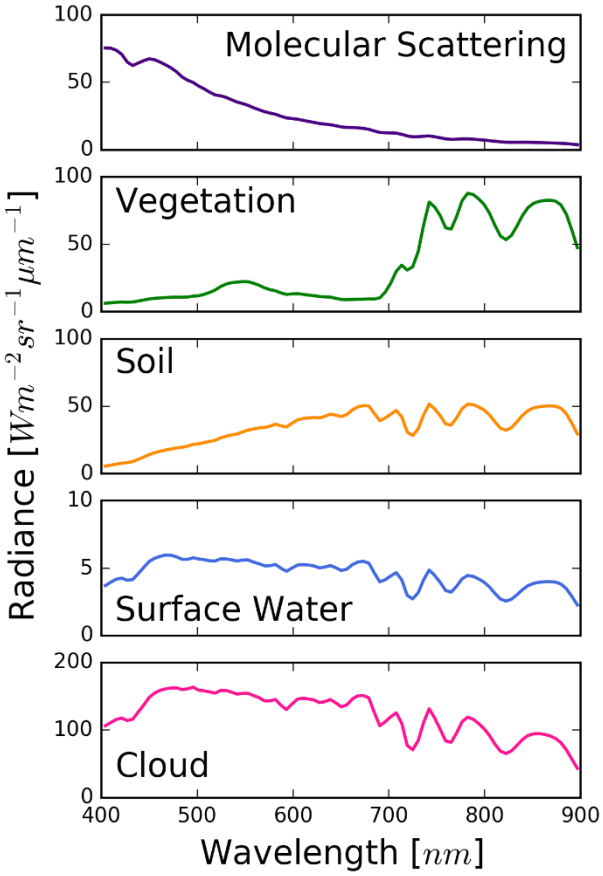

Figure 4.2: Calculated initial guesses of at-sensor radiance for a variety of surface types and atmospheric contributions.

4.4.4. Implementation of Algorithm Introducing a Settle-in Period

In examining the performance of the INMF algorithm, we found that the solutions could diverge from physically plausible endmember spectra. By examining the endmember spectra and abundances fractions after every iteration we found that the cause of this divergence was the *un-*

informed initialization of spatial abundance fractions. In the INMF algorithm the spectral endmembers and spatial abundances are used in turn to update the other, first with **(4.4)** and then with **(4.5)**, in each iteration. The algorithm produced divergent spectral solutions when the endmember spectra are updated using an unrealistic equal and spatially uniform abundances. Divergence did not occur for all the scenes examined. The initial endmember spectra and the choice of constraint parameters likely also have an effect, though this was not tested.

A settle-in period was introduced to avoid spectrally divergent results. During the settle-in period, the algorithm updates the spatial abundance array, $\boldsymbol{H}$, while the endmember spectra are held fixed. We propose that introducing the settle-in period reduced the appearance of divergent solutions because the abundances were not used to update the endmember spectra for several iterations. This meant that the abundances value had already been updated away from the equal abundance fraction initialization before they were used to update the endmember spectra. We qualitatively determined that a settle-in period of five iterations was sufficient to avoid the divergence problem for imagery analyzed in this work. While five iterations were sufficient for the scene processed for this study other INMF applications or even other HICO scenes may require different periods. After the settle-in period the algorithm begins iterating normally, updating both endmembers, $\boldsymbol{W}$, and abundances, $\boldsymbol{H}$.

4.4.5. INMF Algorithm Code

A summary of the INMF algorithm is shown below. The endmember spectra, $\boldsymbol{W}$, and abundance, $\boldsymbol{H}$, arrays are initialized. After initialization, the algorithm enters a settle-in period where the spatial abundances values are updated but the endmember spectra are not. After the five iterations of the settle-in period the iterative portion of the algorithm updates the spatial abundance, $\boldsymbol{H}$ (step 4a), and the endmember spectra, $\boldsymbol{W}$ (step 4b). Then the constrained molecular scattering spectrum is inserted into the array of endmember spectra, replacing the existing molecular

scattering spectrum (step 4c). Iteration continues until the change in the cost function value between subsequent iterations is less than a small value, ϵ. Appropriate values for ϵ depend on the dimensions of the scene, number of endmembers, and the average signal level of pixels in a scene. For the HICO scenes in this study values of ϵ were selected empirically to be between 2×10^{-10} and 5×10^{-10}.

INMF Algorithm

1. Initialize $\boldsymbol{W}$ with derived at-sensor radiances.
2. Initialize $\boldsymbol{H}$ with equal abundance fractions.
3. Settle-in period:
   a. Update abundances, $\boldsymbol{H}$, with Eq. **(4.5)**.
   b. After 5 iterations move to step 4.
4. Iterate:
   a. Update abundances, $\boldsymbol{H}$, with Eq. **(4.5)** .
   b. Then update endmember spectra, $\boldsymbol{W}$, with Eq. **(4.4)**.
   c. Calculate the scaled molecular scattering spectrum and insert into $\boldsymbol{W}$.
   d. Iterate until the cost function decrease in an iteration is less than ϵ.

4.5. Data

4.5.1. Hyperspectral Imager for the Coastal Ocean (HICO)

The Hyperspectral Imager for the Coastal Ocean (HICO) was designed and built by the U.S. Naval Research Laboratory and operated on the International Space Station from September 2009 through September 2014 (Lucke et al., 2011; Oregon State University, 2015). HICO's focus on coastal ocean regions provides challenging data for evaluating the INMF spectral unmixing method. Coastal ocean scenes are

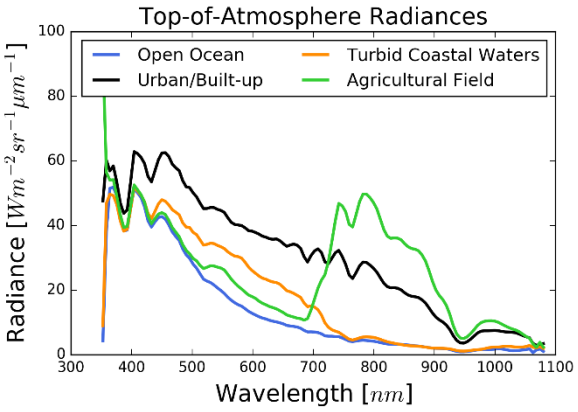

Figure 4.3: Example spectra of four different pixels collected by HICO.
These top-of-atmosphere radiance values include the contributions of molecular and aerosol scatter. All of HICO's 128 wavelength channels are shown.

complex. They include contributions from water, which includes suspended and dissolved matter, chlorophyll, and possibly the ocean bottom (M. R. Corson et al., 2010; Lucke et al., 2011). These surface contributions are in addition to atmospheric sources, including aerosol scattering, molecular scattering, and clouds, all with overlapping spectral features, that complicate the separation of observed signal into source spectra and abundances.

HICO had 128 wavelength channels between 352 nm and 1080 nm, with a spectral sampling of 5.7 nm and spectral Full-Width-Half-Maximum (FWHM) of 10 nm from 350-745 nm, and 20 nm from 746-1080 nm (Lucke et al., 2011). We use a subset of wavelength channels between 400 nm and 900 nm where HICO produced its best quality data (Lucke et al., 2011). HICO level 1B calibrated radiance data is available from the NASA Ocean Biology Distributed Active Archive Center (NASA Goddard Space Flight Center Ocean Ecology Laboratory Ocean Biology Processing Group, 2017). Figure 4.3 shows examples of spectra collected by HICO.

For this work we have applied the *vicarious calibration* produced by Ibrahim et al., (2018) to the HICO level 1B data. Vicarious calibration refers to on-orbit calibration that is performed using a target with assumed or measured reflectance properties. In this case the vicarious calibration made use of in-situ measurements of water leaving radiance collected by the Marine Optical Buoy (MOBY), operated by the National Oceanic and Atmospheric Administration (Brown et al., 2007; Clark et al., 1997). The result of this calibration is a gain value for each wavelength channel that can then be applied to HICO imagery.

4.5.2. Atmospheric Correction Products

To evaluate how well the INMF algorithm performs on the HICO images, we compare the INMF solution with the atmospheric and surface signals derived from a standard atmospheric correction model. Note that the atmospheric correction data are not ground truth measurements. They instead provide a comparison between the INMF results and another approach to separating

atmospheric and surface signals. To make these comparisons we processed the HICO scenes with a standard atmospheric correction routine, L2GEN (Level 2 Generator) (Ahmad et al., 2010; Gordon & Wang, 1994). L2GEN is packaged with NASA's SeaDAS software package, a satellite data processing, analysis and visualization tool (NASA Goddard Space Flight Center Ocean Biology Processing Group, 2017). While there are many atmospheric correction tools available we chose L2GEN because it is used extensively in the ocean color community.

We used L2GEN's atmospheric corrections to determine at-sensor radiances due to the atmosphere, from aerosol and molecular scattering; water leaving radiances; and the atmospheric transmittances. We compared the INMF molecular scattering endmember to the L2GEN derived at-sensor atmospheric radiance. We compared the INMF water endmember to the product of L2GEN derived water-leaving radiances and atmospheric transmittances. The accuracy of radiances derived with model-based atmospheric routines is affected by the same confounding factors that impact INMF results including the viewing geometry, surface reflectance and atmospheric transmittance of the scene. The stated goal of this atmospheric correction routine is retrieving water-leaving radiance with an uncertainty $\leq 5\%$ (Clark et al., 1997; Gordon & Wang, 1994; Mobley et al., 2016).

4.6. INMF Results

We analyzed two HICO images that include deep ocean regions (Figure 4.4). The first shows the Hawaiian Islands of Molokai and Lanai while the second is centered on the Florida Keys. The images were chosen for their areas of cloud-free and low aerosol optical thicknesses atmosphere that overlie dark ocean regions. This type of image is one of the simplest atmosphere and surface separation cases possible because the deep ocean portions of the image have only two

significant contributions to the at-sensor radiance: the signal from molecular scattering, and the signal from the water surface.

We processed several subsets of each image with the INMF algorithm. For the Hawaiian Islands image these were the full scene, a dark-ocean subset, and a cloud-free subset. The dark-ocean subset included only dark-ocean regions and was cloud-free. The cloud-free subset covers a wider area than the dark-ocean subset and includes parts of the island. For the Florida Keys image, the selections were the full image and a dark-ocean subset.

The Hawaiian Island full image was analyzed with five endmembers: water, soil, vegetation, cloud, and atmospheric scattering. Figure 4.5 and Figure 4.6 show the resulting INMF abundance maps, and endmember spectra respectively. The cloud-free subset of the Hawaiian Islands was processed with four endmembers, water, soil, vegetation, and atmospheric scattering. The dark-ocean subset

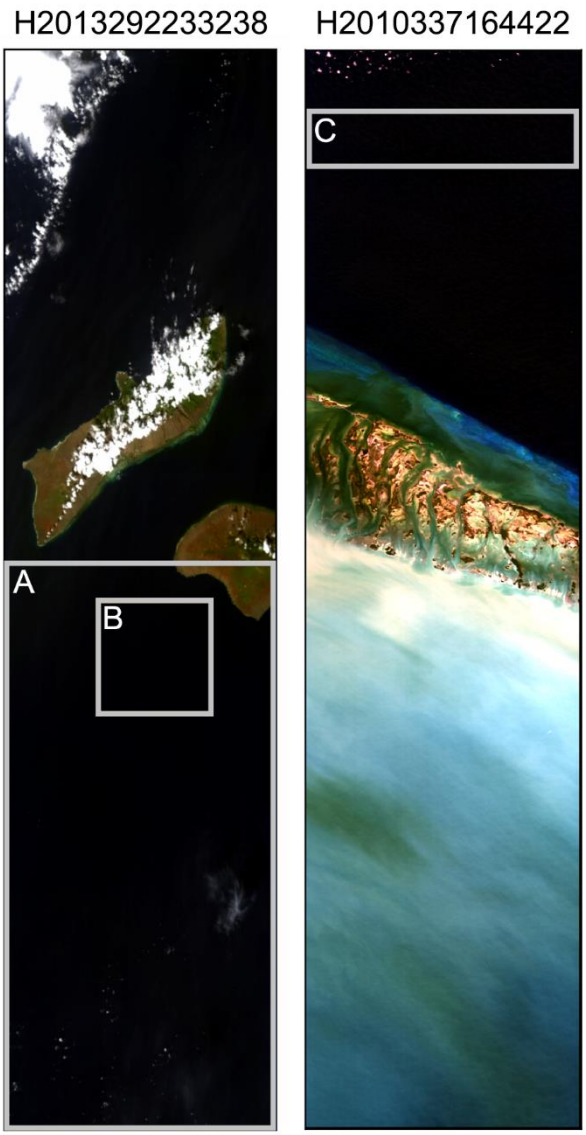

Figure 4.4: True color images of the HICO images examined in this paper.
The left image shows the Hawaiian Islands of Molokai and Lanai, and surrounding ocean, the right shows the Florida Keys and surrounding ocean. The boxes show the three scene subsets that were processed with INMF in addition to the full scene. On the Hawaiian Islands image, box A is the Cloud-free subset and box B is the dark-ocean subset. On the Florida Keys scene box C is the dark-ocean subset. Above each image is the HICO ID which corresponds to the time and date of the imagery in the format: YYYYDDDHHMMSS. The three number long day identifier (DDD) is the day of the year.

was processed twice, once with only two endmembers (water and atmospheric scattering), and a second time with three endmembers (water, cloud and atmospheric scattering).

For the Florida Keys image the subsets were the full scene, and the dark-ocean subset which was processed with two different sets of endmembers. The full scene was analyzed with four endmembers: water, soil, vegetation, and atmospheric scattering. Figure 4.7 and Figure 4.8 show the resulting INMF abundance maps, and endmember spectra respectively. The dark-ocean subset was processed twice, once with only two endmembers (water and atmospheric scattering), and a second time with water, vegetation and atmospheric scattering endmembers.

Abundance maps and endmember spectra are not shown for the selected subsets of Figure 4.5 and Figure 4.6 but quantitative results are discussed. The significance of the choices for varying the number of endmembers and the impacts on the INMF solutions is presented in the following section.

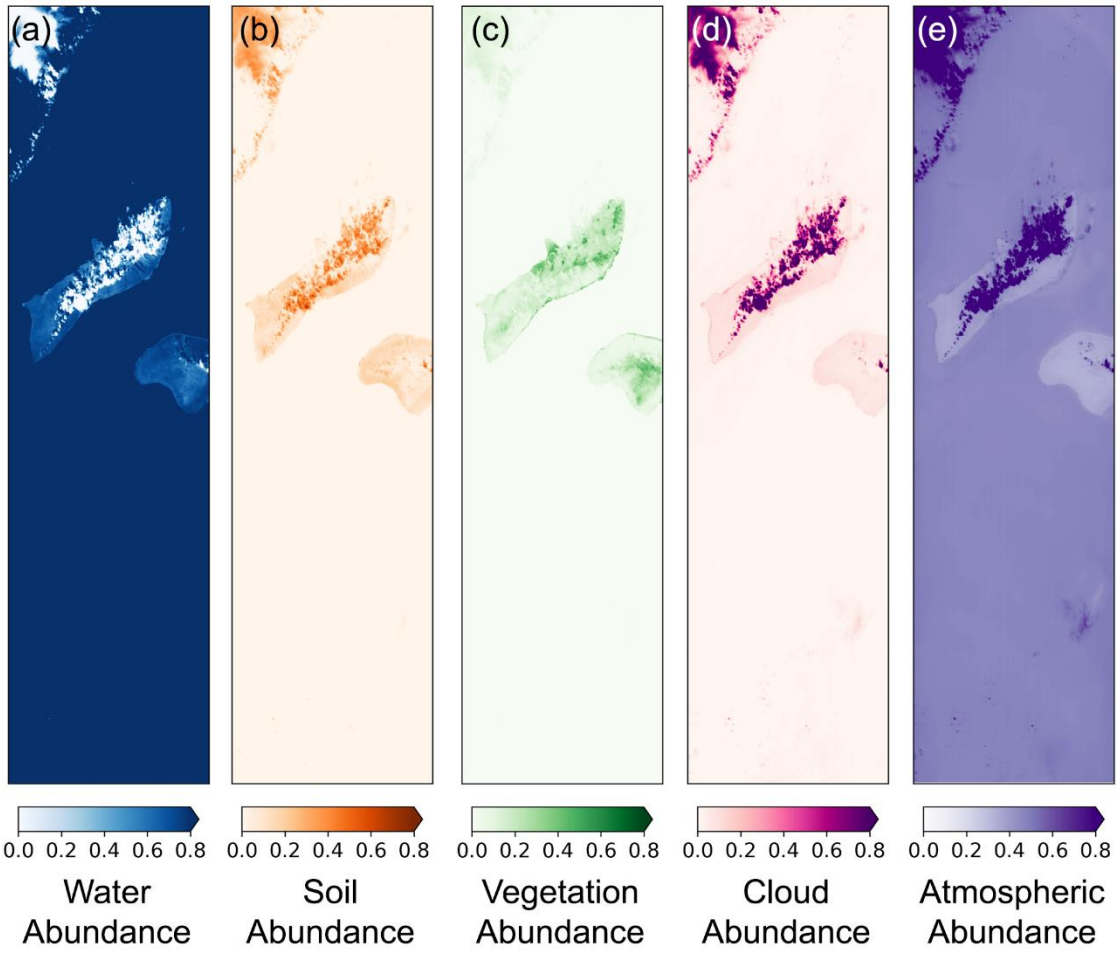

Figure 4.5: The INMF solution abundances for the full image of the Hawaiian Islands.
The maps show the abundance fraction of each endmember. On each map the more intense colors indicate higher abundance values.

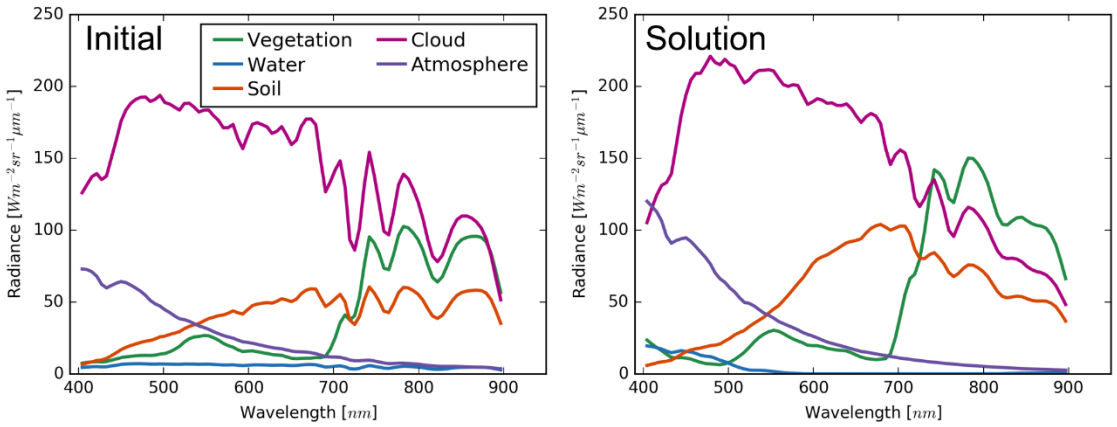

Figure 4.6: Endmember spectra for the Hawaiian Islands image.
The spectra correspond to the same colored map of abundance values from Figure 4.5. The spectra in the left panel were used to initialize the INMF algorithm. The right panels shows the corresponding solution spectra.

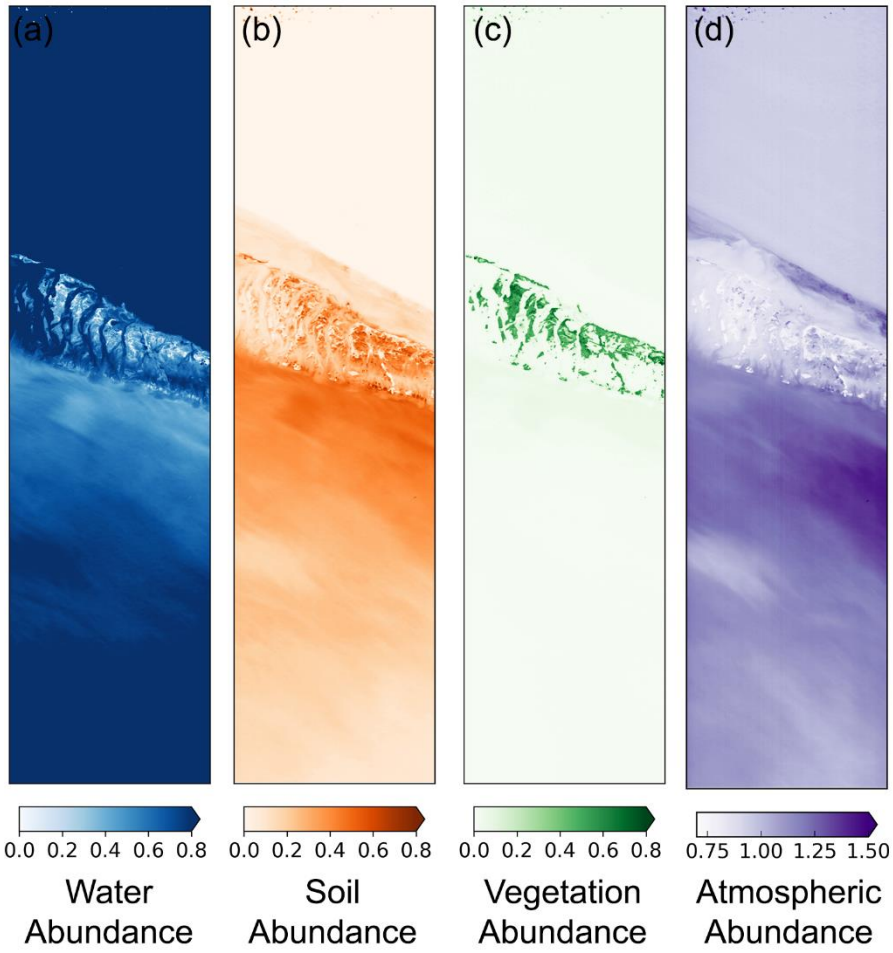

Figure 4.7: INMF solution abundances as in Figure 4.5 but for the full image of the Florida Keys.

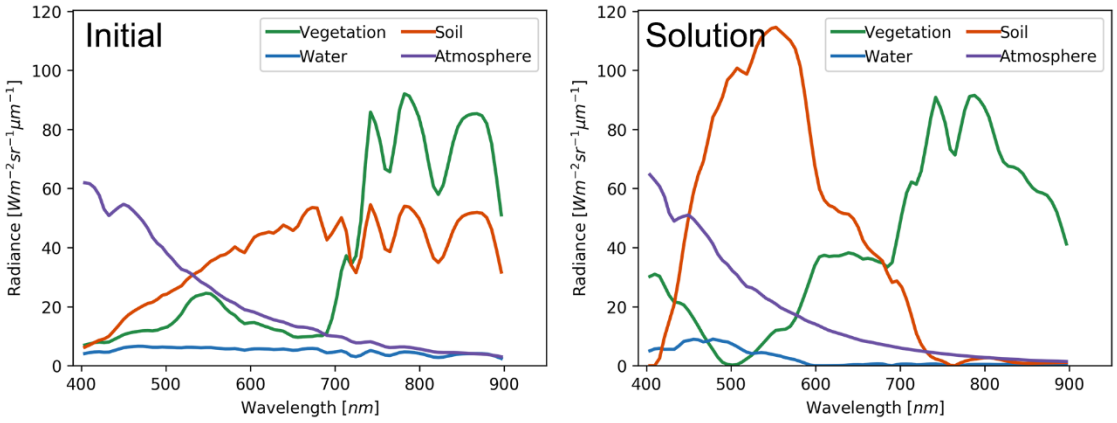

Figure 4.8: Endmember spectra as in Figure 4.6 but for the full image of the Florida Keys.

4.7. Evaluation of Results

The INMF results presented in Figure 4.5-Figure 4.8 are for just two images, but we can qualitatively examine the strengths and weakness of INMF through these two example cases.

In the Hawaiian Islands solution (Figure 4.5 and Figure 4.6), we see that the algorithm correctly identifies regions of cloud and vegetation and these endmember spectra are similar to their initial spectra. However, the cloudy regions of the image also have significant abundance contributions from two other endmembers, atmospheric scattering and soil. This is indicative of multiple endmembers representing a single physical source. This confusion is likely a result of the high signal level of clouds. The cost function is reduced more by reproducing the bright cloudy pixel spectra than by correctly representing the darker soil. The soil endmember appears to have been used because it lacked distinctive spectral features. In contrast, there is a physical basis for an enhancement in atmospheric scattering over clouds. Cloud scattering within the cloud increases atmospheric path length and therefore enhances the signal of atmospheric scattering.

The water endmember does have high abundances over the ocean but it also has significant abundances over the islands. This is a consequence of the low reflectance of surface water. Since the signal is small it can appear with significant abundances and not account for significant radiance from a land surface pixel. As a result, it often appears in dark non-water regions. For example, the water endmember has high abundances in shadowed areas. This is result consistently appears in INMF solutions that include the surface water endmember.

The Florida Keys image is simpler in that it has fewer endmembers and is mostly cloud-free. However, the INMF solution (Figure 4.7 and Figure 4.8) still suffers from some same problems as the Hawaiian Islands image. The water endmember has significant abundance over land, though this is less visible since the Keys have fewer land surfaces and less well-defined

coastlines. There is also a similar problem with the soil spectrum which does not resemble the initial guess. The solution spectrum peaks near 550 nm, in a spectral region where most other endmembers are low. This may result from the algorithmic need for an endmember with higher signal level between 500 nm and 600 nm where the other endmembers are low. An impact of this is that the soil does not appear to represent a pure physical source but rather a part of a source, or several sources, when considered in combination with either the vegetation or atmospheric scattering endmembers. This interpretation is supported by region below the Keys in the image where atmospheric scattering and soil abundances appear correlated. An additional endmember might improve the separation of pure physical sources by alleviating the need for a mixing between the endmembers.

This discussion highlighted some of the limitations of the INMF algorithm when applied to these two complex scenes. Complex scenes, such as these examples, are cases where both atmospheric correction models and numerical approaches struggle.

4.7.1. Comparison to Atmospheric Correction

The focus of this paper is the validation of the INMF solutions against atmospheric correction approaches for simple cases where only two contributions are expected. Figure 4.9 shows the comparisons between the INMF results and the L2GEN atmospheric correction radiance spectra for the Hawaiian Islands image subsets. Figure 4.10 shows the same for the Florida Keys image subsets. The plotted spectra are from the dark-ocean regions (boxes B and C on Figure 4.4 for the Hawaiian Islands and Florida Keys respectively) of INMF solution for each subset so that the same region is compared.

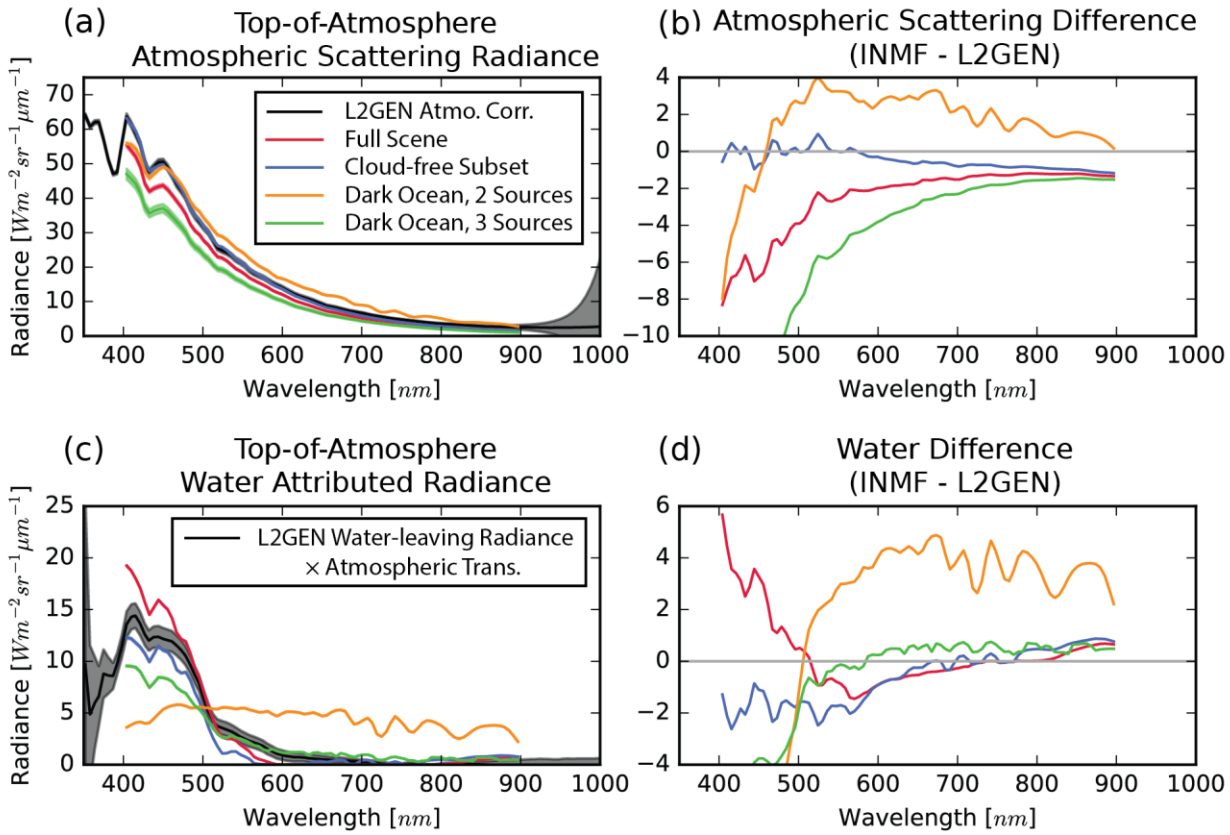

Figure 4.9: Comparison of the INMF solutions with the L2GEN atmospheric correction results for the Hawaiian Islands image.

The black lines are the atmospheric correction products. The colored lines are the INMF results for three different subsets of the scene: red, the full scene; blue, cloud-free subset; and two dark-ocean subsets, one in orange with two endmembers, and another in green with three endmembers. The subsets are outlined on Figure 4.4. The shaded regions on panels (a) and (c) are one standard deviation from the mean L2GEN solution for the dark-ocean subset. Shaded standard deviation regions are plotted for the INMF results but are so small that they are almost imperceptible. In panel (c) the black atmospheric correction line is the L2GEN water-leaving radiance propagate to the top-of-the atmosphere using the L2GEN atmospheric transmittance values. The rightmost panels, (b) and (d), are the difference between the L2GEN atmospheric correction result and the respective INMF mean values.

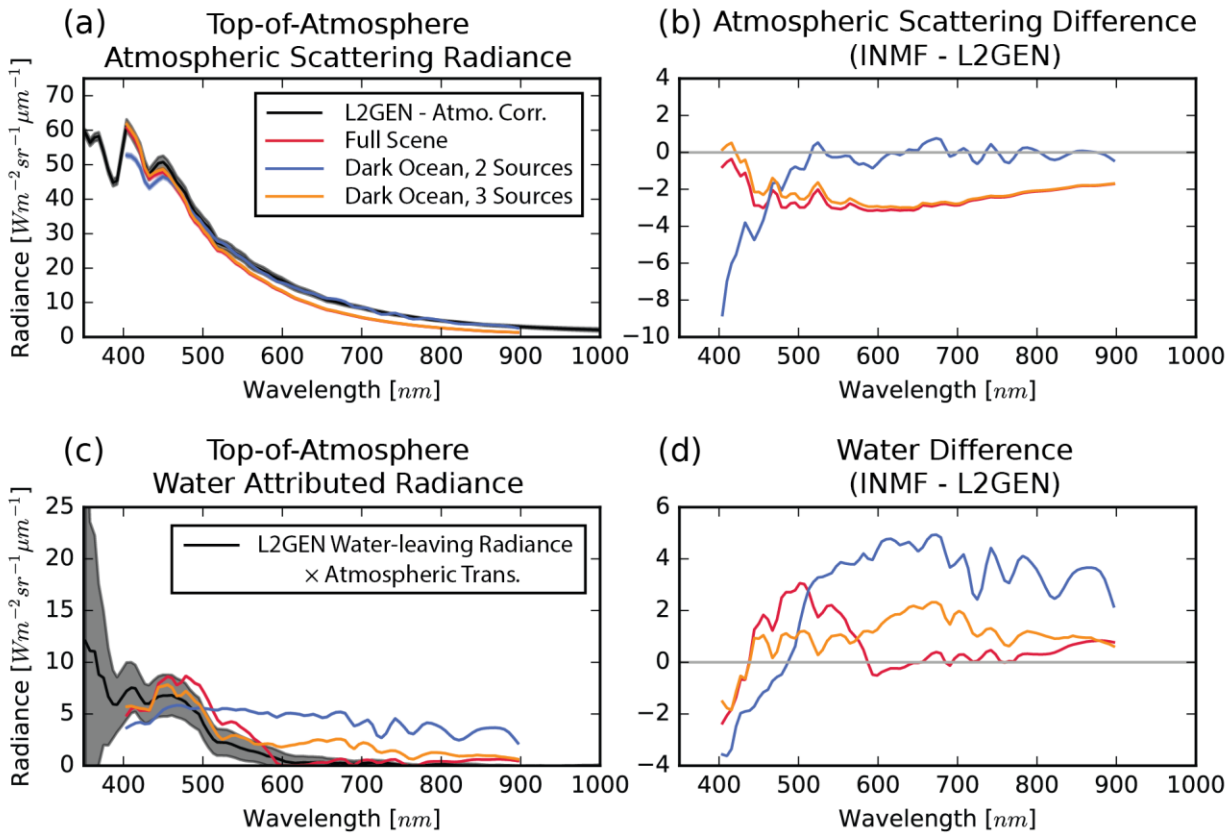

Figure 4.10: Comparison of the INMF solutions with the atmospheric correction results as in Figure 4.9 but for the full image of the Florida Keys.

We applied two metrics to quantitatively compare INMF solutions and L2GEN atmospheric correction results in Figure 4.9 and Figure 4.10. The first is simply the root-mean-squared (RMS) difference between the INMF and L2GEN radiance spectra. RMS difference measures the absolute difference between the two and gives a measure of the similarity of the two signals. An additional measure is necessary to evaluate the spectral shape similarity between the atmospheric correction and INMF results. For this we employed the Spectral Information Divergence (SID) (Chang, 2000). SID is calculated as the sum of the Kullback-Leibler divergences, $D(\boldsymbol{x}||\boldsymbol{y})$, calculated for each spectrum with respect to the other, so the $SID(\boldsymbol{x},\boldsymbol{y}) = D(\boldsymbol{x}||\boldsymbol{y}) + D(\boldsymbol{y}||\boldsymbol{x})$. Kullback-Leibler divergence is defined by:

$$D(\boldsymbol{x}||\boldsymbol{y}) = \sum_{l=1}^{L} p_l \log\left(\frac{p_l}{q_l}\right), \quad \textbf{(4.9)}$$

where $p_j = x_j / \sum_{l=1}^{L} x_l$ and $q_j = y_j / \sum_{l=1}^{L} y_l$. $\boldsymbol{x}$ and $\boldsymbol{y}$ are the two spectra being compared, in this case the atmospheric correction and the INMF radiance spectra. SID has been used extensively to quantify the performance of spectral unmixing routines (Chang, 2000; Jia & Qian, 2009; Nascimento & Dias, 2005; Plaza et al., 2004). For both RMS difference and SID, smaller values indicate higher similarity between spectra.

Table 4.1 and Table 4.2 provide the results of these quantitative metrics for the Hawaiian Islands and Florida Keys images, respectively. We examined how the spatial variability of the scene influences the INMF solution by computing the metrics for the full scenes and for subsets of the images.

Table 4.1: Hawaiian Islands image, RMS differences and SID values comparing the three INMF results against atmospheric correction results.
The smallest value for each measure is reported in bold.

	Full Scene		**Cloud-Free Subset**		**Dark Ocean, 2 Endmembers**		**Dark Ocean, 3 Endmembers**	
	RMS Diff	**SID**	**RMS Diff**	**SID**	**RMS Diff**	**SID**	**RMS Diff**	**SID**
Atmospheric Scattering	3.14	**0.0069**	**1.27**	**0.0069**	2.55	0.0178	6.70	**0.0069**
Water	1.40	**0.509**	**1.20**	1.01	4.55	3.91	1.85	0.722

Table 4.2: Florida Keys image, RMS differences and SID values comparing the three INMF results against atmospheric correction results.
The smallest value for each measure is reported in bold.

	Full Scene		**Dark Ocean, 2 Endmembers**		**Dark Ocean, 3 Endmembers**	
	RMS Diff	**SID**	**RMS Diff**	**SID**	**RMS Diff**	**SID**
Atmospheric Scattering	2.52	0.0259	**1.96**	**0.0026**	2.31	0.0259
Water	**1.22**	**0.753**	3.50	3.70	1.30	1.45

In both sets of images, the SID values for full scene or subsets of the scene the atmospheric endmembers are (nearly) identical. This is by design: the spectral shape of atmospheric scattering

endmember was fixed by the INMF algorithm and SID measures the difference between the shapes of two spectra. However, we found the dark-ocean subsets with two endmembers behaved differently. For these, the algorithm ran for fewer than 35 iterations before a lack of change in the cost function caused it to stop, in contrast to 300-500 iterations for the other subsets or full scenes. Examining the value of the cost function as the algorithm iterated (Figure 4.11) reveals that the two endmember dark-ocean subset failed to converge and did not change substantially after the first iteration. Due to the lack of iteration and convergence the INMF solution spectra were nearly unchanged from the initialization spectra even though the atmospheric scattering spectrum had not yet conformed to the fixed spectral shape. This explains why the SID value for the atmospheric scattering in the dark-ocean (2 endmember) subset does not match those from other subsets.

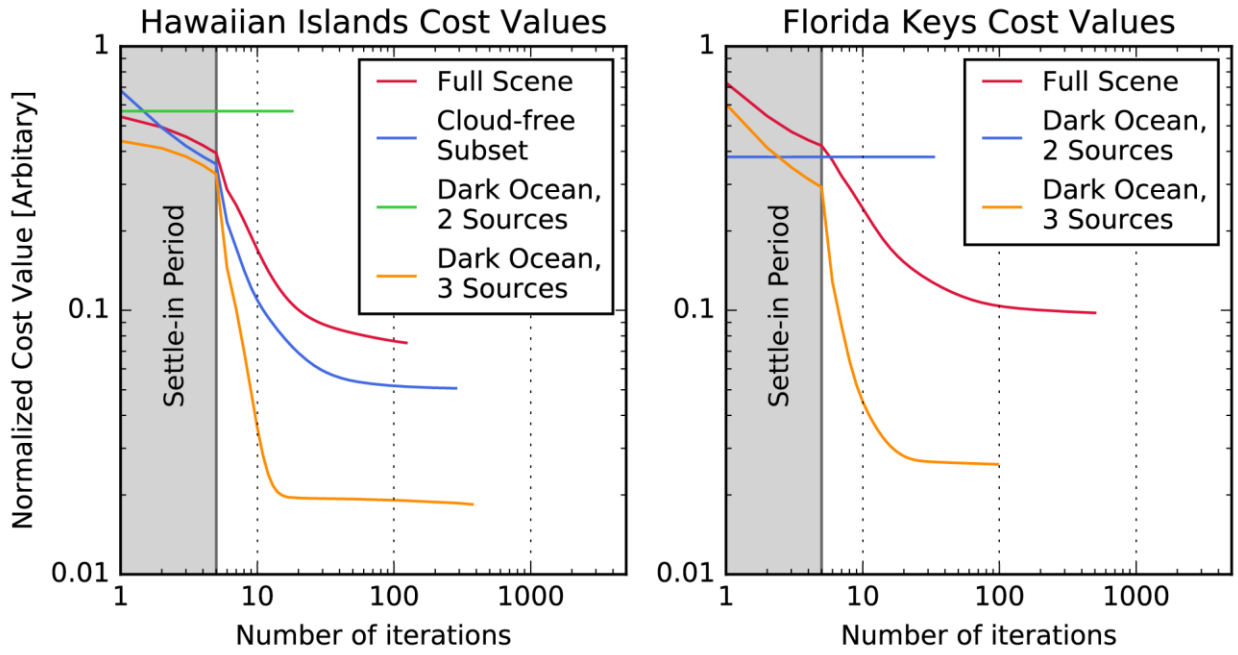

Figure 4.11: Value of the cost function at each iteration of the INMF while processing each image subset.
The five iteration long settle-in period before the endmember spectra are updated is shown in gray. The cost values are normalized by each scene's initial cost.

The failure of the INMF algorithm to converge prompted us to evaluate the minimum required number of endmembers. The dark-ocean subsets were processed again using three endmembers. A cloud-type endmember was added to the Hawaiian Islands image, and a vegetation endmember was added to the Florida Keys image. Although these endmember types were not actually present in the dark-ocean subsections of the image, adding them resulted in several hundred iterations, much greater convergence and significantly improved the results, reducing the RMS difference and SID. The abundances of these added endmembers remained small. The cloud endmember in the Hawaiian Islands dark-ocean subset had a mean abundance of 6.4% and the vegetation endmember in the Florida Keys dark-ocean subset had a mean abundance of 2.7%. From this we conclude that more than one endmember must be included in the abundance-sum-to-one constraint for the INMF algorithm, as currently implemented, to converge to a solution. This endmember does not need to be of a type that occurs in the scene, but it must be present to provide the degree of freedom required for the algorithm to update endmember and abundance values. Because our results for the dark-ocean subset with two endmembers failed to meet the physically imposed constraint in the spectral shape of atmospheric scattering, we exclude it in further discussion.

While the SID values for the other atmospheric scattering endmember should remain the same, the RMS differences should change between the respective subset results because the algorithm did not constrain the amplitude of the endmember. This was observed as expected.

In Table 4.1 and Table 4.2 we present values of two quantitative metrics, SID and RMS difference. The ideal INMF solution would match both the spectral shape and magnitude of the reference data and have low SID and RMS difference values. However, none of the scenes examined had the lowest value of all four metrics. The results still suggest some general trends.

We note that we have only processed scenes from these two images and the reference data was from an atmospheric correction model with its own uncertainty.

We find the INMF algorithm generally performed better on full images, as opposed to subsets of images, the exception being when a full image had cloud contributions. These results are surprising because we expected the simplest scenes, the dark-ocean subsets, to be easiest to separate. Instead the dark-ocean (3 endmember) subsets performed poorly compared to the full and cloud-free scenes. This suggests that spatial variability may improve the separation between endmembers and an extremely simple case may contain too few features for INMF to produce a well-separated result. However, we expect that there is a point above which increased spatial variability may decrease the ability of INMF to represent the scene. The work in this study focused on the lower limit of variability by examining scenes with few expected sources. Further study is need to determine uppers limits on the spatial variability and number of endmembers for INMF.

Clouds should be considered in the implementation of the INMF algorithm. We suggest that the very bright clouds contribute to higher RMS differences with respect to the L2GEN atmospheric correction model. For the full Hawaiian Islands scene, there is a significant radiance contribution from clouds over the dark ocean region, accounting for some of the difference shown in Figure 4.9b. We attributed the error caused by clouds to mixing between the atmospheric scattering and the cloud endmembers, which can be seen in the abundances maps shown in Figure 4.5. In Figure 4.5, both the cloud and atmospheric scattering spatial maps (panels (d) and (e)) have high abundance fractions over the cloudy regions in the top left of the image and over the islands. This suggests that there is a limit to the dynamic range that the algorithm can successfully unmix. Future work could lead to improvements which either increase the dynamic range of the INMF algorithm (or reduce the dynamic range of the radiances in the cloudy images) or otherwise

improve the cloud separation. For example, new constraints on cloud spectral shape could be investigated, or a pre-normalization procedure where all radiances in the image are normalized by the largest value at a single wavelength could be investigated. Separately, an initial cloud masking could be performed prior to running the INMF algorithm.

4.7.2. Sensitivity to the Magnitude of Initial Spectral Endmembers

We examined the sensitivity of the algorithm to variation in magnitude of the initial guess spectra by quantifying the variability in the resulting spectral endmembers. An algorithm where small changes in the initial conditions result in widely diverging solutions is less useful than one where a wider range of similar initial conditions converge to the same solution. We performed INMF on the full scene from the Hawaiian Islands image using 32 different sets of initialization spectra endmembers. The initialization spectra were produced by systematically perturbing the baseline spectra (Figure 4.6 left panel) in magnitude by -30% to +30%. The spectral shapes of the initializing endmembers were not changed. The range of resulting solution spectra are shown in Figure 4.12.

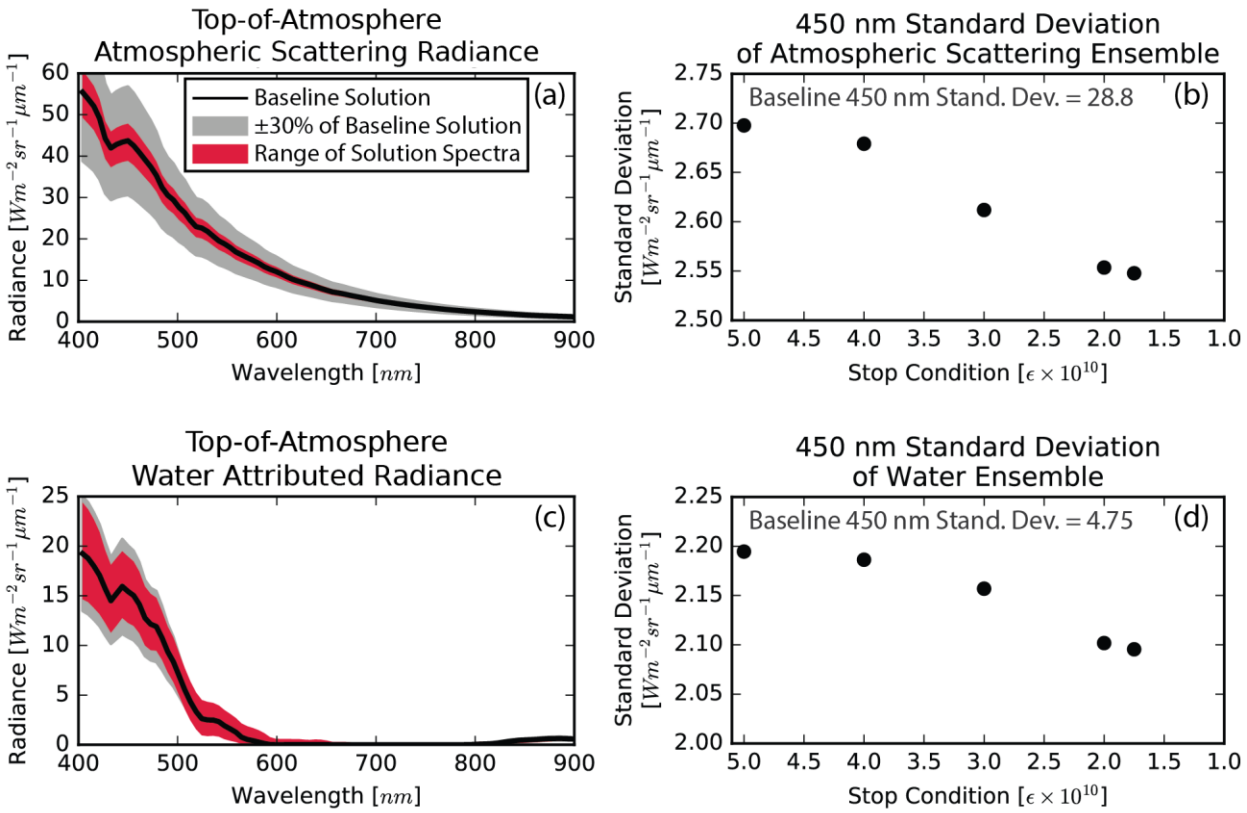

Figure 4.12: Results of sensitivity testing showing the range of initial guesses, range of solutions, and dependence on stop condition.

Panels (a) and (c) show the spectra. (a) is the atmospheric scattering endmember. (c) is the water endmember. The solid black line is the baseline solution spectrum. The spectra were taken from the radiance contributions of each endmember averaged over the dark-ocean subset of Box B in Figure 4.4. The gray shaded area shows a range of ± 30% of the baseline solution spectrum. The red shaded area shows the full range of the INMF solutions. Panels (b) and (d) are the 450 nm standard deviation of the ensemble of solutions shown in panels (a) and (c), respectively. The x-axis is the value of the stop condition, $\epsilon \times 10^{10}$. Smaller values of $\boldsymbol{\epsilon}$ result in more iterations. For reference the plots report the 450 nm standard deviation of an ensemble ± 30% of the baseline solution (gray shaded area of panels (a) and (c)).

Overall, the variation in the INMF solution endmembers is smaller than the variation of the initial guess spectra (Figure 4.12). When the spectral radiance values are small, as in the water endmember at wavelengths longer than 530 nm, the variation can exceed 30%. Perturbing the magnitude of the initial guess spectra did not result in endmember solution spectra with a different spectral shape. Other scenes might behave differently, and should be investigated in future work.

The ensembles converge as the number of iterations increases (Figure 4.12 panels (b) and (d)), which is expected. The scene was processed with the 32 initial condition sets with varying stop conditions, ϵ. A smaller stop condition leads to more iterations. Convergence was quantified by the standard deviation of the ensemble spectra, averaged over all wavelengths. The standard deviation decreased with smaller stop condition To provide a reference for these standard deviation values we assembled a 32 member ensemble of results by perturbing the baseline solution ± 30%. This ensemble represented the shaded gray region of Figure 4.12(a) and (b). This solution ensemble had 450 nm standard deviations of 28.8 and 4.75 for the atmospheric scattering and water spectra respectively. The standard deviation decreased only slightly through a wide range of stop conditions, indicating that the convergence is achieved slowly. Slow convergence has been previously reported with the update algorithm used by INMF (Berry et al., 2007). Smaller stop values required too much computing time to investigate.

This sensitivity analysis demonstrates that perturbing the magnitude of the initial endmember guesses by as much as ± 30% did not produce divergent solutions. Additionally, increasing the number of iterations led to further convergence of the ensemble members. This suggests that, at least for this scene and these constraint parameters, the INMF result is insensitive to minor differences in initialization magnitude.

4.8. Conclusions, Applications and Future Work

INMF has distinct advantages over conventional NMF and many other commonly used spectral unmixing methods. We have demonstrated that INMF is able to separate atmospheric and surface water contributions over a dark ocean region (Figure 4.9 and Figure 4.10) based on similarity in the separated contributions to the conventional model-based L2GEN atmospheric correction. The quality of the INMF separation, measured by similarity to the L2GEN analysis,

depended on the choice of scene, the selected number of endmembers, and the number of allowed INMF algorithm iterations. The best results, based on quantitative comparisons with the L2GEN atmospheric correction model, were achieved using full-scene images, or cloud-free subsets of the full images. The RMS difference for the cloud-free Hawaiian Islands scene was 0.68 and 1.20 $W \cdot m^{-2} \cdot sr^{-1} \cdot \mu m^{-1}$, for the atmospheric scattering and water radiances respectively. The normalized percent difference between the INMF and L2GEN values were: 3.4% and 24.9%. The values were normalized by the L2GEN radiance because L2GEN water radiance approached zero at longer wavelengths). The same values for the full-scene image of the Florida Keys were 2.52 and 1.22 $W \cdot m^{-2} \cdot sr^{-1} \cdot \mu m^{-1}$, and 13.1% and 38.5%. Ensemble testing of the INMF algorithm to magnitude changes in the initial guess spectra of up to ± 30% demonstrated that the ensemble solutions converged as the number of iterations of the algorithm increased.

For the two images examined in this study, processing larger subsets with more spatially variable land surfaces and atmospheric contributions produced INMF solutions that were more comparable to the L2GEN atmospheric correction results. We found worse performance for simple subsets of images, such as the dark-ocean subsets. This was contrary to our expectation that INMF would be most similar to the L2GEN results for simple scenes. We demonstrated that the abundance-sum-to-one constraint must include at least two endmembers for the algorithm to update correctly and converge to a solution. In comparisons against the model-based atmospheric correction this simple image result underperformed for the same scene processed with a third endmember, even if that third endmember, such as vegetation, did not actually appear in the subset of the image. This poor result was a result of the abundance-sum-to-one constraint which requires two or more endmembers within the constraint to iterate correctly.

The presence of clouds caused additional challenges for the INMF algorithm. We suggest the reason was high signal from very bright clouds, which led to a mixing of cloud and atmospheric scattering signals in the INMF solution. Cloud-masking, pixel-to-pixel signal level normalization, or physical constraints based on the spectral shapes of cloud radiances are possible research areas that could be tested in the future.

Further work is clearly needed to validate and fully characterize the INMF algorithm and explore possible applications. This work has examined only two images and a total of seven scenes from these images. Generalizing these results will require processing and evaluating a broader range HICO images, covering a wider range of conditions. This includes processing images with more challenging atmospheric conditions, such as heavier aerosol loading, or scattered cloud conditions. It also includes processing images with more complicated surface contributions, especially images with more land surface, coastal and shallow waters. These results suggest that more spatial variability from within a scene improves the INMF result. More work is need to determine how broadly applicable this conclusion is and to determine whether there is a limit at which increase variability begins to degrade the INMF results. In a similar direction this study established a lower limit for the number of endmembers required but an upper limit remains to be determined. The sensitivity of the INMF solution to the spectral shape of the initial guess spectra needs to be examined. Additionally, the sensitivity to various constraint parameters such as the smoothness constraint parameters ($\alpha, \beta, \gamma_W, \gamma_H$) should be explored.

The unsupervised selection of endmembers for techniques such as INMF is a more difficult problem, especially for highly mixed data (Bioucas-Dias et al., 2012; Pauca et al., 2006). For the scenes analyzed in this work, the number and type of the endmembers were chosen manually. Automatic selection of the number of endmembers should be a target of future work.

A desired outcome of spectral unmixing methods like INMF, is to connect the results from spectral endmembers and abundances fractions to physical properties. A study is in preparation to evaluate how aerosol properties can be retrieved from INMF results. We intend to use independent coincident observations, from the ground, or other satellite instruments, to independently evaluate the INMF results, rather than comparing to atmospheric correction routines.

Chapter 5

Evaluation of First Retrievals of Atmospheric and Surface Properties from Hyperspectral Imagery using Informed Non-Negative Matrix Factorization

5.1. Abstract

Hyperspectral instruments generate a large amount of spectral and spatial data. Connecting the spectral observations to radiative processes or sources is required for many applications, but it is difficult. Model-based property retrievals or atmospheric correction models are commonly used to make this connection, but have some drawbacks. Spectral unmixing is another approach. In this study we applied a spectral unmixing technique, Informed Non-Negative Matric Factorization (INMF), to relate the radiance observed at the top of the atmosphere to physical sources. In particular, we tested whether INMF results can be used to determine aerosol properties and seafloor bathymetry. We evaluated the INMF solution by comparison to in-situ measurements and independent remote sensing retrievals. The U.S. Coastal Relief Model was used as reference bathymetry data. An independent measurement of aerosol properties was provided by the Moderate Resolution Imaging Spectroradiometer (MODIS).

Hyperspectral imagery used for this work was acquired from the Hyperspectral Imager for the Coastal Ocean (HICO). We examined images collected over three coastal regions. Coasts are of particular scientific interest because of their ecological importance, sensitivity to climate

change, and their importance to human activities. They are also regions where it is often difficult to separate aerosol extinction from underlying ocean color features such as aquatic vegetation, suspended sediment, or seafloor in shallow regions.

The results of this study show that the INMF attributed aerosol radiance has a strong spatial correlation (R = 0.972) to MODIS retrieved aerosol properties. However, comparisons revealed significant differences over the spectral dimension. The closest agreement between INMF endmembers and radiances simulated from MODIS optical depths still differed by a root-mean-square (RMS) percentage difference of 33%. INMF abundance-derived seafloor depths have a mean absolute bias of 2.33 meters and a mean absolute percentage bias of 13.8% when compared to bathymetry data.

5.2. Introduction

Hyperspectral imagery used for this study was collected by the Hyperspectral Imager for the Coastal Ocean, (HICO) instrument onboard the International Space Station (ISS) (Lucke et al., 2011). This data set was selected because the instrument was spaceborne and HICO data can inform our use of planned orbital hyperspectral instruments. The HICO mission also had a strong focus on coastal ocean regions. Coastal ocean regions are important and interesting because of their ecological diversity, human commercial activity, and sensitivity to climate change, including impacts from rising levels, ocean acidification and storm intensification (Wong et al., 2014). Remote sensing in these regions is difficult. Coastal regions can be mixtures of deep ocean, shallower regions, wetlands, and estuaries that, when combined with low spatial resolution can result in a single imaged pixel containing a wide range of surface types, which complicates property retrievals, especially considering that coastal regions are also often close to sources of industrial pollutants and other continental aerosols (M. Corson et al., 2010; C. Davis et al., 2006;

C. O. Davis et al., 2007). Additionally, some assumptions that are commonly made for data retrievals cannot be applied to these regions, for example, that ocean surfaces have very low reflectances. In practice, this can result in poor data retrievals over coastal regions.

Model-based atmospheric correction routines are used to connect remote sensing observations to surface physical properties (B.-C. Gao et al., 2006; Goetz, 2009). Hyperspectral imagery has been used with model-based retrieval methods to derive a wide variety of science data products, including surface, vegetation and atmospheric properties (Goetz, 2009; Shaw & Burke, 2003).

Alternative approaches to model-based attribution are desired for hyperspectral remote sensing because of the volume of data collected and limitations to the accuracy of atmospheric correction models. Atmospheric correction requires radiative transfer models to derive atmospheric absorption and transmittance in order to infer the surface reflectance (Goetz et al., 1997). This process is dependent on input conditions, such as trace gas concentrations and spectral aerosol extinction. Uncertainty in these assumptions introduces biases that limit the accuracy of the derived surface reflectance (B.-C. Gao et al., 2009). One commercially available algorithm, Atmospheric/Topographic Correction for Airborne Imagery (ATCOR) (Richter & Schläpfer, 2015) is capable of retrieving surface reflectance with accuracies of 10-20% depending on the target's surface reflectance (Richter & Schläpfer, 2002). This level of uncertainty is larger than the radiometric accuracy of current generation instruments. For example, the Hyperspectral Imager for the Coastal Ocean (HICO) has a radiometric accuracy of 5% (Michael R. Corson et al., 2008). However, these uncertainties are far larger than what the next generation of hyperspectral imagers are expected to achieve. Instruments on the NASA Climate Absolute Radiance and Refractivity Observatory (CLARREO) mission will have accuracies on the order of 0.3% (Wielicki et al.,

2013). The difference between instrument accuracies and the larger retrieval accuracies suggests that more research on retrieval improvements is needed to exploit improved instrumental capabilities.

Numerical spectral unmixing methods use the large number of contiguous spectral channels provided by hyperspectral instruments to improve signal attribution. *Spectral unmixing*, or just *unmixing*, refers to algorithms that separate signals into their constituent spectral and spatial patterns (Keshava & Mustard, 2002) that ideally are attributable to a single source. Unmixing techniques were developed to exploit this additional spectral information for the signal attribution that is crucial to using these measurements for climate science applications. Spectral unmixing techniques are extensively used for land surface remote sensing problems such as identifying mineral types and distributions from surface reflectance data (Bioucas-Dias et al., 2012; Keshava & Mustard, 2002; Nascimento & Dias, 2005; Winter, 1999). In this work we applied a spectral unmixing technique to measurements that include atmospheric signals. This application of spectral unmixing techniques has been recognized (Bioucas-Dias et al., 2012) but is less well explored than surface remote sensing applications.

Many numeric unmixing techniques have been developed and applied to hyperspectral imagery including Independent Component Analysis (ICA) (Chiang et al., 2000; Comon, 1994), Principal Component Analysis (PCA) (Jolliffe, 2002; Roberts et al., 2014), N-FINDR (Winter, 1999), Pixel Purity Index (PPI) (Boardman et al., 1995), Non-negative Matrix Factorization (NMF) (D. D. Lee & Seung, 1999; Pauca et al., 2006), Vertex Component Analysis (VCA) (Nascimento & Dias, 2005), and many others (Keshava & Mustard, 2002). Each technique has its own benefits and disadvantages while some common limitations are shared by many methods. Many of these methods are based on measures of correlation such as orthogonality (PCA) or

mutual information (ICA) (Jolliffe, 2002). However, physically distinct sources are rarely spatially, spectrally or temporally uncorrelated (Rabbette & Pilewskie, 2001).

Additionally, many unmixing techniques have focused on surface signals, and are therefore, applied only to surface reflectances (Bioucas-Dias et al., 2012; Keshava & Mustard, 2002). Surface reflectances are retrieved from the observed at-flight level radiances through an atmospheric correction process (B.-C. Gao et al., 2009) which introduces biases and removes atmospheric information. Direct application of a numeric unmixing method to radiance avoids model-based atmospheric correction, and is intended to improve the accuracy of signal attribution and allow for the retrieval of atmospheric properties such as aerosol optical thickness (AOT).

We have developed an unmixing technique, Informed Non-Negative Matrix Factorization (INMF), that does not assume uncorrelated sources, and directly addresses atmospheric contributions. INMF, described in Chapter 4, is an algorithm based on Non-Negative Matrix Factorization (NMF) (D. D. Lee & Seung, 1999) that has been tailored for use in hyperspectral unmixing. INMF was developed specifically for unmixing at-sensor radiances and separating atmospheric and surface signals. INMF improves upon standard NMF approaches by introducing algorithmic constraints that are based on the physics of radiative transfer and generating an initial guess using library reflectance spectra. Chapter 4 of this thesis describes the development and validation of the INMF method in detail.

The goal of this study is to evaluate the efficacy of INMF spectral unmixing results for retrieving physical properties. The properties of interest in this study are aerosol optical thickness (AOT) and coastal bathymetry, or seafloor depth. We compare INMF-derived aerosol attributed radiance with reference data provided by co-located Moderate Resolution Imaging Spectroradiometer (MODIS) aerosol observations (Levy et al., 2013). The U.S. Coastal Relief

Model (NOAA National Centers for Environmental Information, 2001) was used as reference for comparison against INMF derived seafloor depths.

5.3. Informed Non-Negative Matrix Factorization

Informed Non-Negative Matrix Factorization (INMF) is a numerical spectral unmixing method that was developed specifically for separating atmospheric and surface contributions for measurements of at-sensor radiance. *At-sensor radiance* is the measurement of calibrated radiance that includes signals from all sources: molecular, aerosol, cloud scattering, and surface reflectance. A summary of the INMF method is presented in this section and a more detailed description of the technique is provided in §4.4.

5.3.1. INMF Algorithm

INMF factors a hyperspectral image, $\boldsymbol{A}$, into *spectral endmembers*, $\boldsymbol{W}$, representing the spectral shape of each separated source, and *spatial abundances*, $\boldsymbol{H}$, which describe the prevalence of the corresponding endmember in each image pixel (Figure 4.1). The INMF algorithm solves for the spectral endmembers and spatial abundances by minimizing a cost function. A standard NMF cost function is the square of the Euclidean distance between the original image and the NMF approximation (D. D. Lee & Seung, 2001): $D(\boldsymbol{W},\boldsymbol{H}) = \|\boldsymbol{A} - \boldsymbol{WH}\|^2$. However, the INMF cost function introduces additional constraints to guide the INMF solution to a more physically realistic result. These include terms that constrain spectral and spatial smoothness, inherent properties of hyperspectral imagery from natural scenes such as a field or forest region at the typical spectral and spatial resolution of hyperspectral sensors (Hunt, 1977; Jia & Qian, 2009).

INMF also uses an Abundance-Sum-to-One (ASO) normalization that scales the abundance values for each pixel into relative fractions of each endmember to the total abundance of the pixel (Heinz & Chang, 2001; Jia & Qian, 2009). Producing fractional abundances simplifies

the interpretation of the INMF output. However, the atmospheric endmembers are excluded from the ASO constraint. Consider a highly variable land surface below an unchanging atmosphere. In this scenario, while the absolute signal contribution from the atmosphere is constant over all the pixels, the relative strength of the surface and atmosphere contributions would vary significantly. Since the atmospheric spectral endmember is shared by all pixels, the NMF result with an ASO constraint would be unable to produce a correct representation of the atmosphere. To address this limitation, we have excluded the atmospheric endmembers of molecular and aerosol scattering from the ASO constraint.

Lastly, we have fixed the spectral shape of the molecular scattering endmember. Unlike many surface reflectance spectra, the spectral shape of molecular scattering is well known since it follows Rayleigh's law (Bodhaine et al., 1999). We constrained the spectral shape of the molecular scattering endmember at each iteration of the INMF algorithm so that only its magnitude can vary in each iteration.

5.3.2. Informed Initial Endmember Spectra

A potential limitation of INMF is that it must be given an initial guess of the endmember spectra, $\boldsymbol{W}$, and the spatial abundances, $\boldsymbol{H}$. This type of algorithm is also known to be sensitive to the choice of initial values (Berry et al., 2007; Pauca et al., 2006). A key feature of INMF is the use of library reflectance spectra and radiative transfer modeling to produce initial guesses of the endmember spectra. At-sensor radiance spectra for the initial guesses were modeled using MODTRAN 5.3 (Berk et al., 2006). The lower boundary condition model input of surface spectral reflectance was from the ASTER Spectral Library (Baldridge et al., 2009). By starting the iterative INMF algorithm with known source spectra, we expect that it is more likely for the solution spectra to also be physically plausible spectra. Spatial abundances were distributed uniformly across a scene.

5.4. Method

To analyze a hyperspectral image with INMF the algorithm must be provided with three pieces of information: the number of endmembers, and initial endmember spectra and abundance fractions. The target retrievals for this study were aerosols and seafloor depth. For INMF to separate these signals, additional aerosol and seafloor endmembers was added to the INMF expected scene endmember spectra and spatial abundances arrays (***W*** and ***H***).

Other endmember types were selected based on visual inspection of the scene. They included open ocean, soil, concrete, vegetation, and molecular scattering. Automating methods for selecting the number and type of endmembers for NMF and related unmixing approaches is an open area of research (Bioucas-Dias et al., 2012; Pauca et al., 2006). This set of endmembers was then input into the INMF algorithm which iterates until the solution changes by a small amount between iterations. This threshold value was based on the number of pixels, and signal level of the scene. It was set by multiplying a small number, $5 \cdot 10^{-10}$, by the sum of radiance across all pixels and wavelengths. For these three scenes, the resulting average cutoff cost function change was 3, or approximately $1 \cdot 10^{-5}$ times the initial cost function value. The INMF output is radiance spectra and spatial abundances for each endmember.

5.5. Data

5.5.1. Hyperspectral Imager for the Coastal Ocean (HICO)

The Hyperspectral Imager for the Coastal Ocean (HICO) was sponsored by the U.S. Office of Naval Research and operated on the International Space Station (ISS) from September 2009 through September 2014 (Lucke et al., 2011; Oregon State University, 2015). The final two years of HICO operation were supported by NASA's International Space Station Program (Oregon State University, 2015). HICO had 128 wavelength channels between 352 nm and 1080 nm. This work

used the subset of channels between 400 nm and 900 nm where the HICO instrument team stated that “The HICO produces its best data…” (Lucke et al., 2011). The details of the HICO instrument and the dataset used in this work were presented in full in §4.5.

5.5.2. MODIS Aerosol Retrievals

Moderate Resolution Imaging Spectroradiometer (Ardanuy et al., 1991) observations provide an independent retrieval of aerosol optical thickness. For this analysis we used the aerosol optical depth retrieved with the dark target algorithm (Levy et al., 2013) over the ocean portions of the images. We used the 3 km MODIS Collection 6 Atmosphere Level-2 Aerosol Products (Levy et al., 2013). The 3 km data was used because the standard 10 km MODIS data is coarse compared to the nominal HICO resolution of 90 m.

One limitation when comparing HICO and MODIS observations is finding contemporaneous observations. HICO was onboard the International Space Station while the MODIS instruments are on the Aqua and Terra satellites. These spacecraft have orbits with different periods, inclinations, and altitudes so HICO and MODIS were often imaging different regions. This leads to difficulty in finding HICO images that match the time and location of MODIS data. The images used in this study were selected because the MODIS data were collected within 30 minutes of the HICO imagery.

5.5.3. U.S. Coastal Relief Model Bathymetric Data

We used the U. S. Coastal Relief Model, produced by National Oceanic and Atmospheric Administration (NOAA)’s National Centers for Environmental Information, as an independent measurement of seafloor depth. The bathymetric data covers the coastal regions of the continental US, Hawaii and Puerto Rico with a resolution of 3 arc-seconds (approximately 93 meters at the equator, 66 meters at 45° latitude) (NOAA National Centers for Environmental Information, 2001). The U.S. Coastal Relief Model data products aggregate measurements from a wide number

of sources including the hydrographic soundings from NOAA's National Ocean Service, multi-beam and track-line sonar surveys, and information from the International Bathymetric Chart of the Caribbean Sea and the Gulf of Mexico project (NOAA National Centers for Environmental Information, 2001). The coastal relief model for Florida and the East Gulf of Mexico that we use in this study reports an assumed vertical accuracy no better than 1 meter (NOAA National Centers for Environmental Information, 2001). Similar coastal relief models report bathymetric vertical accuracies between 0.1 m and 5% (Calsbeek et al., 2013; Grothe et al., 2011). We will assume the accuracy of this data set is the less accurate of 1 m absolute or 5% relative.

5.6. INMF Aerosol Retrievals

5.6.1. Initial Aerosol Endmember Spectra

We selected two HICO images (Figure 5.1 center and right) to evaluate the INMF separation aerosol signals from surface reflectance and molecular scattering based on three criteria: availability of contemporaneous MODIS observations; MODIS retrieved 550 nm aerosol optical thicknesses greater than 0.3; and at least a portion of the image over a region of dark ocean. These criteria were met by images of the Persian Gulf (Figure 5.1, center) and of the Korean Peninsula and Yellow Sea (Figure 5.1, right). MODIS aerosol retrievals reported scene-averaged 550 nm AOT for the Persian Gulf scene was 0.49 and 1.04 for the Korean Peninsula. Together the two images cover a range of 550 nm aerosol optical thicknesses from 0.3 to 1.2. Dark ocean surfaces are ideal for validating INMF results because contributions are only expected from three sources: the water surface, molecular scattering, and aerosol scattering. Limiting the number of

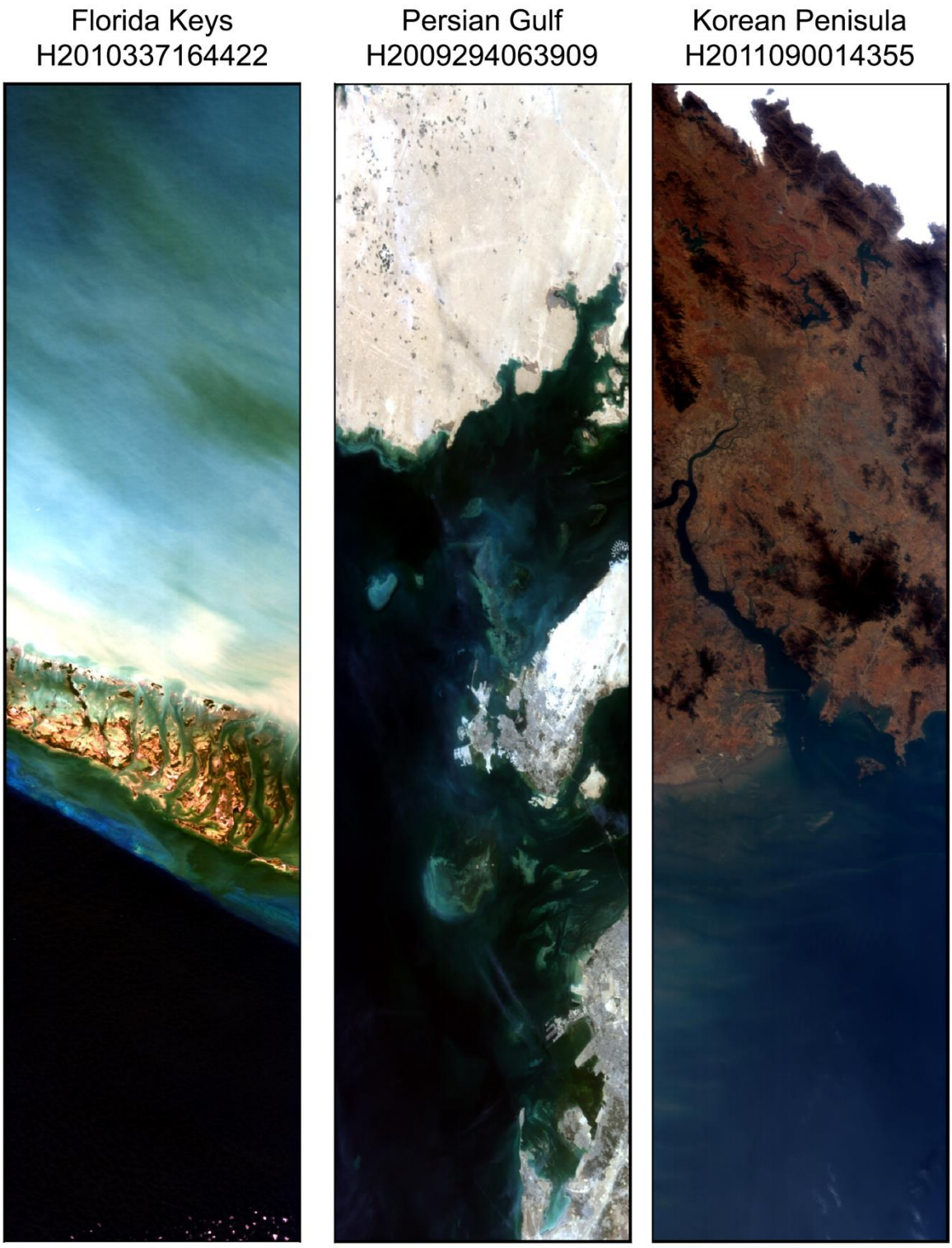

Figure 5.1: Three HICO images of scenes with different aerosol optical depths.
The scenes, from left to right, are centered on the Florida Keys, the island of Bahrain in the Persian Gulf and the city of Nampo on the Korean Peninsula. The number above each image is the HICO ID which corresponds to the time and date of the imagery in the format: YYYYDDDHHMMSS. The three number long day identifier (DDD) refers to the day of the year.

expected contributions simplifies the validation of the results, in contrast to highly inhomogeneous coastal ocean or land scenes that include a wider range of surface types. Further simplification of unmixing problem is provided by reflectance from dark ocean water surface that is small compared to the two scattering terms.

To separate the aerosol signal from molecular scattering and surface reflectance contributions, we added an endmember to represent the radiance due to aerosol scattering to the set of INMF endmembers. We did not assume an a-priori aerosol composition. Instead, we generated five initial guesses of the aerosol scattering radiance using the MODTRAN 5.3 radiative transfer model (Berk et al., 2006) and five different aerosol profiles and spectra properties (Figure 5.2). For four of these spectra, we used aerosol properties and profiles that are defined in MODTRAN as standard aerosol models. These aerosol model profiles are defined by the region (rural, urban, or desert) and the meteorological visibility, which is a proxy for AOT (Berk et al., 2013). The MODTRAN defined spectra used the standard MODTRAN aerosol models for Rural with 5 km visibility, Rural with 23 km visibility, Urban, and Desert. A fifth aerosol radiance spectrum was generated by MODTRAN using the MODIS retrieved aerosol spectral optical thickness. A mid-latitude winter atmospheric profile was used for the Korean Peninsula image and a standard mid-latitude summer profile was used for the Persian Gulf image. In addition to the aerosol properties, the solar and observation angles were set to match the HICO observing geometry. Other properties, such as column water vapor, were defined by the standard atmospheric profiles.

The initial guess of the aerosol spectrum was then added to the array of other initial endmembers. The aerosol endmember was excluded from the abundance-sum-to-one constraint, as was the molecular scattering endmember.

INMF was run five times on each HICO image, once with each initial aerosol spectrum. The Korean Peninsula image was processed with a set of six endmembers: water, soil, vegetation, concrete, aerosol, and atmospheric scattering. The Persian Gulf image was processed with five endmembers, water, soil, shallow water, aerosol, and atmospheric scattering. The result of this processing is a set of endmember spectra and abundance fraction maps (Figure 5.3 and Figure 5.4).

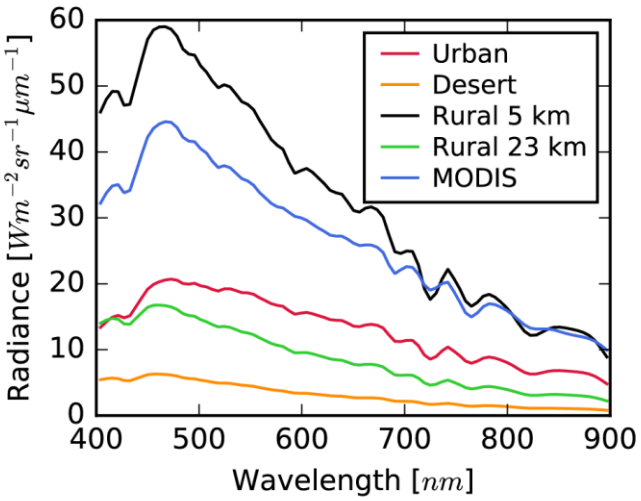

Figure 5.2: Modeled top-of-atmosphere radiance due to aerosol scattering using five different aerosol profiles.
Four are MODTRAN standard aerosol profiles, Urban, Desert, Rural with 5 km visibility and Rural with 23 km visibility and the last used the MODIS retrieved aerosol properties. These spectra were generated for the Korean Peninsula Scene (Figure 5.1 right panel)

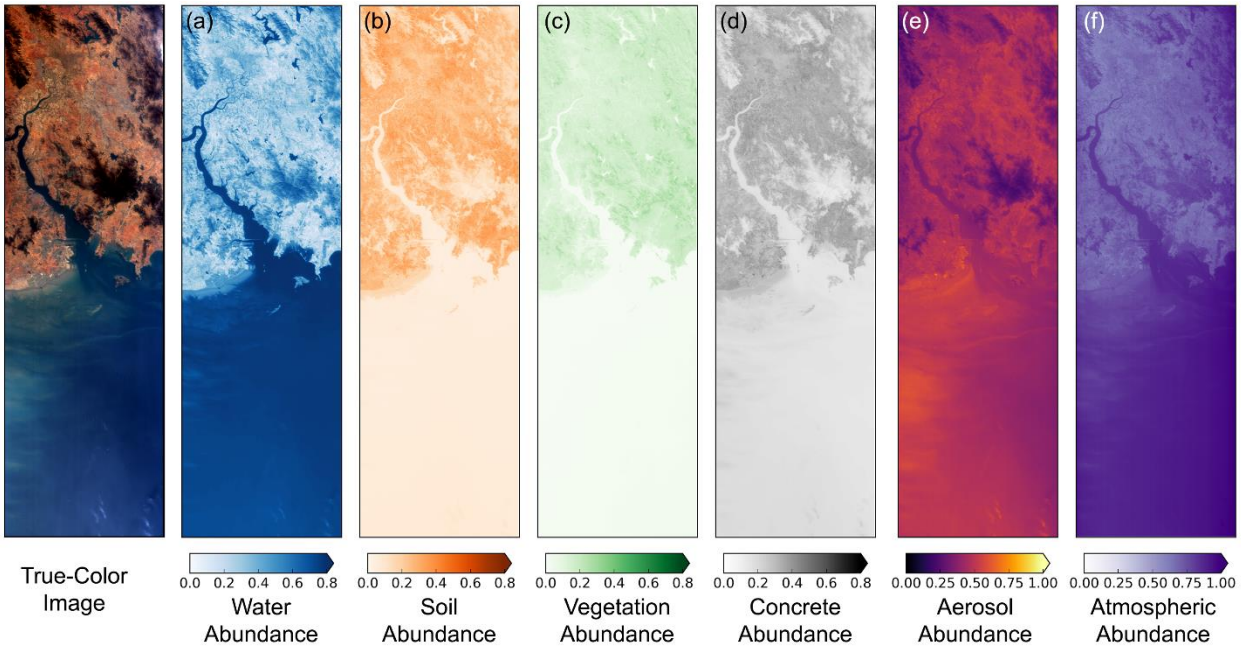

Figure 5.3: The INMF solution abundances for the HICO image of the Korean Peninsula and coastal Yellow Sea.
The left-most panel is a true-color image of the scene and the remaining maps show the abundance fraction of each endmember.

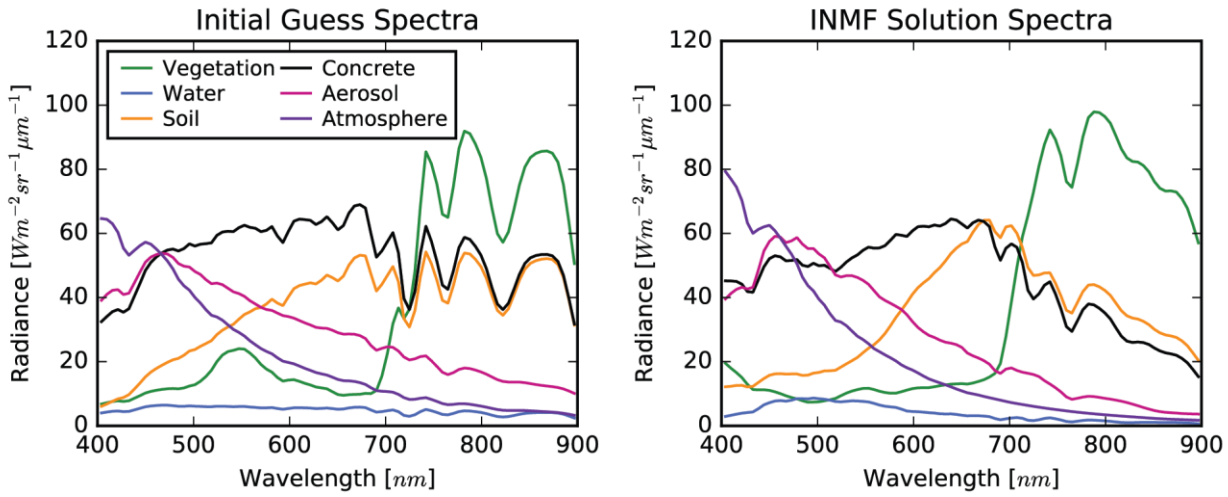

Figure 5.4: INMF endmember spectra for HICO image of the Korean Peninsula and coastal Yellow Sea.
The spectra correspond to the maps of abundance values from Figure 4.5. The spectra in the left panel were used to initialize the INMF algorithm. The right panel shows the corresponding INMF solution spectra.

5.6.2. Comparison of MODIS Aerosol Properties and INMF Results

Evaluating and understanding the INMF output requires examination of both spectral and spatial results. For hyperspectral instruments, such as HICO, this necessitates relatively high spatial and spectral reference data. To simplify the validation, we focused only on the ocean regions of the HICO images. Over ocean it is simpler to isolate radiance due to aerosol because there should be only one surface contribution, water reflectance. MODIS aerosol retrievals include spectral and spatial information, though at much lower resolutions than HICO.

Aerosol abundance fraction is the spatial component of the INMF aerosol scattering endmember, so ideally it should vary in the same spatial patterns as the MODIS aerosol retrievals if both retrievals are accurate. Figure 5.5 shows the INMF aerosol abundance plotted against the MODIS 550 nm AOT. For this comparison the 3 km MODIS data was used because the finer spatial resolution provides 220 observations over the HICO image. The standard MODIS aerosol products at 10 km resolution would only provide 23 data point across the image. Both MODIS products have many fewer observations than the 325,000 HICO spatial pixels over in the same location.

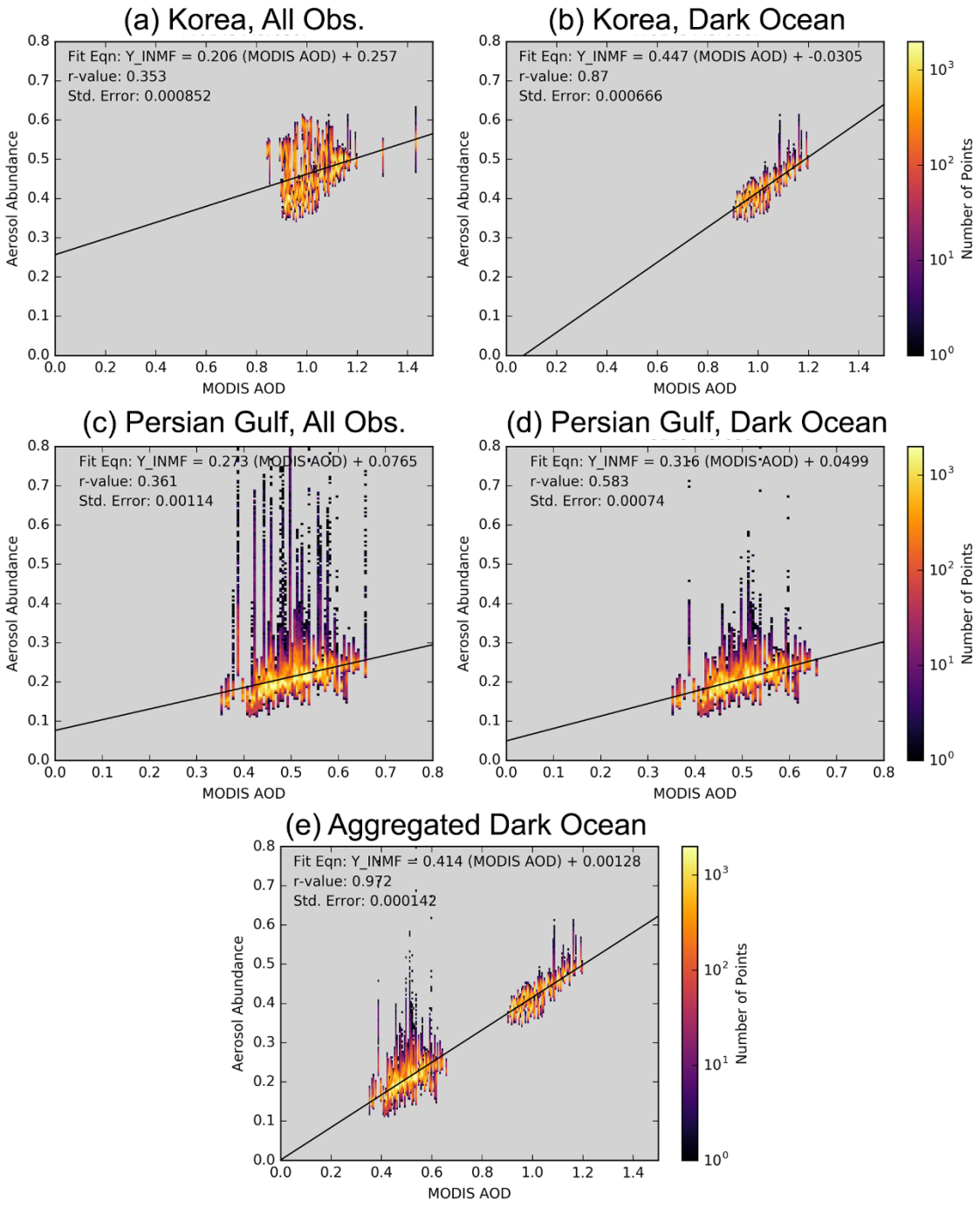

Figure 5.5: INMF Aerosol Abundances plotted against the MODIS retrieved 550 nm AOT. The data were binned. Bins are colored by the number of points they contain. (a) and (b) show results for the Korean Peninsula image; (a) includes all points that had MODIS aerosol retrievals and (b) only includes points from the dark ocean regions of the image. (c) and (d) show results for the Persian Gulf image; (c) includes all points that had MODIS aerosol retrievals and (d) excludes data points from shallow regions, determined by where INMF reported seafloor abundances greater than 0.5. (e) aggregates the results from (b) and (d) for the dark ocean portions of the Korean Peninsula and Persian Gulf images.

For the Korean Peninsula image Figure 5.5a shows the resulting plot of INMF aerosol abundance against MODIS AOT. The two values are poorly correlated as demonstrated by the scatter plot. Examination of the aerosol abundance maps (Figure 5.3e) shows that the aerosol signal is mixed with surface signals in coastal regions with variable ocean color. This occurs on the left side of the image and can clearly be seen at the river's mouth where the two water masses mix. Separating signals in coastal regions is difficult due to the number and variety of possible contributors to reflectance spectrum (C. Davis et al., 2006). This increased surface variability also reduces the effectiveness of the MODIS retrieval. The MODIS aerosol property retrieval includes a quality control flag that rates the retrieval as 'very good', 'good', 'marginal', or 'poor' (Levy et al., 2013). In the regions of this scene with highly variable ocean color the MODIS reported quality decreases from 'very good' to 'marginal'. Without ground truth measurements we cannot determine whether the error is in the INMF separation, MODIS property retrieval, or a combination of both.

Excluding these areas with significant additional surface contributions produces a much stronger correlation between the MODIS AOT and the INMF aerosol abundance. Figure 5.5b reproduces the first scatter plot but uses only that data from the dark ocean region at the bottom right corner of the image. This reduces the number of HICO data points to 144,000. A linear fit produces a correlation coefficient, R-value, of 0.870. This value is similar to the reported global correlation of MODIS retrievals to AERONET 550 nm optical thicknesses (Levy et al., 2013).

The Persian Gulf image (Figure 5.2, at center) has slightly more coincident MODIS retrievals, 239 at 3 km resolution versus 379,500 HICO spatial pixels. This scene, like the Korean Peninsula image, has regions of shallow water that have higher reflectance where INMF did not adequately separate the aerosol contributions from the surface signal. This results in a large spread

in the data in the abundance fraction dimension (seen as the vertical outliers in Figure 5.5c). Complications due to variable ocean color were expected for this image and can be easily identified in the true-color image. In attempt to separate the shallow water contributions from the aerosol signal we added a shallow water endmember before performing INMF on the image. This approach was not entirely successful as evidenced by the outliers in Figure 5.5c. However, the abundance of the shallow water endmember does correlate with these higher reflectance shallow regions. The shallow water endmember was used to remove the shallow regions by plotting only those data points where the abundance of the shallow water endmember was less than 0.5. This eliminated many of the outliers, producing the better correlated (R = 0.583) distribution shown in Figure 5.5d.

These two images included different ranges of aerosol optical thicknesses: 0.8 to 1.2 in the Korean Peninsula image, and 0.3 to 0.7 for the Persian Gulf. To combine the INMF results to cover this entire range of aerosol conditions we aggregated the results from these two images (Figure 5.5e). It should be noted that the aerosol abundance derived by INMF is sensitive to surface reflectance and scene illumination so two scenes with identical aerosol abundance may differ in their INMF result. Nonetheless, the aggregated comparison is quite promising, with R = 0.972.

These results demonstrate that the INMF is appropriately identifying the spatial patterns of aerosol scattering. However, in the coastal regions of both images the INMF aerosol abundance values have a broader distribution that is less well correlated with the MODIS AOT values. Both the MODIS retrievals and the INMF results had increased uncertainty in these regions. The MODIS aerosol quality decreased to ‘marginal’, and uncertainty could be seen in the INMF result as an increased attribution of radiance from a non-aerosol source to the aerosol endmember. However, there are possible solutions to reduce this mixing that should be a topic of further investigation. First, additional endmembers could be introduced to account for the mixed signal.

This approach was partially successful in adding a shallow-water endmember to the Persian Gulf image. Another approach that could improve separation is to introduce additional constraints, although more investigation is required to determine what constraints would be appropriate to enhance separation. One possibility would be to limit the similarity in spectral shape between the aerosol and other endmember spectra.

INMF also produces a spectrum of each endmember. We evaluated the spectra first by quantifying the radiance attributed to the aerosol endmember in each pixel. This is the product of abundance fraction and the aerosol spectrum. The same quantity was approximated for the MODIS retrieval. This was done by using the MODTRAN radiative transfer model, using the MODIS retrieved aerosol spectral properties and optical thickness as input to model the MODIS radiance attributed to aerosols. MODIS retrieves aerosol properties at only seven wavelengths, four of which (470 nm, 550 nm, 660 nm, and 860 nm) are within HICO's wavelength range. To compare to the INMF output, the MODIS spectral properties were interpolated between these four wavelengths.

Figure 5.6 shows three sets of spectra from the INMF processing of the Korean Peninsula and Persian Gulf scenes: the initial aerosol radiance spectra produced with MODTRAN and used as inputs to the INMF algorithm, the solution spectra produced by INMF, and the radiance attributed to the aerosol by INMF, calculated as the product of the spectra and abundance fraction for the mean aerosol abundance over the image. Note that the absolute magnitudes of the INMF solution aerosol spectra are not particularly important because the abundances were allowed to vary freely. As mentioned above the product of the endmember spectra and abundance (Figure 5.6, bottom row) shows the relevant comparison of absolute radiances.

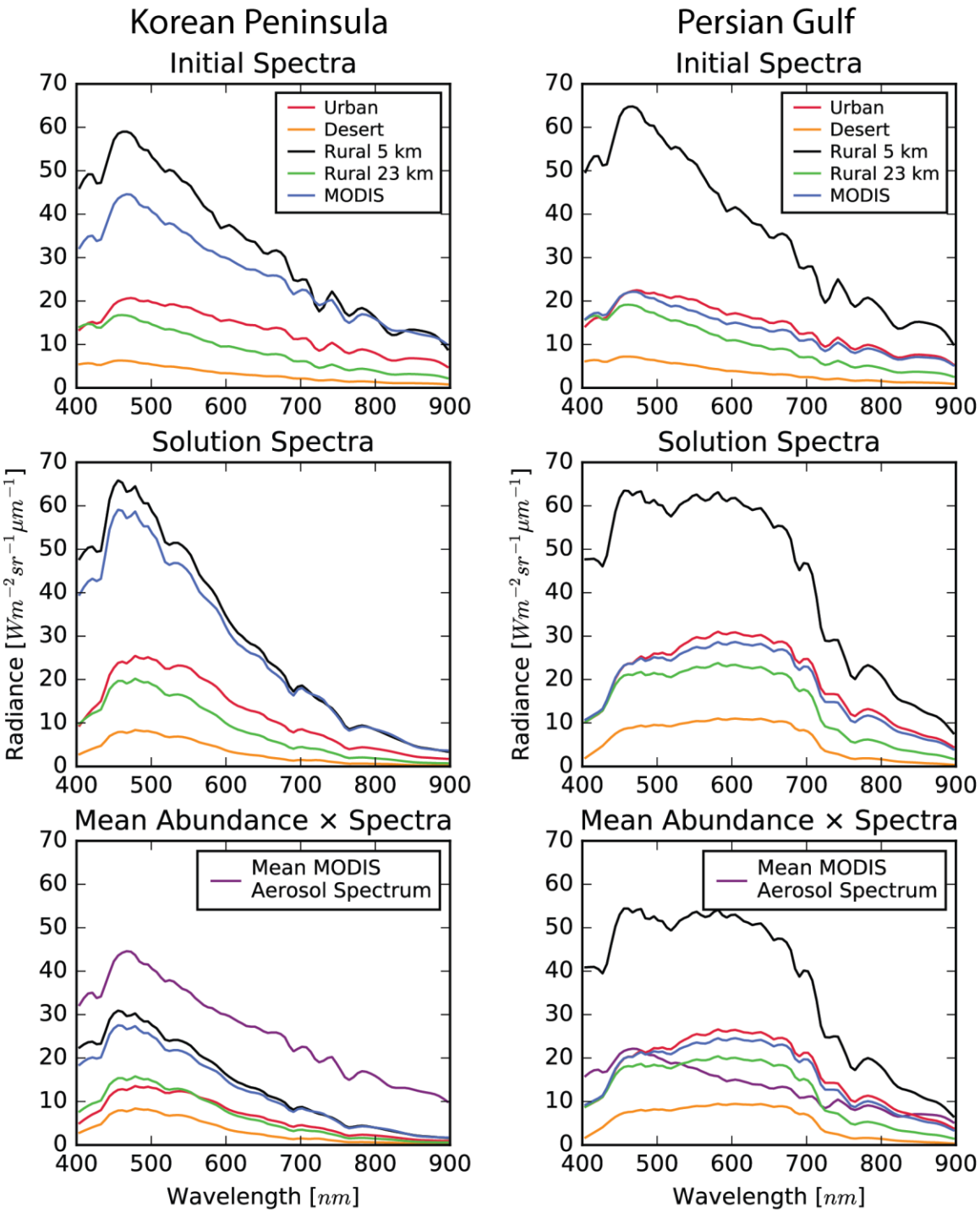

Figure 5.6: Aerosol radiance spectra for the Korean (left column) and Persian Gulf images (right). The top row shows the MODTRAN modeled aerosol spectra that were used as initial guesses for the INMF algorithm. The center row is the resulting INMF endmember spectra for each initial aerosol spectrum. The bottom row shows the reconstructed radiance attributed aerosol for the mean aerosol abundance over the image. This is the product of the INMF aerosol endmember spectra and abundance fraction. For reference the modeled aerosol radiance using the scene averaged aerosol properties retrieved with MODIS is shown with the purple line.

We applied two quantitative metrics to compare the INMF solutions from the five different aerosol types to each other and to the modeled MODIS aerosol spectra. Comparing the INMF results from different initial aerosol spectra indicates how sensitive the INMF result is to the initial guess. While comparing each result to the MODIS derived aerosol spectra provides a measure of how well INMF isolates the aerosol signal from other surface and atmospheric contributions. Although we use MODIS observations as a benchmark to compare with the INMF results they are not ground truth measurements. MODIS retrievals of aerosol optical thickness have their own retrieval challenges with potentially high uncertainties.

The first comparison metric is the root-mean-squared (RMS) difference between the INMF and modeled MODIS aerosol radiance spectra. RMS difference measures the absolute difference and the similarity of the magnitudes of the two signals. An additional measure is necessary to evaluate the spectral shape similarity between the atmospheric correction and INMF results. For this we employed the Spectral Information Divergence (SID) (Chang, 2000). SID is calculated as the sum of the Kullback-Leibler divergences, $D(\boldsymbol{x}||\boldsymbol{y})$, calculated for each spectrum with respect to the other, so the $SID(\boldsymbol{x},\boldsymbol{y}) = D(\boldsymbol{x}||\boldsymbol{y}) + D(\boldsymbol{y}||\boldsymbol{x})$. Kullback-Leibler divergence is defined by:

$$D(\boldsymbol{x}||\boldsymbol{y}) = \sum_{l=1}^{L} p_l \log\left(\frac{p_l}{q_l}\right),$$

where $p_j = x_j / \sum_{l=1}^{L} x_l$ and $q_j = y_j / \sum_{l=1}^{L} y_l$. $\boldsymbol{x}$ and $\boldsymbol{y}$ are the two spectra being compared, in this case aerosol attributed radiance spectra derived from INMF and MODIS. SID has been used extensively to quantify the performance of spectral unmixing routines (Chang, 2000; Jia & Qian, 2009; Nascimento & Dias, 2005; Plaza et al., 2004). For both RMS difference and SID, smaller values indicate higher similarity between spectra.

The SID between the various aerosol endmember spectra for the INMF using different initial aerosol spectra provides insight into the performance of the algorithm. Table 5.1 shows the

SID values for a comparison between all solution aerosol endmember spectra. For the Korean Peninsula image the largest of these values is 0.0626. The Persian Gulf image exhibited lower convergence with a largest SID value of 0.1050. As a point of reference, the mean SID between two randomly generated spectra is approximately 1.0. These small SID values indicate that there is similarity between all of the solution aerosol endmember spectra. This suggests that the spectral shape produced by INMF is insensitive to the choice of initial aerosol spectrum within the range tested here. Aerosol radiative properties can vary significantly depending on the type, shape size distribution and chemistry of the aerosols (Tanré et al., 1997). Our results suggest that it may be sufficient to consider a single generic initial aerosol profile which greatly simplifies the analysis. More images, covering a broader range of aerosol cases, will need to be examined to validate this conclusion.

Table 5.1: Spectral Information Divergence between the INMF solution Aerosol spectra for the Korean Peninsula image (top) and the Persian Gulf image (bottom)

Korean Peninsula

Initial Aerosol Type:	*Urban*	*Desert*	*Rural (Vis=5km)*	*Rural (Vis=23 km)*	*Average MODIS*
Urban	0.	0.0626	0.0353	0.0378	0.0244
Desert		0.	0.0522	0.0096	0.0570
Rural (Vis = 5km)			0.	0.0174	0.0019
Rural (Vis = 23 km)				0.	0.0212
Average MODIS					0.

Persian Gulf

Initial Aerosol Type:	*Urban*	*Desert*	*Rural (Vis=5km)*	*Rural (Vis=23 km)*	*Average MODIS*
Urban	0.	0.1050	0.0409	0.0449	0.0017
Desert		0.	0.0967	0.0263	0.0901
Rural (Vis = 5km)			0.	0.0220	0.0272
Rural (Vis = 23 km)				0.	0.0312
Average MODIS					0.

Table 5.2: RMS Difference and Spectral Information Divergence values between the aerosol attributed radiance spectra from the modeled mean MODIS aerosol properties and the INMF derive aerosol endmember for 5 INMF solutions processed with different initial aerosol spectra.

	INMF Initial Aerosol Spectrum	***RMS Difference*** $[W \cdot m^{-2} \cdot sr^{-1} \cdot nm^{-1}]/[\%]$		***Spectral Information Divergence***
Korean Peninsula	*Urban*	20.8	78.6 %	0.108
	Desert	24.3	90.3 %	0.296
	Rural (Vis = 5km)	12.5	57.6 %	0.135
	Rural (Vis = 23 km)	20.4	80.0 %	0.217
	Average MODIS	13.8	60.2 %	0.112
Persian Gulf	*Urban*	6.77	41.3 %	0.106
	Desert	8.53	62.8 %	0.267
	Rural (Vis = 5km)	26.6	166.9 %	0.051
	Rural (Vis = 23 km)	4.03	33.1 %	0.129
	Average MODIS	5.64	33.8 %	0.093

We compared the INMF derived aerosol radiance spectra to the radiance spectrum modeled using the MODIS retrieved aerosol properties. The spectra used for the comparison are an average over the image. This comparison shows significant differences in the magnitudes of the MODIS derived spectrum and all of the INMF results. For the Korean Peninsula image, all of the INMF result spectra differed from the MODIS derived spectrum by RMS percentage differences greater than 57%. While Table 5.1 shows that the INMF derived aerosol spectra were similar to each other, Table 5.2 shows that they are an average of 3 times less similar to the MODIS derived spectrum. The SID values averaging 0.174, triple the largest SID from the inter-comparison of INMF solution aerosol spectra.

Compared to the Korean Peninsula image, the SID and RMS difference results for the Persian Gulf image are slightly lower. The exception is the INMF solution initialized with a Rural aerosol profile and 5 km visibility, which produced a significant overestimate of the magnitude of the aerosol radiance. The other INMF solutions more closely match the MODIS data with RMS

percent differences between 33.1 and 62.8%. The shapes of the aerosol spectra are also a slightly closer match to the MODIS derived spectrum with an average SID of 0.129, ¾ of the average SID of for the Korean Peninsula results.

5.7. Bathymetry Retrievals

Seafloor depth, or bathymetry, is a common retrieval target for hyperspectral imagery, particularly from instruments like HICO. Bathymetric retrieval algorithms have been developed using a range of techniques from model-based methods (Adler-Golden et al., 2005) to neural networks (Sandidge & Holyer, 1998). Given the interest in retrieving coastal region bathymetry from hyperspectral imagery we attempted to retrieve it using the INMF method. We are able to compare the INMF derived bathymetry to independent measurements from in-situ sounding methods.

Our evaluation focused on a shallow region of the Gulf of Mexico located to the north of the Florida Keys. This area was selected because it is a large region, covering tens of thousands of square kilometers, in which the seafloor is shallower than 30 meters. A portion of the region, covering approximately 4000 km^2, can be seen as the highly reflective area at the top of the left panel of Figure 5.1. We have used the U.S. Coastal Relief Model (NOAA National Centers for Environmental Information, 2001) as a reference data source because it covers this region with similar spatial resolution (3 arc-second) to HICO's nominal resolution of 90 meters.

The process of retrieving seafloor depth using INMF is similar to the method used to retrieve aerosol signal in the previous section. An endmember is added to the INMF endmember spectra and abundance arrays to separate the radiance in each pixel that is attributed to the seafloor. The abundance of this seafloor endmember in any pixel is then used as a proxy for the seafloor depth. This method assumes that pixels of shallow water will have higher signal than a deep water

counterpart because the seafloor reflects more light than water. In theory, a seafloor endmember abundance of zero should occur when the seafloor is below the depth of light penetration. In practice, the seafloor abundance has a lower limit of approximately 0.0925 that appears even in ocean regions with depths greater than 100 meters where there are no seafloor contributions to observed radiance.

The initial guess of the seafloor endmember spectrum was intended to approximate the spectral shape of contributions from the ocean bottom. The initial guess was derived from the HICO image by taking a mean spectrum from the shallow portion of the image and subtracting the other expected contributions from the surface water and molecular scattering (Figure 5.7). This leaves a spectrum for the remaining radiance from those pixels, assumed to be contributions from the seafloor scattering.

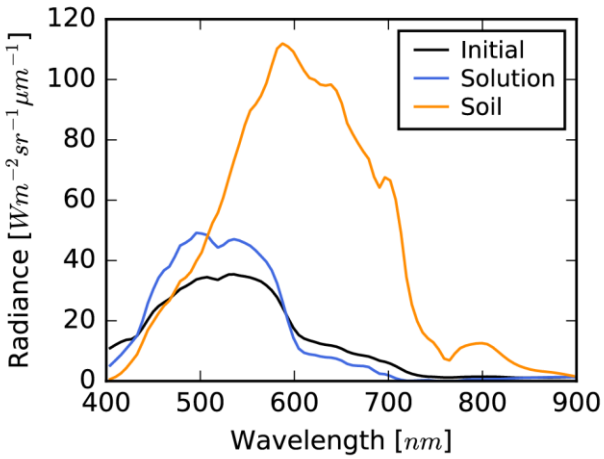

Figure 5.7: Seafloor endmember initial guess spectrum (black) and INMF solution spectrum (blue).The INMF solution soil endmember spectrum is also shown (orange).

The image is then processed using the INMF algorithm with five endmember types: vegetation, water, soil, seafloor and atmospheric scattering. The contributions of aerosol scattering were neglected because the average MODIS retrieved 550 nm AOT for this image was below 0.05.

After processing with INMF, the seafloor endmember spectrum maintained a spectral shape similar to the initial guess, with a peak at 500 nm before decreasing rapidly near 600 nm (Figure 5.7). The corresponding seafloor abundance is shown in Figure 5.8b. To evaluate the INMF solutions we compared the seafloor abundances against the U.S. Coastal Relief Model depth. Figure 5.8c shows the relationship between depth and INMF seafloor abundance. Below 40 meters, the seafloor abundance approaches a small value, as expected. In shallower regions, above 30 meters, there is no clear relationship between depth and INMF seafloor abundance. Considerable scatter occurs in the area around and over the Florida Keys, which can be seen as the bright band in the center of Figure 5.8a.

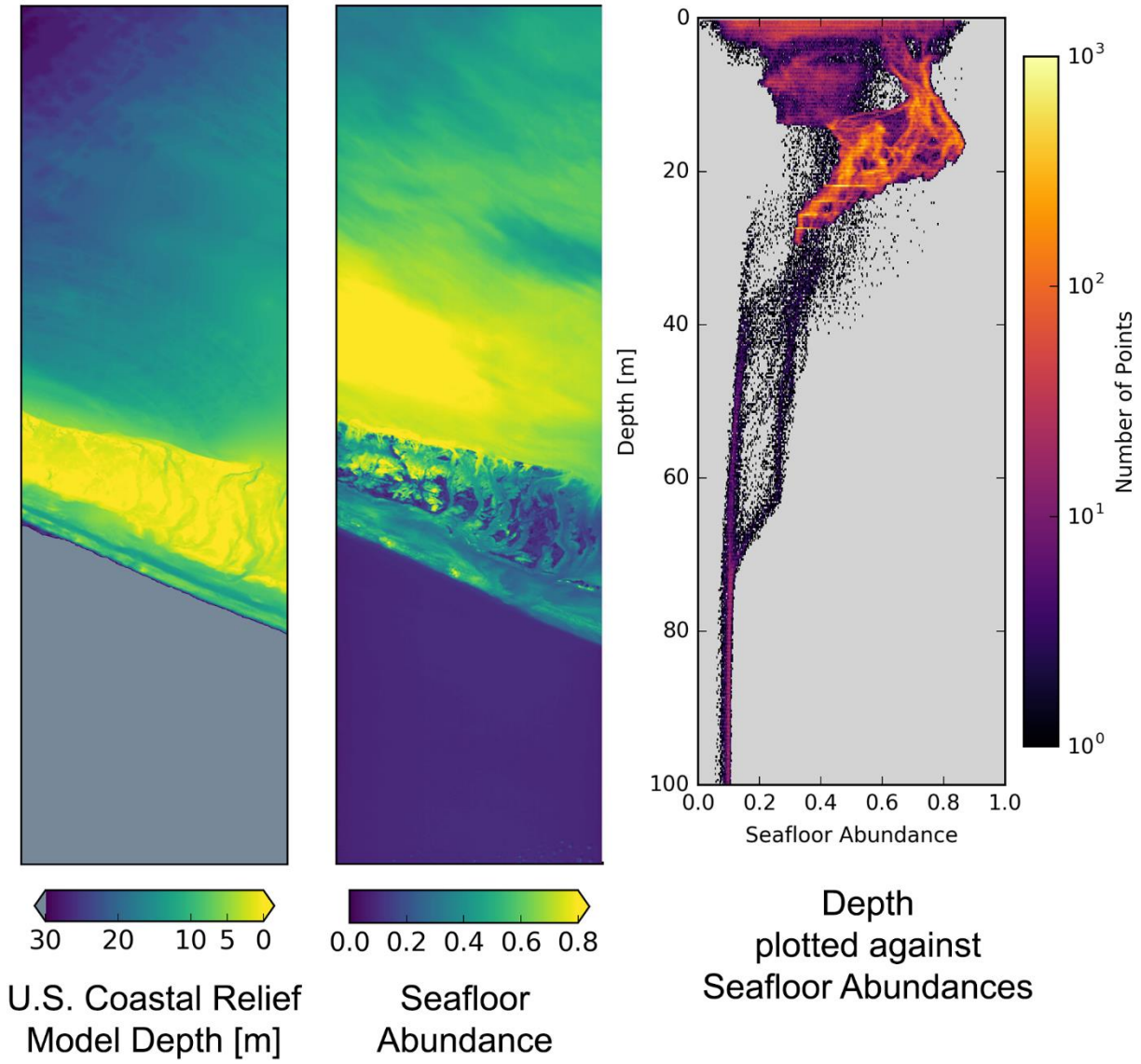

Figure 5.8: INMF seafloor abundance compared to the U.S. Coastal Relief Model.
(left) U.S. Coastal Relief Model seafloor depths for the HICO image. Depths greater than 30 meters are masked in gray. The lower portion of the image includes depths up to 1100 m. (center) INMF produced seafloor abundances. (right) Scatter plot of the U.S. Coastal Relief Model depths against the INMF seafloor abundances. The data are binned and each bin is colored by the number of points contained.

We cropped the image to the shallow region located above of the keys (Figure 5.1, left panel), and repeated the analysis. Figure 5.9 shows the relationship between bathymetric depth and INMF seafloor abundance for the cropped image. The seafloor abundance generally increased with decreasing depth, from 100 meters to a depth of about 15 meters. Shallower than 15 meters,

the seafloor abundance decreases as the depth decreases. At the same time, the INMF soil endmember abundance increases. The soil and seafloor endmembers have similar spectral shapes, although the soil spectrum is shifted to longer wavelengths (Figure 5.7).

To derive a predictive model of the relationship between depth and seafloor abundance, we fit a surface to the seafloor abundance, soil abundance, and depth data. The relationship between depth (D) and the seafloor abundance ($A_{seafloor}$) was assumed to be logarithmic due to the expected exponential relationship between transmitted radiance and path length. The relationship between depth and soil abundance (A_{soil}) was assumed to be linear. Given these assumptions the function: $D(A_{seafloor}, A_{soil}) = a + b \cdot \ln(A_{seafloor} - 0.0925) + c \cdot A_{soil}$, was fit to the data by minimizing the least-square error through varying the coefficients a, b, and c. The logarithmic offset, 0.0925 was found by taking the mean value of the seafloor abundance at depths below 100 meters.

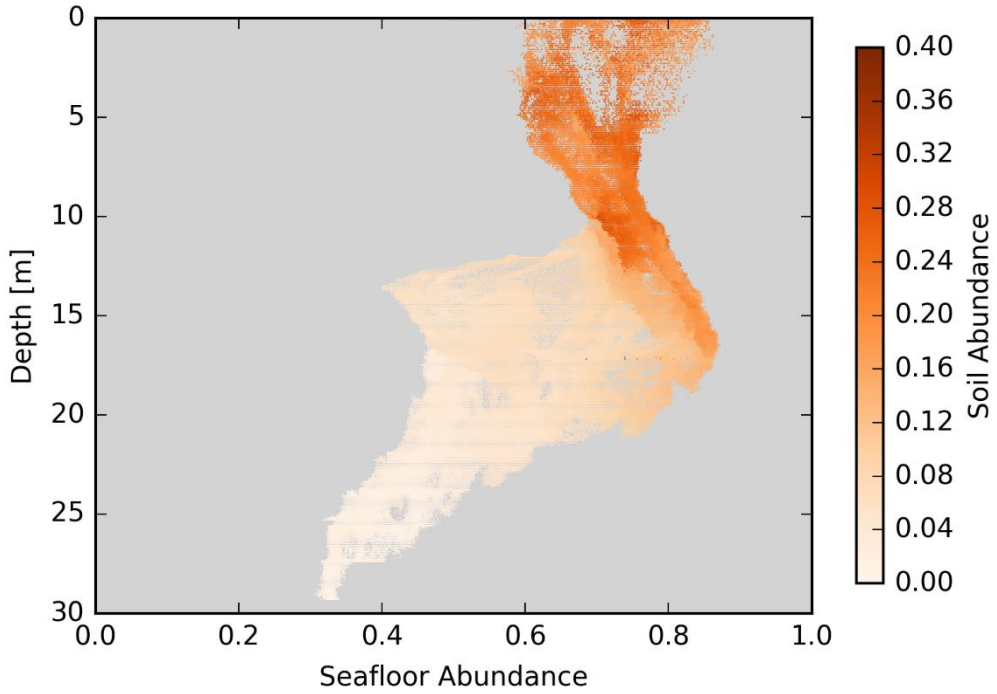

Figure 5.9: Scatter plot of seafloor abundance against depth.
Only the region to the north of the Florida Keys has been included. The Florida Strait and the Keys themselves have been excluded. The data points are colored by their soil abundance.

The resulting best fit equation was: $D = -18.68 + 3.70 \cdot \ln\left(A_{seafloor} - 0.0925\right) + 51.86 \cdot A_{soil}$. With this fit we achieve a mean absolute error of 2.33 meters, a mean absolute percentage error of 13.8%, a median absolute error of 2.10 meters, and a median absolute percentage error of 11.9%. Figure 5.10 shows the error between the depth calculated using the INMF derived value and the depth reported by the reference U.S. Coastal Relief Model.

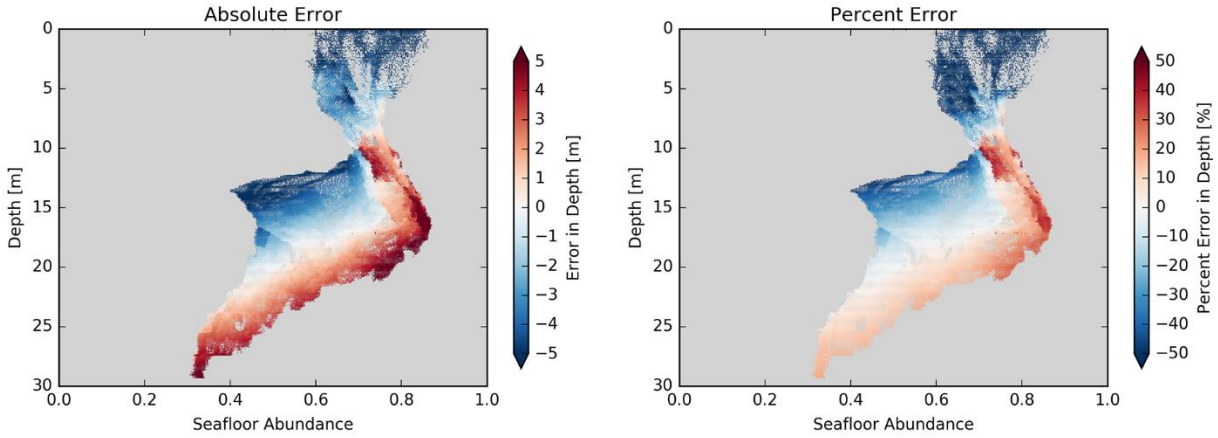

Figure 5.10: Differences between the INMF derived depth and the U.S. Coastal Relief Model. Absolute difference between the INMF derived depth values and the reference U.S. Coastal Relief Model depths (left). Relative difference between the derived depths and the reference depths (right)

The spectral shapes of the two endmembers suggest that the observed radiance spectra shift to longer wavelengths in shallower water resulting in the higher soil endmember abundance. This could be explained by water absorption increasing with wavelength (Figure 5.11). In shallow regions, more light in the 500-700 nm wavelength region, where the soil spectrum peaks (Figure 5.7), is scattered by the seafloor and travels through the water column without being absorbed. There are other possible explanations for the observed relationship between seafloor abundance, soil abundance, and water depth. For example, shallower regions may have more suspended sediment, plankton or other light-scattering particles that INMF attributed to the soil endmember.

Alternatively, the reflectance of the seafloor may have changed in shallow regions due to differences in composition or vegetation.

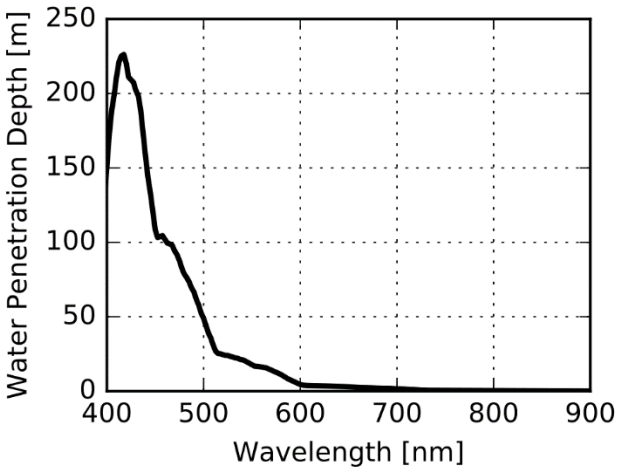

Figure 5.11: Liquid water penetration depth calculated for the HICO wavelength range. Absorption data are from Kou et al., 1993 and Pope & Fry, 1997.

5.8. Summary and Conclusions

Evaluation of the INMF aerosol attribution shows some promising results and some challenges. The spatial comparison against MODIS aerosol retrievals was encouraging. The INMF derived aerosol abundances were correlated (R = 0.972) with the MODIS retrieved 550 nm AOT. However, this high correlation was achieved only after masking certain sections of the image. However, in the absence of a ground truth measurement we have no way of attributing the low correlation to either the INMF results or the MODIS retrievals. Contributions from other oceanic sources proved particularly difficult. Removing regions of highly variable ocean color significantly improved the correlation in the Korean Peninsula image (Figure 5.4a and b), resulting in a correlation coefficient R of 0.87. In the Persian Gulf image another endmember was added to separate aerosol signal from highly reflective, shallow ocean regions. This approach was partially successful. The additional shallow water endmember had a high abundance in the shallow regions, but the aerosol abundance was also high. By excluding pixels where the shallow-water endmember

abundance was greater than 0.5 we removed regions where the aerosol signal was mixed with seafloor reflectance. The resulting data were better correlated (R = 0.583) with the MODIS data. Aggregating the results of the two images produced a strong correlation (R = 0.972), which suggests that the INMF aerosol abundance is appropriately identifying the spatial variations of the aerosol signal.

INMF derived aerosol spectra are not similar to the MODIS derived aerosol radiance spectra in either magnitude or spectral shape, despite the high spatial correlation between the INMF result and the MODIS retrieval. The closest results between the MODIS and INMF results had an RMS difference of 12.5 $W \cdot m^{-2} \cdot sr^{-1} \cdot nm^{-1}$, or 57.6%, with a SID of 0.135 for the Korean image and 4.03 $W \cdot m^{-2} \cdot sr^{-1} \cdot nm^{-1}$, or 33.1%, with a SID of 0.129 for the Persian Gulf image.

The poor correlation between the aerosol spectra and the MODIS derived spectrum suggests that the INMF aerosol endmember likely includes a mixture of contributions from other sources. Improving this performance would require better separation of aerosol from other sources. One approach to improving aerosol separation may be to add additional constraints to INMF. Adding constraints improved the separation between molecular scattering and surface signals (see Chapter 4) so it is likely that additional constraints can improve the separation of aerosol signals. Given these results we conclude that it is possible to derive aerosol optical thicknesses from the INMF attributed aerosol signals, but that future work should aim to improve aerosol separation.

Using INMF to retrieve bathymetry also revealed promising results and challenges. We were able to predict depth using a combination of seafloor abundance and soil abundance. Water depth calculated with this relationship had a mean absolute error of 2.33 meters and a mean relative error of 13.8%. The method appears to produce more accurate depth estimates in deeper water, while both relative and absolute error increase in water shallower than 10 meters. It could be that

the absorption spectrum in deeper water is most similar to the seafloor initial spectrum guess, but shifts towards longer wavelengths in shallower water. Another explanation is that shallow regions are more likely to have contributions from sources other than the seafloor bottom or water, such as suspended sediments or vegetation.

Further work to improve water depth retrievals with INMF should optimize the algorithmic constraints and the initial guess of the seafloor spectrum. Additionally, there are other approaches to hyperspectral retrievals of bathymetry. INMF should be compared to these. Finally, in this work only a single image was examined. This method needs to be more broadly tested by examining its performance in different shallow regions.

Chapter 6

Summary and Directions for Future Work

This chapter, summarizes results of the work presented in this thesis and suggest directions for future work. The work described focused on developing tools and applications that effectively manage data collected by hyperspectral instruments. Considering the growing number of operational and planned hyperspectral instruments, this work provides timely information on how to make use of the additional spectral data collected beyond previous generation multispectral instruments.

6.1. Instrument Development and Atmospheric Correction

Chapter 2 describes the characterization, validation and calibration of the Solar Spectral Irradiance Monitor (SSIM) that was built for National Ecological Observatory Network (NEON) and flown on their Twin Otter aircraft. Substantial improvements were made to the SSIM over previous generations of the instrument (Pilewskie et al., 2003). An active stabilizing system, or leveling platform, was introduced to the zenith-viewing optics. This system was designed to keep the optics level with the Earth horizon for aircraft motion of up to ±7° in pitch or roll (Figure 2.4). This system was flight tested and it performance validated through a series of engineering test flights in June 2015. The optics themselves underwent a redesign to remove substantial azimuthal dependencies. The revised optical design removed the four-lobed pattern from the response

function and reduced the magnitude of azimuthal variations in response from ±5% to less than 1% (Figure 2.6). A thermal control system was implemented to enclose the spectrometers. Testing in a thermal chamber demonstrated that this system dampened the spectrometer temperature fluctuations by 84%, which reduced an environmental temperature change of 10ºC to a change in spectrometer temperatures of 1.6ºC (Figure 2.7). This chapter also presented an overview of the spectral and radiometric calibration methods for the SSIM.

In Chapter 3 we demonstrated the use of airborne irradiance measurements made by the SSIM to atmospherically correct hyperspectral imagery below clouds. This work was a collaboration with NEON and compared surface reflectance data retrieved from NEON's imaging spectrometer against ground reflectance spectra measured over a bright and dark reflectance target, a dirt road, and a vegetated surface. Below cloud layers the retrieval using SSIM irradiance data was up to 58% more accurate than standard retrieval methods (Figure 3.11). We also demonstrated the possibility of using an upwelling irradiance measurement to estimate the adjacency effect. However, the result of this adjacency correction showed only that the approach was more accurate than no correction. Further research is needed to compare this method to other widely used adjacency correction methods, such as defining an adjacency range, before concluding whether a hemispheric observation like the SSIM upwelling irradiance measure is appropriate for adjacency correction.

Below-cloud atmospheric correction is an important challenge for airborne remote sensing. The challenge of retrieving accurate surface reflectances from data collected below clouds is faced by all airborne remote sensing platforms and increases the length, and therefore expense of deployments if an aircraft is unable to collect the required data. The work presented in Chapter 3 presents a solution, although there are several additional steps required for these results to be

widely implemented. The atmospheric correction routines tested were very basic algorithms. A more advanced method could be developed by incorporating methods that are already used in currently available commercial routines such as pixel-by-pixel water vapor corrections, retrievals of aerosol optical thickness from the imagery itself, and topographic corrections. Lastly, one of the most obvious drawbacks of the current implementation is the increase in channel-to-channel variation evident in the retrieved data product. To avoid this problem in an operational observing system the irradiance spectrometers and hyperspectral imagers should be made with spectrometers with the same slit functions or one instrument should over-sample the other.

6.2. Informed Non-Negative Matrix Factorization Algorithm and Retrievals

The remaining two chapters discuss the development of the Informed Non-Negative Matrix Factorization (INMF) spectral unmixing routine. Chapter 4 describes the development and testing of the INMF algorithm. INMF includes both cost function and algorithmic constraints in order to incorporate the physics of radiative transfer and remote sensing. These constraints guide the algorithm towards a physically plausible identification of component signals, and reduce mixing between physically distinct sources in the INMF solution. To test the method two images taken by the Hyperspectral Imager for the Coastal Ocean (HICO) were processed with INMF using several different subset scenes from within the image and different number of endmembers. One image was centered on the Hawaiian Islands, the other on the Florida Keys. To validate the solutions, the INMF decomposition of dark, deep ocean portions of each image were compared against model-based atmospheric correction partitioning of the observed signal (Figure 4.9 and Figure 4.10). The best comparison between INMF and the model-based atmospheric correction was achieved for scenes with the highest spatial variability. In the best-case-scenario, the relative RMS difference

between the two methods was 3.4% for the signal attributed to atmospheric scattering and 24.9% for signal attributed to surface water.

We also investigated the sensitivity of the INMF algorithm to variations in the magnitude of the initial guess spectra (Figure 4.12). The results demonstrated that perturbations as large as 30% from the best initial guess did not produce divergent solutions for endmember shapes and magnitudes. This test also showed that increasing the number of iterations for the perturbed ensemble led to further convergence of the ensemble members as demonstrated by decreasing ensemble standard deviation. For atmospheric scattering the ensemble standard deviation decreased to less than 10% of the initial value, and continued to decrease with further iteration (Figure 4.12, top right).

The results from this study suggest a number of new avenues to be explored. For example, a new study could examine the effect of perturbing not only initial guess magnitudes but also their spectral shapes. This work did not attempt to determine the sensitivity to several of the INMF constraint parameters that were adopted from previous studies (Jia & Qian, 2009). Finally, only two HICO images were examined; before generalizing results more images should be examined.

Chapter 5 presents two (out of many possible) retrievals, aerosol optical thickness and seafloor depth, using the INMF solution. This work focused on demonstrating whether INMF results could be used to derive properties relevant to atmospheric and oceanic science, aerosol optical thickness and seafloor depth, respectively. For aerosol optical thickness (AOT) the INMF solution was compared spatially and spectrally against aerosol properties retrieved from the Moderate Resolution Imaging Spectroradiometer (MODIS) observations. Spatially, the INMF-derived aerosol abundances correlate strongly with the MODIS AOT values (Figure 5.5). However, the INMF attributed aerosol spectrum does not compare well in shape or magnitude to

the MODIS derived spectrum (Figure 5.6) because other endmembers are mixed onto the aerosol endmember. The poorest comparison against MODIS was produced over shallow regions with contributions from the seafloor, or oceans with high turbidity, where MODIS-retrieved aerosol properties would also have high uncertainty. Over darker ocean the INMF results match the MODIS values more closely.

Our results show that adding an additional aerosol endmember is insufficient to fully unmix the aerosol signal. A better approach may be to add tighter constraints to the INMF algorithm. More work is needed to determine what form these constraints should take. Additionally, the scenes covered fairly small ranges of aerosol optical thicknesses. Generalizing these INMF results will require processing and validating significantly more images over a wider range of atmospheric conditions.

The bathymetry, or seafloor depth, retrieval from the INMF results was derived by comparing the abundance of the seafloor endmember against reference depth measurements produced by the U.S. Coastal Relief Model (NOAA National Centers for Environmental Information, 2001). We examined a single HICO scene over a large shallow region to the north of the Florida Keys. The seafloor endmember spectrum resembles the spectrum of penetration depth of liquid water (Figure 5.7 and Figure 5.11). It is clear that both the soil and seafloor endmembers were related to depth. We derived a predictive equation for the relationship between seafloor abundance, soil abundance and depth (Figure 5.9 and Figure 5.10). The derived relationship resulted in a mean absolute error of 2.33 meter or 13.8%.

A next step would be to examine if this relationship correctly predicts depth in other images on this same location near the Florida Keys. The end goal is to generalize a relationship between

derived seafloor abundance and the depth of any shallow body of water. This requires selecting and processing many more images than the single one examined here.

6.3. Conclusion

The remote sensing community has capitalized on the benefits that hyperspectral measurements afford. However, there are many areas where the data analysis and resulting science has not been able to take advantage of the full range information content is this data. This is most often evident where data processing methods treat hyperspectral data as a collection of wavelength channels similar to multispectral data processing, for example, by replicating multispectral techniques such as band ratios. Hyperspectral data affords many more opportunities for data analysis because channels are more numerous, continuous, and contiguous over their entire spectral range. This thesis addresses some of those challenges by presenting new ways to approach hyperspectral data, including new combinations of multiple instruments (Chapter 2 and Chapter 3) and developing an algorithm to unmix top-of-atmosphere radiance observations (Chapter 4 and Chapter 5). As new instruments and their measurements improve in spectral coverage and resolution and radiometric accuracy these methods will become increasingly important for exploiting the information dense data to its full potential.

References

Adler-Golden, S. M., Acharya, P. K., Berk, A., Matthew, M. W., & Gorodetzky, D. (2005). Remote bathymetry of the littoral zone from AVIRIS, LASH, and QuickBird imagery. *IEEE Transactions on Geoscience and Remote Sensing*, *43*(2), 337–347. https://doi.org/10.1109/TGRS.2004.841246

Ahmad, Z., Franz, B. A., McClain, C. R., Kwiatkowska, E. J., Werdell, J., Shettle, E. P., & Holben, B. N. (2010). New aerosol models for the retrieval of aerosol optical thickness and normalized water-leaving radiances from the SeaWiFS and MODIS sensors over coastal regions and open oceans. *Applied Optics*, *49*(29), 5545. https://doi.org/10.1364/AO.49.005545

Anderson, G. D. (2010). The first weather satellite picture. *Weather*, *65*(4), 87–87. https://doi.org/10.1002/wea.550

Ardanuy, P. E., Han, D., & Salomonson, V. V. (1991). The moderate resolution imaging spectrometer (MODIS) science and data system requirements. *IEEE Transactions on Geoscience and Remote Sensing*, *29*(1), 75–88. https://doi.org/10.1109/36.103295

Baldridge, A. M., Hook, S. J., Grove, C. I., & Rivera, G. (2009). The ASTER spectral library version 2.0. *Remote Sensing of Environment*, *113*(4), 711–715. https://doi.org/10.1016/j.rse.2008.11.007

Barnes, W. L., Pagano, T. S., & Salomonson, V. V. (1998). Prelaunch characteristics of the Moderate Resolution Imaging Spectroradiometer (MODIS) on EOS-AM1. *IEEE Transactions on Geoscience and Remote Sensing*, *36*(4), 1088–1100. https://doi.org/10.1109/36.700993

Baugh, W. M., & Groeneveld, D. P. (2008). Empirical proof of the empirical line. *International Journal of Remote Sensing*, *29*(3), 665–672. https://doi.org/10.1080/01431160701352162

Berk, A., Anderson, G. P., & Acharya, P. K. (2013). *MODTRAN 5.3.2 User's Manual*.

Berk, A., & Anderson, G. P. (2008). Impact of MODTRAN 5.1 on Atmospheric Compensation. *International Geoscience and Remote Sensing Symposium (IGARSS)*, 127–129.

Berk, A., Anderson, G. P., Acharya, P. K., Bernstein, L. S., Muratov, L., Lee, J., … Shettle, E. P. (2006). MODTRAN5: 2006 update. In S. S. Shen & P. E. Lewis (Eds.) (Vol. 6233, p. 62331F). https://doi.org/10.1117/12.665077

Berry, M. W., Browne, M., Langville, A. N., Pauca, V. P., & Plemmons, R. J. (2007). Algorithms and applications for approximate nonnegative matrix factorization. *Computational Statistics & Data Analysis*, *52*(1), 155–173. https://doi.org/10.1016/j.csda.2006.11.006

Bioucas-Dias, J. M., Plaza, A., Dobigeon, N., Parente, M., Du, Q., Gader, P., & Chanussot, J. (2012). Hyperspectral Unmixing Overview: Geometrical, Statistical, and Sparse Regression-Based Approaches. *IEEE Journal of Selected Topics in Applied Earth Observations and Remote Sensing*, *5*(2), 354–379. https://doi.org/10.1109/JSTARS.2012.2194696

Boardman, J. W., Kruse, F. A., & Green, R. O. (1995). Mapping Target Signatures Via Partial Unmixing Of AVIRIS Data. In *Summaries of JPL Airborne Earth Science Workshop*. Pasadena, CA.

Bodhaine, B. A., Wood, N. B., Dutton, E. G., & Slusser, J. R. (1999). On Rayleigh Optical Depth Calculations. *Journal of Atmospheric and Oceanic Technology*, *16*(11), 1854–1861. https://doi.org/10.1175/1520-0426(1999)016<1854:ORODC>2.0.CO;2

Bohren, C. F., & Clothiaux, E. E. (2006). *Fundamentals of Atmospheric Radiation*. Wiley-VCH.

Bovensmann, H., Burrows, J. P., Buchwitz, M., Frerick, J., Noël, S., Rozanov, V. V., … Goede, A. P. H. (1999). SCIAMACHY: Mission Objectives and Measurement Modes. *Journal of the Atmospheric Sciences*, *56*(2), 127–150. https://doi.org/10.1175/1520-0469(1999)056<0127:SMOAMM>2.0.CO;2

Bowker, D. E., Davis, R. E., Myrick, D. L., Stacy, K., & Jones, W. T. (1985). *Spectral reflectances of natural targets for use in remote sensing studies*. *NASA reference publication 1139*. Retrieved from https://ntrs.nasa.gov/archive/nasa/casi.ntrs.nasa.gov/19850022138.pdf

Brown, S. W., Flora, S. J., Feinholz, M. E., Yarbrough, M. A., Houlihan, T., Peters, D., … Clark, D. K. (2007). The marine optical buoy (MOBY) radiometric calibration and uncertainty budget for ocean color satellite sensor vicarious calibration. In R. Meynart, S. P. Neeck, H. Shimoda, & S. Habib (Eds.) (p. 67441M). https://doi.org/10.1117/12.737400

Bucholtz, A., Bluth, R. T., Kelly, B., Taylor, S., Batson, K., Sarto, A. W., … McCoy, R. F. (2008). The Stabilized Radiometer Platform (STRAP) - An actively stabilized horizontally level platform for improved aircraft irradiance measurements. *Journal of Atmospheric and Oceanic Technology*, *25*(12), 2161–2175. https://doi.org/10.1175/2008JTECHA1085.1

Burrows, J. P., Weber, M., Buchwitz, M., Rozanov, V., Ladstätter-Weißenmayer, A., Richter, A., … Perner, D. (1999). The Global Ozone Monitoring Experiment (GOME): Mission Concept and First Scientific Results. *Journal of the Atmospheric Sciences*, *56*(2), 151–175. https://doi.org/10.1175/1520-0469(1999)056<0151:TGOMEG>2.0.CO;2

Callies, J., Corpaccioli, E., Eisinger, M., Hahne, A., & Lefebvre, A. (2000). GOME-2 - Metop's second-generation sensor for operational ozone monitoring. *ESA Bulletin-European Space Agency*, *102*(may), 28–36.

Calsbeek, N., Eakins, B. W., & Love, M. (2013). *Revised Coastal Relief Model of Southern California: Procedures, Data Sources and Analysis*. NOAA National Geophysical Data Center, Boulder, Colorado.

Chang, C.-I. (2000). An information-theoretic approach to spectral variability, similarity, and discrimination for hyperspectral image analysis. *IEEE Transactions on Information Theory*, *46*(5), 1927–1932. https://doi.org/10.1109/18.857802

Chiang, S.-S., Chang, C.-I., & Ginsberg, I. W. (2000). Unsupervised hyperspectral image analysis using independent component analysis. In *IGARSS 2000. IEEE 2000 International Geoscience and Remote Sensing Symposium. Taking the Pulse of the Planet: The Role of Remote Sensing in Managing the Environment. Proceedings (Cat. No.00CH37120)* (Vol. 7, pp. 3136–3138). IEEE. https://doi.org/10.1109/IGARSS.2000.860361

Clark, D. K., Gordon, H. R., Voss, K. J., Ge, Y., Broenkow, W., & Trees, C. (1997). Validation of atmospheric correction over the oceans. *Journal of Geophysical Research: Atmospheres*, *102*(D14), 17209–17217. https://doi.org/10.1029/96JD03345

Coddington, O., Pilewskie, P., & Vukicevic, T. (2012). The Shannon information content of hyperspectral shortwave cloud albedo measurements: Quantification and practical applications. *Journal of Geophysical Research: Atmospheres*, *117*(D4). https://doi.org/10.1029/2011JD016771

Comon, P. (1994). Independent component analysis, A new concept? *Signal Processing*, *36*(3), 287–314. https://doi.org/10.1016/0165-1684(94)90029-9

Cooper, S. J., L'Ecuyer, T. S., Gabriel, P., Baran, A. J., & Stephens, G. L. (2006). Objective Assessment of the Information Content of Visible and Infrared Radiance Measurements for Cloud Microphysical Property Retrievals over the Global Oceans. Part II: Ice Clouds. *Journal of Applied Meteorology and Climatology*, *45*(1), 42–62. https://doi.org/10.1175/JAM2327.1

Corson, M., Lucke, R. L., & Davis, C. O. (2010). The Hyperspectral Imager for the Coastal Ocean (HICO) and Environmental Characterization of the Coastal Zone from the International Space Station. In *Imaging and Applied Optics Congress* (p. OMA4). Washington, D.C.: OSA. https://doi.org/10.1364/ORSE.2010.OMA4

Corson, M. R., Korwan, D. R., Lucke, R. L., Snyder, W. A., & Davis, C. O. (2008). The Hyperspectral Imager for the Coastal Ocean (HICO) on the International Space Station. In *IGARSS 2008 - 2008 IEEE International Geoscience and Remote Sensing Symposium* (Vol. 4, p. IV-101-IV-104). IEEE. https://doi.org/10.1109/IGARSS.2008.4779666

Corson, M. R., Lucke, R. L., Davis, C. O., Bowles, J. H., Chen, D. T., Gao, B.-C., … Snyder, W. A. (2010). The Hyperspectral Imager for the Coastal Ocean (HICO) environmental littoral imaging from the International Space Station. In *2010 IEEE International Geoscience and Remote Sensing Symposium* (pp. 3752–3755). IEEE. https://doi.org/10.1109/IGARSS.2010.5651830

Crowley, J. K., Brickey, D. W., & Rowan, L. C. (1989). Airborne imaging spectrometer data of the Ruby Mountains, Montana: Mineral discrimination using relative absorption band-depth images. *Remote Sensing of Environment*, *29*(2), 121–134. https://doi.org/10.1016/0034-4257(89)90021-7

Davis, C., Carder, K., Gao, B.-C., Lee, Z.-P., & Bissett, W. P. (2006). The Development of Imaging Spectrometry of the Coastal Ocean. In *2006 IEEE International Symposium on Geoscience and Remote Sensing* (pp. 1982–1985). IEEE. https://doi.org/10.1109/IGARSS.2006.513

Davis, C. O., Kavanaugh, M., Letelier, R., Bissett, W. P., & Kohler, D. (2007). Spatial and spectral resolution considerations for imaging coastal waters. In R. J. Frouin (Ed.), *Proceedings of SPIE* (Vol. 6680, p. 66800P). https://doi.org/10.1117/12.734288

Feldman, D. R., Algieri, C. A., Collins, W. D., Roberts, Y. L., & Pilewskie, P. A. (2011). Simulation studies for the detection of changes in broadband albedo and shortwave nadir reflectance spectra under a climate change scenario. *Journal of Geophysical Research: Atmospheres*, *116*(D24). https://doi.org/10.1029/2011JD016407

Gao, B.-C., Heidebrecht, K. B., & Goetz, A. F. H. (1993). Derivation of scaled surface reflectances from AVIRIS data. *Remote Sensing of Environment*, *44*(2–3), 165–178. https://doi.org/10.1016/0034-4257(93)90014-O

Gao, B.-C., Davis, C., & Goetz, A. F. H. (2006). A Review of Atmospheric Correction Techniques for Hyperspectral Remote Sensing of Land Surfaces and Ocean Color. In *2006 IEEE International Symposium on Geoscience and Remote Sensing* (pp. 1979–1981). IEEE. https://doi.org/10.1109/IGARSS.2006.512

Gao, B.-C., Montes, M. J., Davis, C. O., & Goetz, A. F. H. (2009). Atmospheric correction algorithms for hyperspectral remote sensing data of land and ocean. *Remote Sensing of Environment*, *113*, S17–S24. https://doi.org/10.1016/j.rse.2007.12.015

Goetz, A. F. H. (2009). Three decades of hyperspectral remote sensing of the Earth: A personal

view. *Remote Sensing of Environment*, *113*, S5–S16. https://doi.org/10.1016/j.rse.2007.12.014

Goetz, A. F. H., Heidebrecht, K. B., Kindel, B. C., & Boardman, J. W. (1998). Using Ground Spectral Irradiance for Model Correction of AVIRIS Data. In *Summaries of the Seventh JPL Airborne Earth Science Workshop* (pp. 159–168).

Goetz, A. F. H., Billingsley, F. C., Gillespie, A. R., Abrams, M. J., Squires, R. L., Shoemaker, E. M., … Elston, D. P. (1975). *Application of ERTS Images and Image Processing to Regional Geological Problems and Geological Problems in Northern Arizona.*

Goetz, A. F. H., Boardman, J. W., Kindel, B. C., & Heidebrecht, K. B. (1997). Atmospheric corrections: on deriving surface reflectance from hyperspectral imagers. In M. R. Descour & S. S. Shen (Eds.), *Proceedings of SPIE, 3118, Imaging Spectrometry III* (Vol. 3118, pp. 14–22). https://doi.org/10.1117/12.283831

Goetz, A. F. H., Vane, G., Solomon, J. E., & Rock, B. N. (1985). Imaging Spectrometry for Earth Remote Sensing. *Science*, *228*(4704), 1147–1153. https://doi.org/10.1126/science.228.4704.1147

Gordon, H. R., & Wang, M. (1994). Retrieval of water-leaving radiance and aerosol optical thickness over the oceans with SeaWiFS: a preliminary algorithm. *Applied Optics*, *33*(3), 443. https://doi.org/10.1364/AO.33.000443

Green, R. O., Eastwood, M. L., Sarture, C. M., Chrien, T. G., Aronsson, M., Chippendale, B. J., … Williams, O. (1998). Imaging Spectroscopy and the Airborne Visible/Infrared Imaging Spectrometer (AVIRIS). *Remote Sensing of Environment*, *65*(3), 227–248. https://doi.org/10.1016/S0034-4257(98)00064-9

Grothe, P. ., Taylor, L. A., Eakins, B. W., Carignan, K. S., Friday, D. Z., Lim, E., & Love, M. (2011). *Digital Elevation Models of Key West, Florida: Procedures, Data Sources and Analysis*. NOAA National Geophysical Data Center, Boulder, Colorado.

Guanter, L., Kaufmann, H., Segl, K., Foerster, S., Rogass, C., Chabrillat, S., … Sang, B. (2015). The EnMAP Spaceborne Imaging Spectroscopy Mission for Earth Observation. *Remote Sensing*, *7*(7), 8830–8857. https://doi.org/10.3390/rs70708830

Hamlin, L., Green, R. O., Mouroulis, P., Eastwood, M., Wilson, D., Dudik, M., & Paine, C. (2011). Imaging spectrometer science measurements for Terrestrial Ecology: AVIRIS and new developments. In *2011 Aerospace Conference* (pp. 1–7). IEEE. https://doi.org/10.1109/AERO.2011.5747395

Harrison, L., Michalsky, J., & Berndt, J. (1994). Automated multifilter rotating shadow-band radiometer: an instrument for optical depth and radiation measurements. *Applied Optics*, *33*(22), 5118–5125. https://doi.org/10.1364/AO.33.005118

Heinz, D. C., & Chang, C.-I. (2001). Fully constrained least squares linear spectral mixture analysis method for material quantification in hyperspectral imagery. *IEEE Transactions on Geoscience and Remote Sensing*, *39*(3), 529–545. https://doi.org/10.1109/36.911111

Homer, C. G., Dewitz, J., Yang, L., Jin, S., Danielson, P., Xian, G. Z., … Megown, K. (2015). Completion of the 2011 National Land Cover Database for the conterminous United States – Representing a decade of land cover change information. *Photogrammetric Engineering and Remote Sensing*, *81*, 345–354.

Homolova, L., Alanko-Huotari, K., & Scheapman, M. E. (2009). Sensitivity of the ground-based

downwelling irradiance recorded by the FODIS sensor in respect of different angular positions. In *2009 First Workshop on Hyperspectral Image and Signal Processing: Evolution in Remote Sensing* (pp. 1–4). IEEE. https://doi.org/10.1109/WHISPERS.2009.5289084

Hunt, G. R. (1977). Spectral Signatures Of Particulate Minerals In The Visible And Near Infrared. *GEOPHYSICS*, *42*(3), 501–513. https://doi.org/10.1190/1.1440721

Ibrahim, A., Franz, B., Ahmad, Z., Healy, R., Knobelspiesse, K., Gao, B.-C., … Zhai, P.-W. (2018). Atmospheric correction for hyperspectral ocean color retrieval with application to the Hyperspectral Imager for the Coastal Ocean (HICO). *Remote Sensing of Environment*, *204*, 60–75. https://doi.org/10.1016/J.RSE.2017.10.041

Jia, S., & Qian, Y. (2009). Constrained Nonnegative Matrix Factorization for Hyperspectral Unmixing. *IEEE Transactions on Geoscience and Remote Sensing*, *47*(1), 161–173. https://doi.org/10.1109/TGRS.2008.2002882

Johnson, B. R., Kampe, T. U., & Kuester, M. (2010). Development of airborne remote sensing instrumentations for NEON. In W. Gao, T. J. Jackson, & J. Wang (Eds.), *Remote Sensing and Modeling of Ecosystems for Sustainability VII* (Vol. 7809, p. 78090I). https://doi.org/10.1117/12.860182

Jolliffe, I. T. (2002). *Principal Component Analysis*. New York: Springer.

Justice, C. O., Vermote, E. F., Townshend, J. R. G., Defries, R., Roy, D. P., Hall, D. K., … Barnsley, M. J. (1998). The Moderate Resolution Imaging Spectroradiometer (MODIS): Land Remote Sensing for Global Change Research. *Geoscience and Remote Sensing, IEEE Transactions on*, *36*(4), 1228–1249. https://doi.org/10.1109/36.701075

Kampe, T. U., Johnson, B. R., Kuester, M., & Keller, M. (2010). NEON: the first continental-scale ecological observatory with airborne remote sensing of vegetation canopy biochemistry and structure. *Journal of Applied Remote Sensing*, *4*(1), 43510. https://doi.org/10.1117/1.3361375

Kampe, T. U., Asner, G. P., Green, R. O., Eastwood, M., Johnson, B. R., & Kuester, M. (2010). Advances in airborne remote sensing of ecosystem processes and properties: toward high-quality measurement on a global scale. In W. Gao, T. J. Jackson, & J. Wang (Eds.), *Proceedings of SPIE* (Vol. 7809, p. 78090J). https://doi.org/10.1117/12.859455

Kampe, T. U., Johnson, B. R., Kuester, M., & McCorkel, J. (2010). The NEON Imaging Spectrometer: Airborne Measurements of Vegetation Cover and Biochemistry for the Continental-scale NEON Observatory. *IEEE-GRSS Proc. of Art, Science …*, 1–6.

Kampe, T. U., Leisso, N., Musinsky, J., Petroy, S., Karpowicz, B., Krause, K., … Serbin, S. (2013). *TM-005: The NEON 2013 Airborne Campaign at Domain 17 Terrestrial and Aquatic Sites in California*. Boulder, Colorado.

Keshava, N. (2003). A survey of spectral unmixing algorithms. *Lincoln Laboratory Journal*, *14*(1), 55–78.

Keshava, N., & Mustard, J. F. (2002). Spectral unmixing. *IEEE Signal Processing Magazine*, *19*(1), 44–57. https://doi.org/10.1109/79.974727

Kindel, B. C., Schmidt, K. S., Pilewskie, P., Baum, B. A., Yang, P., & Platnick, S. (2010). Observations and modeling of ice cloud shortwave spectral albedo during the Tropical Composition, Cloud and Climate Coupling Experiment (TC 4). *Journal of Geophysical Research*, *115*(17), D00J18. https://doi.org/10.1029/2009JD013127

Kou, L., Labrie, D., & Chylek, P. (1993). Refractive indices of water and ice in the 065- to 25-μm spectral range. *Applied Optics*, *32*(19), 3531. https://doi.org/10.1364/AO.32.003531

Krause, E. F. (1986). *Taxicab Geometry: An Adventure in Non-Euclidean Geometry*. New York: Dover Publications Inc.

Kruse, F. A. (2004). Comparison of ATREM, ACRON, and FLAASH Atmospheric Corrections Using Low-Altitude AVIRIS Data of Boulder, CO. In *Summaries of 13th JPL Airborne Geoscience Workshop*. Padadena, CA.

L'Ecuyer, T. S., Gabriel, P., Leesman, K., Cooper, S. J., & Stephens, G. L. (2006). Objective Assessment of the Information Content of Visible and Infrared Radiance Measurements for Cloud Microphysical Property Retrievals over the Global Oceans. Part I: Liquid Clouds. *Journal of Applied Meteorology and Climatology*, *45*(1), 20–41. https://doi.org/10.1175/JAM2326.1

Lee, C. M., Cable, M. L., Hook, S. J., Green, R. O., Ustin, S. L., Mandl, D. J., & Middleton, E. M. (2015). An introduction to the NASA Hyperspectral InfraRed Imager (HyspIRI) mission and preparatory activities. *Remote Sensing of Environment*, *167*, 6–19. https://doi.org/10.1016/j.rse.2015.06.012

Lee, D. D., & Seung, H. S. (1999). Learning the parts of objects by non-negative matrix factorization. *Nature*, *401*(6755), 788–791. https://doi.org/10.1038/44565

Lee, D. D., & Seung, H. S. (2001). Algorithms for Non-negative Matrix Factorization. In T. K. Leen, T. G. Dietterich, & V. Tresp (Eds.), *Advances in Neural Information Processing Systems 13* (pp. 556–562). MIT Press.

Levelt, P. F., van den Oord, G. H. J., Dobber, M. R., Malkki, A., Huib Visser, Johan de Vries, … Saari, H. (2006). The ozone monitoring instrument. *IEEE Transactions on Geoscience and Remote Sensing*, *44*(5), 1093–1101. https://doi.org/10.1109/TGRS.2006.872333

Levy, R. C., Mattoo, S., Munchak, L. A., Remer, L. A., Sayer, A. M., Patadia, F., & Hsu, N. C. (2013). The Collection 6 MODIS aerosol products over land and ocean. *Atmospheric Measurement Techniques*, *6*(11), 2989–3034. https://doi.org/10.5194/amt-6-2989-2013

Lucke, R. L., Corson, M., McGlothlin, N. R., Butcher, S. D., Wood, D. L., Korwan, D. R., … Chen, D. T. (2011). Hyperspectral Imager for the Coastal Ocean: instrument description and first images. *Applied Optics*, *50*(11), 1501. https://doi.org/10.1364/AO.50.001501

Matthew, M. W., Adler-Golden, S. M., Berk, A., Felde, G., Anderson, G. P., Gorodetzky, D., … Shippert, M. (2002). Atmospheric correction of spectral imagery: evaluation of the FLAASH algorithm with AVIRIS data. In *Applied Imagery Pattern Recognition Workshop, 2002. Proceedings.* (pp. 157–163). IEEE Comput. Soc. https://doi.org/10.1109/AIPR.2002.1182270

Mobley, C. D., Werdell, J., Franz, B., Ahmad, Z., & Bailey, S. W. (2016). Atmospheric Correction for Satellite Ocean Color Radiometry. *A Tutorial and Documentation NASA Ocean Biology Processing Group*, (June), 1–73.

NASA Goddard Space Flight Center. (1971). *NASA Earth Resources Technology Satellite - Data user's handbook*.

NASA Goddard Space Flight Center. (2017). PACE: Plankton, Aerosol, Cloud, ocean Ecosystem. Retrieved January 1, 2017, from https://pace.gsfc.nasa.gov/

NASA Goddard Space Flight Center Ocean Biology Processing Group. (2017). SeaWiFS Data Analysis System (SeaDAS). Retrieved June 1, 2017, from https://seadas.gsfc.nasa.gov/

NASA Goddard Space Flight Center Ocean Ecology Laboratory Ocean Biology Processing Group. (2017). Hyperspectral Imager for the Coastal Ocean (HICO^{TM}) Data. https://doi.org/10.5067/ISS/HICO/L1/DATA/1

Nascimento, J. M. P., & Dias, J. M. B. (2005). Vertex component analysis: a fast algorithm to unmix hyperspectral data. *IEEE Transactions on Geoscience and Remote Sensing*, *43*(4), 898–910. https://doi.org/10.1109/TGRS.2005.844293

NOAA National Centers for Environmental Information. (2001). U.S. Coastal Relief Model. https://doi.org/10.7289/V5W66HPP

Oregon State University. (2015). Hyperspectral Imager for the Coastal Ocean. Retrieved October 8, 2017, from http://hico.coas.oregonstate.edu/

Painter, T. H., Berisford, D. F., Boardman, J. W., Bormann, K. J., Deems, J. S., Gehrke, F., … Winstral, A. (2016). The Airborne Snow Observatory: Fusion of scanning lidar, imaging spectrometer, and physically-based modeling for mapping snow water equivalent and snow albedo. *Remote Sensing of Environment*, *184*, 139–152. https://doi.org/10.1016/j.rse.2016.06.018

Pauca, V. P., Piper, J., & Plemmons, R. J. (2006). Nonnegative matrix factorization for spectral data analysis. *Linear Algebra and Its Applications*, *416*(1), 29–47. https://doi.org/10.1016/j.laa.2005.06.025

Pearlman, J. S., Barry, P. S., Segal, C. C., Shepanski, J., Beiso, D., & Carman, S. L. (2003). Hyperion, a space-based imaging spectrometer. *IEEE Transactions on Geoscience and Remote Sensing*, *41*(6), 1160–1173. https://doi.org/10.1109/TGRS.2003.815018

Pilewskie, P., Pommier, J., Bergstrom, R. W., Gore, W., Howard, S., Rabbette, M., … Tsay, S. C. (2003). Solar spectral radiative forcing during the Southern African Regional Science Initiative. *Journal of Geophysical Research: Atmospheres*, *108*(D13). https://doi.org/10.1029/2002JD002411

Plaza, A., Martinez, P., Perez, R., & Plaza, J. (2004). A Quantitative and Comparative Analysis of Endmember Extraction Algorithms From Hyperspectral Data. *IEEE Transactions on Geoscience and Remote Sensing*, *42*(3), 650–663. https://doi.org/10.1109/TGRS.2003.820314

Pope, R. M., & Fry, E. S. (1997). Absorption spectrum (380–700 nm) of pure water II Integrating cavity measurements. *Applied Optics*, *36*(33), 8710. https://doi.org/10.1364/AO.36.008710

Qian, Y., Jia, S., Zhou, J., & Robles-Kelly, A. (2011). Hyperspectral Unmixing via L_1/2 Sparsity-Constrained Nonnegative Matrix Factorization. *IEEE Transactions on Geoscience and Remote Sensing*, *49*(11), 4282–4297. https://doi.org/10.1109/TGRS.2011.2144605

Qu, Z., Kindel, B. C., & Goetz, A. F. H. (2003). The high accuracy atmospheric correction for hyperspectral data (hatch) model. *IEEE Transactions on Geoscience and Remote Sensing*, *41*(6), 1223–1231. https://doi.org/10.1109/TGRS.2003.813125

Rabbette, M., & Pilewskie, P. (2001). Multivariate analysis of solar spectral irradiance measurements. *Journal of Geophysical Research: Atmospheres*, *106*(D9), 9685–9696. https://doi.org/10.1029/2000JD900582

Reynold, R. M., Miller, M. A., & Bartholomew, M. J. (2001). Design, operation, and calibration of a shipboard fast-rotationg shadowband spectral radiometer. *Journal of Atmospheric and Oceanic Technology*, *18*(2), 200–214. https://doi.org/10.1175/1520-0426(2001)018<0200:DOACOA>2.0.CO;2

Richter, R. (1998). Correction of satellite imagery over mountainous terrain. *Applied Optics*, *37*(18), 4004. https://doi.org/10.1364/AO.37.004004

Richter, R., Bachmann, M., Dorigo, W., & Muller, A. (2006). Influence of the Adjacency Effect on Ground Reflectance Measurements. *IEEE Geoscience and Remote Sensing Letters*, *3*(4), 565–569. https://doi.org/10.1109/LGRS.2006.882146

Richter, R., & Schläpfer, D. (2002). Geo-atmospheric processing of airborne imaging spectrometry data. Part 2: Atmospheric/topographic correction. *International Journal of Remote Sensing*, *23*(13), 2631–2649. https://doi.org/10.1080/01431160110115834

Richter, R., & Schläpfer, D. (2015). *Atmospheric / Topographic Correction for Airborne Imagery (ATCOR-4 user guide v7.0.1)*.

Roberts, Y. L., Pilewskie, P., Feldman, D. R., Kindel, B. C., & Collins, W. D. (2014). Temporal variability of observed and simulated hyperspectral reflectance. *Journal of Geophysical Research: Atmospheres*, *119*(17), 10,262-10,280. https://doi.org/10.1002/2014JD021566

Roberts, Y. L., Pilewskie, P., & Kindel, B. C. (2011). Evaluating the observed variability in hyperspectral Earth-reflected solar radiance. *Journal of Geophysical Research: Atmospheres*, *116*(D24). https://doi.org/10.1029/2011JD016448

Rodgers, C. D. (1998). Information content and optimisation of high spectral resolution remote measurements. *Advances in Space Research*, *21*(3), 361–367. https://doi.org/10.1016/S0273-1177(97)00915-0

Rodgers, C. D. (2000). *Inverse Methods for Atmospheric Sounding: Theory and Practice*. Hackensack N. J.: World Scientific.

Sandidge, J. C., & Holyer, R. J. (1998). Coastal Bathymetry from Hyperspectral Observations of Water Radiance. *Remote Sensing of Environment*, *65*(3), 341–352. https://doi.org/https://doi.org/10.1016/S0034-4257(98)00043-1

Schaepman-Strub, G., Schaepman, M. E., Painter, T. H., Dangel, S., & Martonchik, J. V. (2006). Reflectance quantities in optical remote sensing—definitions and case studies. *Remote Sensing of Environment*, *103*(1), 27–42. https://doi.org/10.1016/J.RSE.2006.03.002

Schimel, D., Keller, M., Berukoff, S., Kao, B., Loescher, H., Powell, H., … Gram, W. (2011). *2011 Science Strategy: Enabling Continental-Scale Ecological Forecasting*. Boulder Colorado.

Shannon, C. E., & Weaver, W. (1949). *The Mathematical Theory of Communication*. *The mathematical theory of communication* (Vol. 27). https://doi.org/10.2307/3611062

Shaw, G. A., & Burke, H. K. (2003). Spectral Imaging for Remote Sensing. *Lincoln Laboratory Journal*, *14*(1), 22–38.

Smith, W. L., Hansen, C., Bucholtz, A., Anderson, B. E., Beckley, M., Corbett, J. G., … Winstead, E. (2017). Arctic Radiation-IceBridge Sea and Ice Experiment: The Arctic Radiant Energy System during the Critical Seasonal Ice Transition. *Bulletin of the American Meteorological Society*, *98*(7), 1399–1426. https://doi.org/10.1175/BAMS-D-14-00277.1

Tamminen, J., & Kyrölä, E. (2001). Bayesian solution for nonlinear and non-Gaussian inverse problems by Markov chain Monte Carlo method. *Journal of Geophysical Research: Atmospheres*, *106*(D13), 14377–14390. https://doi.org/10.1029/2001JD900007

Tanré, D., Kaufman, Y. J., Herman, M., & Mattoo, S. (1997). Remote sensing of aerosol properties over oceans using the MODIS/EOS spectral radiances. *Journal of Geophysical Research: Atmospheres*, *102*(D14), 16971–16988. https://doi.org/10.1029/96JD03437

Taylor, T. E., L'Ecuyer, T. S., Slusser, J. R., Stephens, G. L., & Goering, C. D. (2008). An operational retrieval algorithm for determining aerosol optical properties in the ultraviolet. *Journal of Geophysical Research*, *113*(D3), D03201. https://doi.org/10.1029/2007JD008661

Thompson, D. R., Gao, B.-C., Green, R. O., Roberts, D. A., Dennison, P. E., & Lundeen, S. R. (2015). Atmospheric correction for global mapping spectroscopy: ATREM advances for the HyspIRI preparatory campaign. *Remote Sensing of Environment*, *167*, 64–77. https://doi.org/10.1016/j.rse.2015.02.010

Thompson, D. R., Leifer, I., Bovensmann, H., Eastwood, M., Fladeland, M., Frankenberg, C., … Thorpe, A. K. (2015). Real-time remote detection and measurement for airborne imaging spectroscopy: a case study with methane. *Atmospheric Measurement Techniques*, *8*(10), 4383–4397. https://doi.org/10.5194/amt-8-4383-2015

Vane, G., Goetz, A. F. H., & Wellman, J. B. (1984). Airborne imaging spectrometer: A new tool for remote sensing. *IEEE Transactions on Geoscience and Remote Sensing*, *GE-22*(6), 546–549. https://doi.org/10.1109/TGRS.1984.6499168

Verrelst, J., Camps-Valls, G., Muñoz-Marí, J., Rivera, J. P., Veroustraete, F., Clevers, J. G. P. W., & Moreno, J. (2015). Optical remote sensing and the retrieval of terrestrial vegetation bio-geophysical properties – A review. *ISPRS Journal of Photogrammetry and Remote Sensing*, *108*, 273–290. https://doi.org/10.1016/j.isprsjprs.2015.05.005

Vukicevic, T., Coddington, O., & Pilewskie, P. (2010). Characterizing the retrieval of cloud properties from optical remote sensing. *Journal of Geophysical Research*, *115*(D20), D20211. https://doi.org/10.1029/2009JD012830

Wang, N., Du, B., & Zhang, L. (2013). An Endmember Dissimilarity Constrained Non-Negative Matrix Factorization Method for Hyperspectral Unmixing. *IEEE Journal of Selected Topics in Applied Earth Observations and Remote Sensing*, *6*(2), 554–569. https://doi.org/10.1109/JSTARS.2013.2242255

Wendisch, M., Müller, D., Schell, D., & Heintzenberg, J. (2001). An Airborne Spectral Albedometer with Active Horizontal Stabilization. *Journal of Atmospheric and Oceanic Technology*, *18*(11), 1856–1866. https://doi.org/10.1175/1520-0426(2001)018<1856:AASAWA>2.0.CO;2

Wielicki, B. A., Young, D. F., Mlynczak, M. G., Thome, K. J., Leroy, S., Corliss, J., … Xiong, X. (2013). Achieving Climate Change Absolute Accuracy in Orbit. *Bulletin of the American Meteorological Society*, *94*(10), 1519–1539. https://doi.org/10.1175/BAMS-D-12-00149.1

Williams Jr., R. S., & Carter, W. D. (1976). *ERTS-1, a new window on our planet*. *Professional Paper*. Retrieved from http://pubs.er.usgs.gov/publication/pp929

Winter, M. E. (1999). N-FINDR: an algorithm for fast autonomous spectral end-member determination in hyperspectral data. In M. R. Descour & S. S. Shen (Eds.), *SPIE's International Symposium on Optical Science, Engineering, and Instrumentation* (Vol. 3753,

pp. 266–275). https://doi.org/10.1117/12.366289

Wong, P. P., Losada, I. J., J.-P., G., Hinkel, J., Khattabi, A., NcInnes, K. L., … Sallenger, A. (2014). Chapter 5: Coastal Systems and Low-Lying Areas. In C. B. Field, V. R. Barros, D. J. Dokken, K. J. Mach, M. D. Mastrandrea, T. E. Bilir, … L. L. White (Eds.), *Climate Change 2014: Impacts, Adaptation, and Vulnerability. Part A: Global and Sectoral Aspects. Contribution of Working Group II to the Fifth Assessment Report of the Intergovernmental Panel on Climate Change* (pp. 361–409). Cambridge, United Kingdom and New York, NY, USA: Cambridge University Press. https://doi.org/10.1017/CBO9781107415379.010

Wyatt, C. L., Privalsky, V., & Datla, R. (1998). *Recommended Practice; Symbols, Terms, Units and Uncertainty Analysis for Radiometric Sensor Calibration*. *NIST Handbook 152*. National Institute of Standards and Technology.

Yoon, H. W., Gibson, C. E., & Barnes, P. Y. (2002). Realization of the National Institute of Standards and Technology detector-based spectral irradiance scale. *Applied Optics*, *41*(28), 5879–5890. https://doi.org/https://doi.org/10.1364/AO.41.005879